Effects of nonaxisymmetry in equilibria and MHD evolution of spheromaks

Thomas Edwin Benedett

A dissertation
submitted in partial fulfillment of the
requirements for the degree of

Doctor of Philosophy

University of Washington

2020

Reading Committee:

Thomas R. Jarboe, Chair

Brian A. Nelson

Christopher J. Hansen

Program Authorized to Offer Degree:
Aeronautics & Astronautics

University of Washington

Abstract

Effects of nonaxisymmetry in equilibria and MHD evolution of spheromaks

Thomas Edwin Benedett

Chair of the Supervisory Committee:
Professor Thomas R. Jarboe
Dept. of Aeronautics & Astronautics

Magnetic field configurations used for magnetic confinement of plasmas are often preferred to be simple in form, with symmetry sufficient to reduce their effective dimensionality to two or fewer, as with tokamak plasmas or ideal spheromak equilibria. In practice, three-dimensional effects may be unavoidable due to experimental geometry, especially in the case of the Steady Inductive Helicity Injection (SIHI) experiments HIT-SI, HIT-SI3, and the upcoming HIT-SIU, that necessarily impose nonaxisymmetric perturbations on the plasma for current drive. The effects of boundary shapes on plasma behavior will be studied in three parts, using the 3D magnetohydrodynamic (MHD) code PSI-Tet that solves equations on unstructured tetrahedral grids and is capable of simulating plasmas within arbitrary shapes: the first is an exploration of nonaxisymmetric boundary shapes, as well as nonaxisymmetric magnetic boundary conditions, on the ideal pressureless Taylor state equilibria that form the theoretical foundations for the targeted behavior of spheromak plasmas; the causes and limits of these effects are shown. The second is a study of the application of a single-temperature, dynamic-pressure Hall MHD model in PSI-Tet to the simulation of HIT-SI; the results of this model are compared to simulations of HIT-SI using an earlier constant-pressure model in PSI-Tet, as well as the (axisymmetric boundary) NIMROD code, and experimental HIT-SI data, finding that the new "finite-beta" model agrees with most, but not all, experimental trends. The third is an application of the single-temperature finite-beta Hall MHD model

in PSI-Tet to a study of different SIHI geometries (HIT-SI, HIT-SI3, and HIT-SIU) under equivalent simulated conditions to explore the influence of boundary shapes on simulated operating SIHI devices, with differences in performance noted and traced back to particular device features. These studies mark a significant step forward in the field of the exploration of SIHI plasma dynamics in complicated geometries.

TABLE OF CONTENTS

LIST OF FIGURES

LIST OF TABLES

GLOSSARY

BD: Bi-Orthogonal Decomposition: singular value decomposition, here applied to the analysis of signals varying in space and in time.

FEM: The Finite Element Method: a method of solving differential equations on complex domains via dividing them into a finite number of well-defined sub-elements.

HIT-SI: The Helicity Injected Torus - Steady Inductive experiment, using two half-toroidal helicity injectors for current drive.

HIT-SI3: The Helicity Injected Torus - Steady Inductive 3-Injector experiment, using three half-toroidal helicity injectors for current drive.

HIT-SIU: The Helicity Injected Torus - Steady Inductive Upgrade experiment, using a four-mouthed helicity injector manifold for current drive.

MHD: Magnetohydrodynamics: a single-fluid model of plasma dynamics.

SIHI: Steady Inductive Helicity Injection: a method of steady-state plasma current drive for toroidal plasmas.

ACKNOWLEDGMENTS

"If you wish to make an apple pie from scratch, you must first invent the universe," so said Carl Sagan. As such, this work of mine would not have been possible without the help of an enormous web of influences whose effects have all come together to let this be. I can name only the smallest fraction of them with certainty, particularly those close to me; any absences from this list are inadvertent. But I can begin with my advisor, Dr. Tom Jarboe, who is responsible for providing a place for me here at the University of Washington to conduct my studies; it is his work on and theories of spheromaks that form the foundation of my theoretical and computational exploration here. Dr. Brian Nelson has also been an invaluable mentor, with the sharpest editor's eye I know. Dr. Chris Hansen's help to me cannot be overstated: as the lead devloper of PSI-Tet in its current form and my predecessor as its user, his mentorship and guidance has been paramount to the direction my research has taken. The other members of my committee, Dr. Uri Shumlak, Dr. Justin Little, Dr. Marco Salviato, Dr. Bob Holzworth, and Dr. Sett You, have also been valuable mentors. Dr. George Marklin, original developer of PSI-Tet, was also a great help to me, as were my other co-workers at the PSI-Center, who supported me through many discussions, including Dr. Alan Glasser, Dr. Richard Milroy, Dr. John O'Bryan, Dr. Eric Meier. Special thanks goes to Susan Griffith for her computational help. The HIT-SI group has also been invaluable: particularly I want to thank John Rogers: most of the SIHI geometries shown here are his designs. My fellow students were also great helps and mentors, including Brian Victor, Aaron Hossack, Derek Sutherland (who also works with PSI-Tet and has consequently been of useful support,) Kyle Morgan (whose NIMROD simulations have been an excellent point of reference for how MHD simulations of SIHI experiments should behave,) Chris Everson, James Penna, and Alan Kaptanoglu (who also works with PSI-Tet, and is picking up where I left off with investigations of physics models.) I also want to thank Luisa Pareja-Klemisch for her invaluable coordination over the years. I'd also like to thank my family (my father Robert, my mother Ruth, my sister Laura, and the whole extended set beyond) for their support through my whole education and indeed my life.

DEDICATION

to Harlan Norem and Donald Benedett

Chapter 1

INTRODUCTION

1.1 *Motivation: High-thrust, high-efficiency space propulsion*

1.1.1 The challenges facing space propulsion

Of all the benefits that the application of nuclear fusion for power production could bring, including providing emission-free electrical power with millennia of fuel available with much-reduced radioactive waste compared to nuclear fission[1], one particular advantage that plasma-based nuclear power is especially suited to is the ability to provide a qualitative leap forward in space propulsion, of the sort that could render interplanetary travel more practical.

The cause is two particular principles governing rocket performance, the first of which is summarized in the Tsiolkovsky Rocket Equation:

$$\Delta v = g_0 I_{sp} e^{\frac{m_f}{m_o}} \tag{1.1}$$

Eq. 1.1 relates total change in velocity to the ratio of spacecraft masses before (m_o) and after (m_f) the impulse, governed by the specific impulse I_{sp}, which, when multiplied by g_0, the standard acceleration of gravity at Earth's surface, gives the speed of the rocket's exhaust, in turn commonly referred to with v_e.

It thus gives spacecraft mass (and consequently size and expense) as having an exponential dependence on the total change in velocity required, moderated only by the exhaust speed.

However, since thrust power is the kinetic energy flow rate of the propellant:

$$P_T = \frac{m\dot{v}_e^2}{2} \tag{1.2}$$

where (P_T) is thrust power in terms of propellant mass flow rate ($\dot{m}$) and exhaust speed (v_e), and thrust (F) is given as the propellant mass flow rate times the exhaust speed:

$$F = m\dot{v}_e \tag{1.3}$$

That results in the relation for thrust power-efficiency

$$\frac{F}{P_T} = \frac{2}{v_e} \tag{1.4}$$

which gives that power efficiency is inversely related to exhaust speed, meaning that, for a given amount of power available for a spacecraft, there is a direct tradeoff between mass-efficiency and thrust.

This can be observed on real spacecraft: the Saturn V moon rocket, even with its hydrogen-oxygen upper stages being at the practical limit of specific impulse for chemical rockets, could put a payload of only 4% of its launch mass into Earth orbit[2].

By contrast, the Dawn probe, which used electric propulsion to surpass the chemistry-imposed specific-impulse limits of chemical rockets (with its NSTAR ion engine capable of $I_{sp} = 3100$ seconds[3] versus $I_{sp} = 424$ seconds on the Saturn V's Rocketdyne J-2[4]) could only produce thrust equal to the weight of "a single sheet of notebook paper"[5], resulting in much less acceleration, even for a much smaller spacecraft.

This tradeoff is also attested to in the name of one plasma-based spacecraft thruster: VASIMR[6], the "VAriable Specific Impulse Magnetoplasma Rocket:" the utility of varying specific impulse, as opposed to simply maintaining it at a high level, for mass-efficiency purposes, is to be able to make the trade for greater thrust, given a set amount of power available.

To accommodate these competing concerns, a propulsion system capable of both producing great power and accelerating propellant to great speeds would be just what is needed to make traversing the solar system practical, i.e., to create spacecraft capable of carrying large masses quickly without needing to be almost entirely propellant by mass. To reduce mechanical inefficiencies, it would be best if the energy could be stored in the propellant (also so as to maintain an onboard power source, which would provide autonomy by not requiring a link to something external, like the Sun or an Earth-based laser, which would innately limit range or maneuverability,) and if that were to be the case, the energy would need to be stored in some form that holds more energy per unit mass than chemical bonds do, which suggests nuclear energy.

A further limitation to propellant energy (and thus mass-efficiency of the spacecraft) is the thermal limits of the solid material that directs propellant gases. This restricts the temperatures at which solid-confined-pressure-based rockets can operate to approximately the same order of magnitude as chemical limits do, (consider the melting point of tungsten: 3695 K, versus the adiabatic flame temperature of hydrogen and oxygen: 3473 K, both of which amount to upper bounds,) a way to maintain some separation between the propellant and the structure, as in electric rockets, which manipulate charged particles with electromagnetic fields instead of relying on gas pressure, would be preferred.

1.1.2 Nuclear fusion

Plasma-based magnetic confinement fusion is a natural fit for this problem, as it could permit a more-direct link from the power source to the rocket than existing electric rockets have, and a far higher specific-energy limit than chemical rockets can have. Plasma devices are natively required to maintain the separations between high-energy substances and structures, just as in advanced electric rockets.

Nuclear fusion power is produced from the combinations of nucleons from low-mass original reactants into higher-mass products, with the energy that is released coming from the reduction in energy required to bind the nucleons together between the reactants and products.

The energies released tend to be vastly higher than in chemical reactions, for example:

$$1\mathrm{H}_2 + \frac{1}{2}\mathrm{O}_2 \rightarrow 1\mathrm{H}_2\mathrm{O} + 3.0 mboxeV \tag{1.5}$$

Eq. 1.5 shows the combustion of hydrogen and oxygen molecules, including energy released ($1\ \mathrm{eV} = 1.6 \times 10^{-19}\ \mathrm{J}$)

$$ {}^{2}_{1}\mathrm{H} + {}^{3}_{1}\mathrm{H} \rightarrow {}^{4}_{2}\mathrm{He}(3.5\ \mathrm{MeV}) + {}^{1}_{0}\mathrm{n}(14.1\ \mathrm{MeV}) \tag{1.6} $$

Eq. 1.6 shows a nuclear fusion reaction, specifically "D-T fusion:" fusion of deuterium (hydrogen with one proton and one neutron) with tritium (hydrogen with one proton and two neutrons) producing helium and a free neutron, each with more than a million times the energy released in the combustion reaction, which results in the products achieving far greater speeds (and far greater temperatures) than the products of chemical reactions do, and with no need for an external power source to provide these accelerations, as electric propulsion requires.

However, nuclear fusion has not been successfully used to produce net-gain power in steady state; by contrast, nuclear fission (which breaks apart heavy nuclei to release energy, with the results of both fission and fusion approaching the lowest-energy-per-nucleon isotope, ${}^{62}_{28}\mathrm{Ni}$, from above and below, respectively, in order to release energy) has been in use for decades.

However, nuclear fission tends to produce more varied and dangerous waste products, threatening via radioactivity the health of both structures and life, and on top of that, nuclear fission is generally performed in solid-state reactors (with liquid coolant,) and that approach innately limits the temperature (and thus average kinetic energy) of the particles in action. The fuel required for nuclear fission, being supernova-produced heavy elements, is also much rarer in space than the light elements that are useful for fusion fuel.

Nuclear fusion, by contrast, requires temperatures far higher than solids can support in order to achieve net-gain power production. This is a difficulty for practical implementation, but a boon for its application for space propulsion, as it natively requires the lifting of the solid/reaction-mass interface, in a similar manner to electric propulsion.

That said, even granting the greater thrust and power output that fusion rockets would be capable of, fusion reactor hardware itself does not tend to be compact and lightweight enough to, at present, justify its use to replace, for example, chemically-propelled launch vehicles[7]. All the same, a qualitative step forward in terms of propulsive technology should be a benefit to the prospects of space exploration.

The conditions required to produce net-gain fusion are intense, requiring a particular triple-product of temperature, density, and characteristic energy confinement time on the order of $10^{21}(\mathrm{keV} \cdot \mathrm{s})/\mathrm{m}^3$ [8], and the multiplicity of variables in this product produces a spectrum of different approaches.

On one end, inertial confinement fusion raises densities to an extreme in order to require lesser energy confinement times via compressing the fusion fuel via laser pulses.

On the other main end, magnetic confinement fusion uses densities much lower than atmospheric densities and relies on the confinement of the ultra-high-temperature fusion fuel in plasma form by magnetic fields, and that is the approach being investigated here.

1.1.3 Plasmas

Plasmas are collections of charged particles that exhibit collective behavior[9]: fluids, like gasses so heated that their molecules ionize, and the ions and electrons at the temperatures and densities plasmas reach speed past each other and rarely or only briefly recombine. But the local densities of positive and negative charges tend to remain similar to the nonionized material, resulting in the property of “quasineutrality:” that plasmas can be globally neutral, despite being made of free charged particles.

Only in plasmas can nuclei reach the speeds necessary to collide and fuse without being driven apart by Coulomb repulsion. However, confining plasmas sufficiently to produce the triple products necessary for fusion has been a decades-long struggle.

Magnetic fields confine the charged particles of plasmas through the principle that the force on a moving charged particle due to a magnetic field is perpendicular to both the particle’s velocity and the magnetic field line, thus leading charged particles to orbit magnetic field lines while traveling helically along them.

But their helical paths means that straight or open field lines would not confine charged particles for very long at all in the axial direction, and so practical devices can be made through bending the field lines back around on each other into toroidal shapes. This carries with it a cost to confinement, as curved field lines do not confine particles as neatly as straight ones do, as the geometry of toroidal magnetic field structures permits particles to travel farther perpendicular to the field lines with each jump[1], but it also carries with it a cost to device complexity and practicality.

1.1.4 Magnetic confinement fusion device concepts

The magnetic fields capable of confining fusion plasmas must be very strong, and when used in steady state must be generated via superconducting magnets to avoid power loss in the magnetic field coils. In the current leading magnetic confinement fusion device concept, the tokamak (exemplified by the in-progress ITER (International Thermonuclear Experimental Reactor)[10],) two different systems require their superconducting magnets to link the toroid.

And while the most-accessible kinds of fusion (D-T, and, due to secondary reactions, D-D,) do not produce the full menagerie of dangerously radioactive products that fission does (owing in part to the number of possible products being fewer, due to the smaller nuclei involved,) they does produce extremely high-energy (14 MeV) neutrons, which blast through great quantities of matter and can do serious damage to fragile molecules, like ones found in the human body, or in superconducting magnets, and can also render some structural materials temporarily radioactive[11], as well.

An alternative to the tokamak, producing similar toroidal magnetic fields in a topologically-spherical volume, is the spheromak, which requires no material penetration of its geometric axis, and thus no superconducting toroidal field coils linking the plasma.

However, what the spheromak requires in lieu of toroidal field coils are much higher currents inside the plasma, as the Dynomak spheromak power-plant design requires a total toroidal plasma current of 41.7 MA[11], compared to, for example, the 7.8 MA calculated for the ARC tokamak reactor study[12].

With the lack of a superconducting center-stack, this also means that there can be no central solenoid for producing inductive startup, unlike what is possible on tokamaks.

The sorts of plasma current drive in use on tokamaks — neutral beam heating, radio-frequency (RF) current drive, and the already-ruled-out inductive current drive — are all largely impractical for the spheromak, owing to the high power per unit current requirements that the remaining concepts have.

1.1.5 Spheromaks and helicity injection

Attempts to use spheromaks' property of self-organization to drive the necessary current have resulted in current-drive schemes focused on helicity injection, such as the Sustained Spheromak Physics Experiment (SSPX) at Lawrence Livermore National Laboratory, which used coaxial helicity injection[13], and the HIT-SI and HIT-SI3 experiments at the University of Washington, which use (typically steady) inductive helicity injection[14].

Magnetic helicity is the linkage of flux with flux, defined as

$$K = \int \boldsymbol{A} \cdot \boldsymbol{B} dvol \tag{1.7}$$

where $\boldsymbol{A}$ is the vector potential and $\boldsymbol{B}$ is the magnetic field, and it is a quantity that is a constant of motion in magnetized plasmas, decaying only on a resistive timescale with the global magnetic structure itself. As resistivity decreases with temperature in plasmas, this means that magnetic helicity is conserved over very long timescales in fusion plasmas[15].

The Taylor minimum energy principle[17] dictates that, subject to this conservation of helicity, a plasma's preferred state will be the state of minimum energy with conserved helicity, which is, in general, in confinement volumes of proper shape and aspect ratio, the spheromak.

An ideal spheromak, such as that shown in Fig. 1.1, is a force-free equilibrium, meaning that it holds no pressure at all (and thus is not directly a confinement solution, but the addition of pressure does not entirely change the dynamics, so a pressure-confining spheromak-like object is still recognizable,) and is the minimum-energy solution to

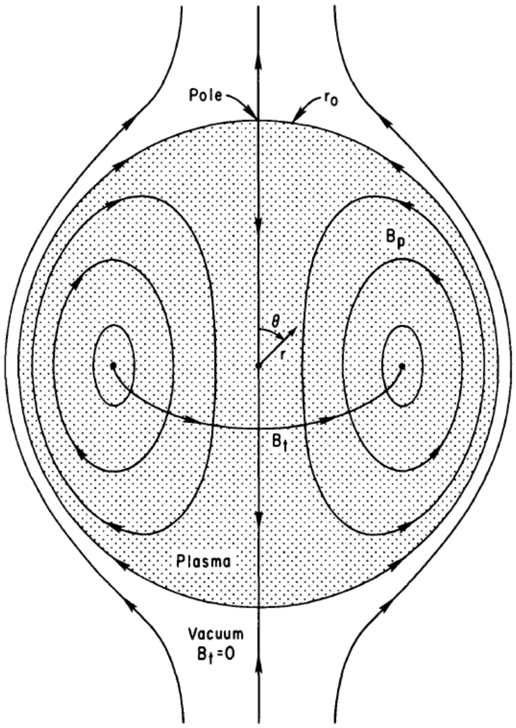

Figure 1.1: The ideal geometrically-spherical spheromak (Fig. 1 from[16].) A spherical shape is not optimal for prevention of instabilities, hence the oblate and dimpled flux-conserver shapes used on modern devices.

$$\nabla \times \boldsymbol{B} = \lambda \boldsymbol{B} \tag{1.8}$$

where λ, defined as

$$\lambda = \mu_0 \frac{\boldsymbol{j} \cdot \boldsymbol{B}}{|\boldsymbol{B}|^2} \tag{1.9}$$

(or, with $\boldsymbol{j} \parallel \boldsymbol{B}$ as in solutions to Eqn. 1.8, $\lambda = \mu_0 j/B$) is a global constant, for the ideal spheromak (and a constant per field line, otherwise.)

This produces a configuration with purely poloidal field at the walls and purely toroidal field at the center of the toroid, which is called, as on tokamaks, the magnetic axis[16]. The poloidal component of the magnetic field can be supported by external field coils, the only one of three primary magnetic coil systems which is common to both spheromaks and tokamaks. But, again, the toroidal field in the spheromak must be generated by plasma currents, of comparable magnitude to the current flowing in the external coils. While tokamaks utilize transport-driven bootstrap current (requiring particular pressure profiles, but not externally-driven) to provide large fractions of their required plasma current[1] for the sake of power efficiency, there is a competing interest: for the sake of control over the energetic plasmas, a substantial amount of externally-driven current is preferred.

Beyond that, however, steady-state current-drive methods tend to be power-inefficient per unit of current driven, with even the relatively-efficient lower-hybrid (radio-frequency) current drive typically requiring about 20 watts to produce one ampere of current[1], an amount that would require approximately 800 MW of current-drive power for a spheromak reactor[11]. Alternatively, neutral beam injection (the launching of high-energy neutral particles into the plasma to impart momentum and current when they ionize) tends to require enormous equipment, of comparable size to full-scale tokamaks themselves, and is even less efficient than lower-hybrid in terms of power per ampere of current driven.

As a result of this inefficiency, current-drive methods presently in use on tokamaks tend to be unsuited for sustaining high-current spheromaks, leading to the pursuit of other concepts.

The self-organization property of spheromaks in principle allows ore efficient current drive techniques to be used, such as helicity injection.

The time derivative of magnetic helicity is

$$\dot{K} = 2\int \boldsymbol{E_v} \cdot \boldsymbol{B_v} dvol - 2\int \boldsymbol{E} \cdot \boldsymbol{B} dvol \tag{1.10}$$

where E and B are the electric and magnetic fields in the plasma, and E_v and B_v are the electric and magnetic fields for the vacuum case with the same boundary conditions as the plasma case, where those boundary conditions are of the form (where $\hat{n}$ is the boundary surface normal) $\boldsymbol{E} \perp \hat{n}$, $\boldsymbol{B} \cdot n$, and total flux linkage of the boundary surface.

This means that it is possible, in theory, to use externally-generated electric and magnetic fields to regenerate helicity against resistive decay, and so potentially to preserve the plasma in its Minimum Energy with Conserved Helicity (MECH) state[18], in a current drive strategy known as helicity injection.

This strategy has historically seen several implementations: a prominent example was the helicity injection concept used in SSPX. That was coaxial helicity injection, which consisted of generating twisted magnetic fields and launching them into the plasma using a coaxial gun, where they would relax into the minimum energy state, i.e., a spheromak, and so produce the desired toroidal plasma configuration that produces good plasma confinement.

And that concept halfway worked: it was good for startup of toroidal plasma configurations (and continues to see use for such purposes even on tokamaks, such as the present-day NSTX-U (National Spherical Torus Experiment - Upgrade) spherical tokamak[20],) but it was not good for sustainment, because the repeated pulses of helicity injection required the old field, containing the plasma that had resistively heated up to high temperatures, to reconnect with the new field, which contained colder plasma and potentially was open to the walls of the experiment.

This resulted in the temperature of the plasma crashing with each pulse of injected helicity, as shown in Fig. 1.2 which was a poor sign for energy confinement.

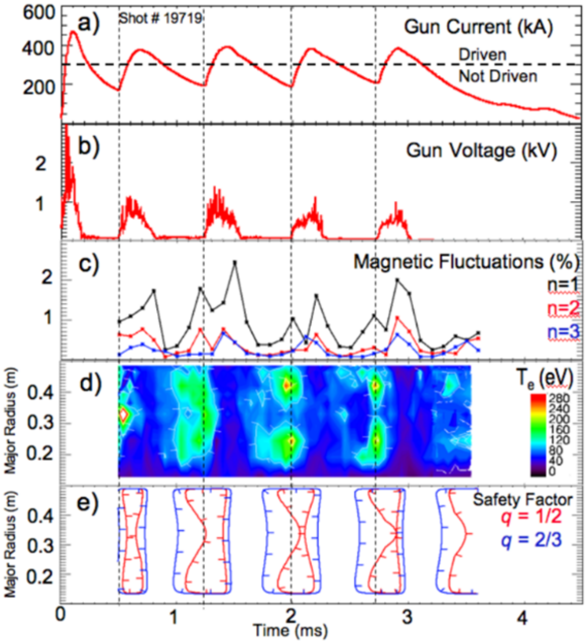

Figure 1.2: Results from SSPX operation (Figure 11 from 19.) Note especially a) or b) versus d), which demonstrate the loss of temperature confinement with each new pulse.

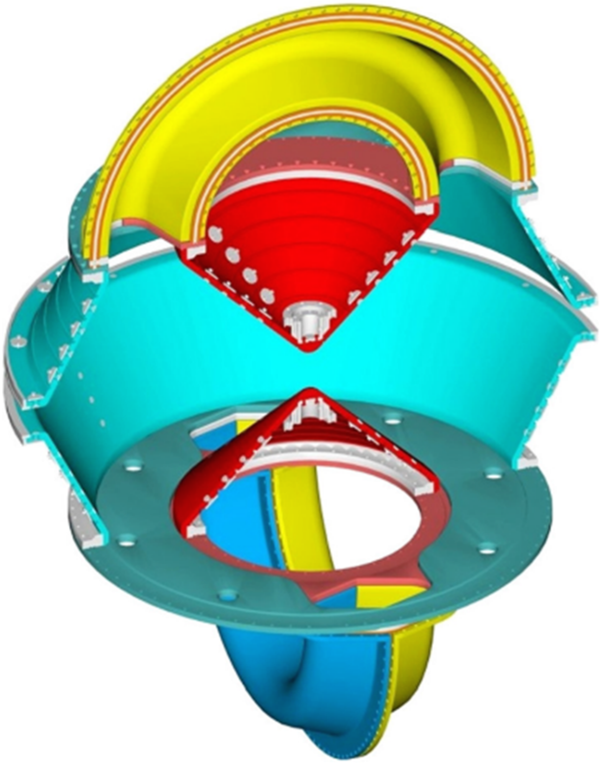

Figure 1.3: Cutaway of the HIT-SI experimental geometry, showing half of the main flux conserver (cyan) and the two half-toroidal helicity injectors (yellow and blue) at the top and bottom, oriented perpendicular (i.e. 90°) to each other.

1.1.6 Steady Inductive Helicity Injection and HIT-SI/HIT-SI3

An alternative helicity-injection scheme not reliant on discrete pulses of helicity injection has been developed here at the University of Washington, with the HIT-SI and HIT-SI3 experiments both being "Helicity Injected Tori" with "Steady Inductive" Helicity Injection (or SIHI) A cutaway of the shape of the HIT-SI experimental device is shown in Fig. 1.3

Steady Inductive Helicity Injection[21] is performed via the twisted magnetic fields being generated in half-tori called "injectors" attached at both ends to the main plasma confinement volume (or "flux conserver," for a spheromak) and the coils wrapped "toroidally" and "poloidally" around each injector induce current and magnetic flux, respectively. With the currents through those coils fired in opposite directions at a constant frequency, and multiple helicity injectors of this form operated out-of-phase, magnetic helicity can be injected steadily into the plasma volume, counteracting the resistive decay of magnetic helicity that would tend to dissipate the structure, without requiring the discrete reconnection pulses used in SSPX.

However, one possibility that needs to be ruled out for the success of this concept is that it doesn't, by its steadiness, leave the system steadily in the low-performance mode that SSPX observed, with constant magnetic reconnection being what is producing the relaxation inside and thus exhibiting poor energy confinement as seen during the drive pulses in SSPX.

In order for there to be some confinement-preserving method of inductive current drive (other than direct and transient solenoidal current drive as on tokamaks;) there must exist some method of cross-field current drive which connects the stochastic and reconnection-filled regions of the volume dominated by the flux that passes through the injectors with the smoother and closed-flux "spheromak region" which ideally exists as a toroid surrounded by the injector-flux-dominated region.

The method by which this is thought to occur on HIT-SI and HIT-SI3 is termed Imposed Dynamo Current Drive (IDCD) [22] which is indeed a proposed method of cross-field current drive, compatible with Cowling's Antidynamo Theorem (a 1933 mathematical result demonstrating the impossibility of steady-state axisymmetric dynamos[23]) through the use of nonaxisymmetric magnetic fields in the region in which current is driven only to the extent necessary to drive current against resistive decay (or a bit more, in the event of startup.)

In this method, imposed perturbations, as due to the constant-frequency but non-axisymmetric nature of the injector action, are capable of distorting the spheromak fields from axisymmetry just enough to separate the current paths from the field lines, providing small and rotating regions in which the voltage can be applied from the higher-λ (where λ, still referring to $\mu_0 j/B$, corresponds to energy-per-unit-helicity, as well,) injector region into the lower-λ spheromak region. This creates an electrostatic buildup along the field lines where the current realigns with the magnetic field, enabling the circuit to be closed and by that method current to be driven parallel to magnetic field lines.

IDCD produces cross-field current drive via a method akin to electron viscosity, whereby faster-moving current-carrying electrons in the injector region link to slower-moving electrons in the spheromak region through magnetic perturbations, reducing the velocity gradient in the electrons without collisions leading particles to jump across magnetic fields, or causing the field lines themselves to reconnect, enabling the transfer of current density ideally no slower than thermal energy flows out from the spheromak to the injector region, where there is effectively no thermal confinement at all. [22].

Provided that this concept works as described, it would be a much more efficient current drive method, estimated to require under 60 MW for producing all the current drive in the gigawatt-net-electric-power-producing Dynomak concept, resulting in an acceptable recirculating power fraction, and thus capable of enabling spheromak fusion reactors economically competitive with present-day coal power plants[11], and potentially spheromak fusion-propelled spacecraft[24].

Experimental analysis of the HIT-SI and HIT-SI3 experiments has been ongoing for the years of their operation, with some promising results, including, for example, an outward shift and symmetrizing of the position of the measured current centroid with increasing injector frequency on HIT-SI, and toroidal currents generated at ratios in excess of 3.8 times the injector current, and (separately) in excess of 90 kA[25].

Even so, the critical question remains of whether the principles observed on HIT-SI and HIT-SI3 will scale to larger devices, and be conducive to confinement of high-temperature plasmas as is necessary in order for this current-drive concept to support a sustained-spheromak fusion reactor of the sort necessary for the economical production of electric power or fusion space propulsion.

The ultimate test of this matter is exposure to reality, of course: whether such a larger device works or cannot be made to work is conclusive. But such tests are time-consuming and expensive and hard to maneuver; it is difficult to attempt multiple strategies on a limited budget, especially if a different approach may require an entirely different machine compared to a previous one. For this reason, simulations and computational investigation of plasma systems are pursued.

1.2 Computational Plasma Analysis

1.2.1 Motivation for computational analysis

In coordination with testing via reality, it is helpful to winnow down the number of possible approaches considered most promising to try via prediction and simulation, which can be performed with much faster turnaround and much easier modification. Due especially to the power of modern computers, computational plasma physics can provide some assistance in the navigation of real plasma physics, through attempts to capture the critical physics that will decide the behavior of the plasma in the actual device.

Of course, even with modern supercomputers, simulation of all the true physics in a plasma is far from practical. Simulating the interactions of n particles with every other particle in the system at once (due to electromagnetic and, if true accuracy is demanded, gravitational) effects would require computational resources vastly in excess of what is possible today or in the foreseeable future, for values of n even beginning to approach the quintillions of particles present in the plasma of even a device as small as HIT-SI.

Simplifications can be applied to approximate the general behavior of the plasma without requiring the calculation of exact quantities for every last particle in the system. These can begin by treating the collection of particles as a continuous statistical set, and by defining particular properties of the statistical distribution, reducing its absolute complexity in ways that make it easier to manipulate, and also in such ways that are usually reflected in the sorts of systems being evaluated. For plasmas, these simplifications produce a fluid model.

Of course, care is necessary to be sure that the conditions for validity of the simplifications are met.

1.3 Magnetohydrodynamics (MHD)

The result of several simplifications is the magnetohydrodynamic (MHD) model of plasmas, which treats the plasma as a gas subject to electromagnetic effects; this involves a combination of the Navier-Stokes equations, Maxwell's laws, and in particular, a variant of Ohm's Law, derived from the electron momentum equation, into which are put plasma-particular terms dictating the influence of fluid and electromagnetic effects on each other.

The MHD model relies on two assumptions particular to it: one that the speed of light is effectively infinite (restricting the time scales (frequency) of phenomena to be slow compared to the speed of light) and it also assumes, generally, that the mass of the electrons is negligible compared to the mass of the ions (considering that the total electron mass compared to ion mass for neutrality ends up anywhere between approximately one part in 1800 for hydrogen, or even less, for all other elements, this approximation is also generally valid for all but exotic systems like electron-positron plasmas.) This results in a reduction to a single-fluid model, as the general assumption of negligible electron mass removes the requirement to track electron mass and momentum evolution separately. A further simplification that can be made is to assume that the electrons and ions have effectively the same local temperature, ($T_e = T_i = T$) completely reducing the model to a single fluid.

These simplifications produce equations governing the evolution of the plasma in response to given initial and boundary conditions:

$$\frac{\partial \boldsymbol{B}}{\partial t} = -\nabla \times \boldsymbol{E} \tag{1.11}$$

$$\frac{\partial n}{\partial t} + \nabla \cdot (n\boldsymbol{u}) = D\nabla^2 n \tag{1.12}$$

$$\rho \left[\frac{\partial \boldsymbol{u}}{\partial t} + \boldsymbol{u} \cdot \nabla \boldsymbol{u} \right] = \boldsymbol{J} \times \boldsymbol{B} - \nabla(2nkT) - \nabla \cdot \Pi \tag{1.13}$$

$$\frac{n}{\gamma - 1} \left[\frac{\partial T}{\partial t} + \boldsymbol{u} \cdot \nabla T \right] = -nkT\nabla \cdot \boldsymbol{u} - \nabla \cdot \boldsymbol{q} + Q/2 \tag{1.14}$$

The following closures to Eqns. 1.11 - 1.14 are used:

$$\begin{aligned}\boldsymbol{E} = &(-\boldsymbol{u} \times \boldsymbol{B} + \eta \boldsymbol{J} + \\ &\frac{1}{ne}(\boldsymbol{J} \times \boldsymbol{B} - \nabla nkT) + f_{m_e} \frac{m_e}{ne^2} \frac{\partial \boldsymbol{J}}{\partial t}\bigg)\end{aligned} \tag{1.15}$$

$$\boldsymbol{q} = -n \left[\chi_{\parallel,e} \hat{\boldsymbol{b}}\hat{\boldsymbol{b}} + \chi_{\perp,i}(I - \hat{\boldsymbol{b}}\hat{\boldsymbol{b}}) \right] \cdot \nabla T \tag{1.16}$$

$$Q = \eta \boldsymbol{J}^2 - (\nabla \boldsymbol{u})^T : \Pi \tag{1.17}$$

$$\Pi = -\nu(\nabla \boldsymbol{u} + (\nabla \boldsymbol{u})^T - \frac{2}{3} I \nabla \cdot \boldsymbol{u}) \tag{1.18}$$

Altogether, Eqns. 1.11- 1.18 give the Hall MHD model used in the version of the PSI-Tet code used for the simulations shown in Chapters 3 and 4, showing, in order, the Maxwell-Faraday equation, the continuity equation, the momentum equation, the temperature equation, Ohm's Law (inserted into Ampère's circuital law, and including the artificial electron mass multiplication factor f_{m_e} for reducing equation stiffness), the anisotropic heat flux closure, the Ohmic and viscous heating term, and the isotropic viscosity tensor.

Those equations can be further simplified by ignoring the effects of pressure and temperature variations, producing a zero-beta model that is easier to manipulate; this will be presented in Chap. 3.

It is under the ideal MHD model that Rosenbluth and Bussac originally derived the field configuration that they called the "spheromak"[16]. However, more thorough analysis is possible through computational analysis of discretized forms of these equations in space and time, such as the exploration of the evolution of plasmas including their temperature and pressures locally and globally.

And so MHD codes have a long history of application to the exploration and diagnosis of plasmas, both in experimental devices and in nature. The sorts of codes typically applied to the analysis of plasma devices of the class of HIT-SI and others on the evolutionary tree for potential toroidal-geometry magnetic confinement fusion include specimens like NIMROD[26] and HI-FI[27], which take particular sorts of translational approaches in the conversion of the MHD equations into computational form, and have long pedigrees in terms of their applications to such analyses.

1.3.1 PSI-Tet's Finite-Element Model

PSI-Tet is an MHD code used for simulations of SIHI experiments that will be further described below. The particular translational approach that it takes is the use of the finite element method to discretize large domains into smaller elements of finite extent, within which the solution is approximated using a set of functions (often polynomials) that approximate spatial variation across the entire domain. Spatial accuracy is proportional to the number and internal representation of elements, as is computational difficulty.

The finite-element approach involves the conversion of the equations into a form that is more suitable for numerical solution, (a weak form instead of the strong form,) which guarantees only that they remain accurate in an integral sense over the volume[28] (which, if the elements are sufficiently fine, approximates the true solution across the volume well for many problem types,) and it differs from the finite-difference approach in permitting more flexibility in element shape.

$$\nabla^2 u = S \tag{1.19}$$

$$(\phi_j^T, \mathbb{L}(U)) = \int_\Omega \phi^T (\nabla^2 u - S) dV \tag{1.20}$$

$$\omega_j \int_\Omega \phi_i (\nabla^2 \phi_j) dV = \int_\Omega \phi_i S(x) dV \tag{1.21}$$

$$L_{ij} \omega_j = s_i \tag{1.22}$$

Equations 1.19– 1.22 show an application of the Galerkin method, as used in PSI-Tet, to transform partial differential equation (in this case, Poisson's equation,) into a discrete problem. The original continuous partial differential equation (the strong form: Eqn. 1.19) is converted into an equivalent weak form (Eqn. 1.20) with respect to a set of test functions; the Galerkin method uses for the set of test functions the same set of functions used to expand the solution. This produces a system of equations for the error-minimizing basis weights (ω_j, Eqn. 1.21,) which can then be expressed as a linear system, with the operator L_{ij} being a numerically-solvable square matrix (Eqn. 1.22) (Equations 1.14a–d from 28)

This specific element type and shape is of particular interest to simulations of Inductive Helicity Injection devices, as the NIMROD assumes a particular type of shape for the boundary, that being axisymmetry for the plasma volume. This means that, in NIMROD simulations of HIT experiments, the injectors cannot be modeled directly in the same simulations. In NIMROD simulations performed by Kyle Morgan[29] and James Penna (among others,) the injectors instead are modeled as boundary conditions upon an axisymmetric plasma volume.

NIMROD simulations show broad agreement with the trends and behaviors experimentally observed in HIT-SI and HIT-SI3. However, considering the influence that the helicity injectors themselves hold over the plasma behavior, the dynamics inside them, and how they are influenced by the main plasma volume they are coupled to, as well as the impact of the asymmetry of the volume itself on the plasma behavior, are also of interest to explore in simulations.

For purposes just such as that, the PSI-Tet code[28] has been developed here at the University of Washington, originally by George Marklin and Chris Hansen. It is a 3D MHD code that uses unstructured tetrahedral grids to simulate plasma behavior on arbitrary volumes, which does extend to the full plasma volumes of HIT-SI and HIT-SI3.

PSI-Tet's MHD model is mostly as shown above in Equations 1.11- 1.18, though additional physics may also be included in simulations. Derek Sutherland has implemented a model enabling the simulation of a neutral fluid as well as the ion and electron fluids, for greater accuracy for modeling plasmas that are not fully ionized[30]; Alan Kaptanoglu has added a separate electron temperature field[31], enabling an additional degree of accuracy for simulations of HIT-SI and HIT-SI3, for which experimental and simulated findings have consistently shown significant differences between ion and electron temperatures.

For the work presented here, however, the single-temperature model without neutrals, as shown in Equations 1.11- 1.18, and its simplification to zero-beta, will be used.

1.3.2 The PSI-Tet Taylor state equilibrium solver

While the primary function of the PSI-Tet code is, as mentioned, to solve the full time-dependent MHD equations in 3D domains (such as the full HIT-SI or HIT-SI3 plasma volumes, including the injectors,) it also includes a solver to compute force-free, constant-λ ideal MHD equilibria according to Eq. 1.8, on the same boundary conditions.

Equilibria satisfying that equation are a special case known as "Taylor states," and a subtype of them is referred to as "composite Taylor states," which specifically are cases where there is a nonzero vacuum field that does not couple directly to the primary Taylor state, allowing a spectrum of states where the force-free response to the vacuum field and the primary Taylor state can be added together in arbitrary ratios.

With the ratios selected appropriately, composite Taylor states can approximate the minimum-energy-state sought by a SIHI spheromak at a given instant of injector action. The force-free response to the vacuum field corresponds to plasma fields produced by injector action, and the primary Taylor state corresponds to the spheromak. While these force-free equilibria are the products of numerous simplifications and not high-fidelity models of plasma behavior, they are computationally inexpensive and offer glimpses of insight into how boundary conditions may affect SIHI plasma dynamics.

1.4 Structure of this dissertation

This project has two two tributaries that join together into a final whole: the first of these is presented in Chap. 2, where a study of the influence of boundary geometry and magnetic boundary conditions on the magnetic topology of Taylor state equilibria is performed, finding that nonaxisymmetric boundary features produce magnetic islands in the equilibrium in a predictable and manipulatable way. This is adapted from a paper that is intended for publication in autumn of 2020.

The second tributary is presented in Chap. 3, and is an exploration of PSI-Tet's finite-pressure Hall MHD model as applied to the HIT-SI experiment at multiple frequencies, exploring on what fronts it agrees and disagrees with other simulations and particularly experimental data. This is adapted from a paper published in *Physics of Plasmas* in April of 2020; see Reference 32.

These sections are joined together into a study, in Chap. 4, using PSI-Tet's finite-pressure Hall MHD model, of multiple SIHI geometries at equivalent conditions, to explore the effects that different boundary shapes, and in particular different injector configurations, have on simulated device performance, and the comparison of these simulations allows for an exploration of helicity injector physics.

Chapter 5 summarizes the results of the three preceding parts and draws recommendations for future steps based on what has been found.

Chapter 2

THREE-DIMENSIONAL EFFECTS ON TAYLOR STATE EQUILIBRIA

2.1 Motivation for Taylor state analysis

Ideally, closed-field-line toroidal magnetic equilibria are desired in magnetic-confinement plasma devices to confine particles to flux surfaces. Those flux surfaces are ideally nested, centered on a "magnetic axis" of purely toroidal field close to the center of the device's poloidal cross-section. This nesting ensures that the cross-field transport happens over the greatest physical distance and allows for the greatest insulation of the plasma core.

However, in practice, particle and energy confinement is not as neat as that intuitive cylindrical approximation suggests; the effects of bending the field lines into toroidal shapes with finite major radii are significant. The effects of curvature include pressure-driven instabilities when the pressure gradient and curvature vector are aligned[33]. The effects of the $1/R$ falloff in toroidal field include the trapping of a fraction of particles in "banana orbits[34]." In banana orbits, particles remain trapped on the outboard side of the magnetic axis and travel between disparate flux surfaces, allowing the short-circuiting of the insulation of the fusing plasma core.

If the magnetic topology is more complicated than simply-nested flux surfaces, these problems compound. When the flux surfaces are not entirely concentrically nested, but instead there exist flux tubes topologically isolated from each other; in plasmas where one such set appears to dominate; where its center appears to most clearly be the magnetic axis, the other sets are referred to as magnetic islands. Owing to their outermost flux surfaces short-circuiting the spatial insulation of the plasma core, these magnetic islands are generally detrimental to confinement. In tokamaks and other symmetric devices, magnetic islands are

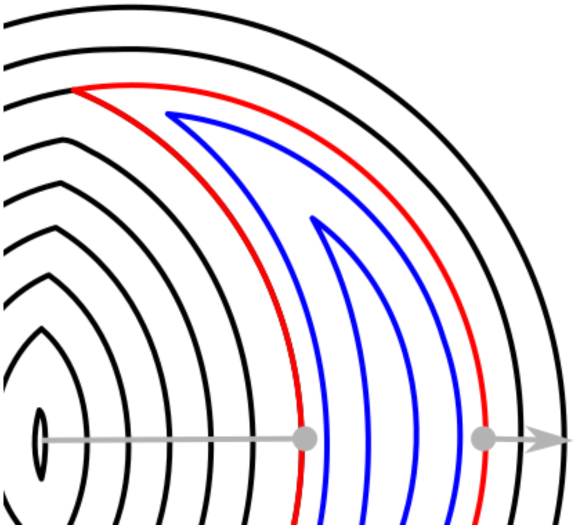

Figure 2.1: The cross-field distance traveled by a particle from the core is shown in gray; the flux surface shown in red is the boundary of an island. Purely parallel transport connects the inboard side of this island boundary with its outboard side, allowing the particle to bypass the volume of the island (the flux surface shown in blue) and providing it with a shorter cross-field path (the total distance shown in gray) to the wall than it would encounter if there were no island present.

often the result of a particular form of current-based instabilities known as tearing modes[35]. An illustration of the short-circuiting process is given in Fig. 2.1.

In axisymmetric plasmas, with equilibria defined by the Grad-Shafranov equation[36, 37],

$$\delta^* \psi = -\mu_0 R^2 p' - F F' \tag{2.1}$$

if disconnected flux tubes are present, they will not link each other, owing to the stipulation of axisymmetry. In three-dimensional equilibria, it is possible for flux tubes to link each other, and for magnetic islands to form according to each others' rational surfaces[38].

The presence of magnetic islands in the vacuum fields created by the nonaxsymmetric coilsets of stellarators is a well-established finding[39, 40, 41, 42, 43, 44], whereby the induced islands appear at rational surfaces corresponding to the shape of the stellarator, subject to the condition that they must grow out of the rational surfaces rendered available by the q- or rotational transform profile [43].

However, stellarator equilibria are not the only three-dimensional equilibria used in plasma experiments; in this chapter a qualitative evaluation of three-dimensional features in certain equilibria relevant to Reversed-Field Pinches (RFPs) and particularly spheromaks will be presented. While this investigation is most relevant to these configurations, it also has relevance to all others, including tokamaks.

2.1.1 Taylor relaxation and minimum-energy states

Spheromaks and RFPs have equilibria determined by Taylor theory[18], in which force-free equilibria (with no $\boldsymbol{j} \times \boldsymbol{B}$ force, necessarily implying $\boldsymbol{j} \parallel \boldsymbol{B}$) are defined by

$$\nabla \times \boldsymbol{B} = \lambda \boldsymbol{B} \tag{2.2}$$

Here λ is indeed a global constant, equal to $\mu_0 j/B$, and proportional to the curvature of the field.

The solution to Eq. 2.2 with the minimum value of λ corresponds to the Minimum Energy with Conserved Helicity (MECH) state[18], where magnetic helicity is the linkage of magnetic flux with flux, and is a constant of motion below resistive time scales, meaning that magnetic helicity decays only with the overall magnetic structure[15].

Spheromaks in particular are solutions to Eq. 2.2 in simply-connected volumes and have, in axisymmetric conducting boundaries, (even when the constraints of pressureless ideal MHD that pure Taylor theory requires are relaxed,) tokamak-like nested flux surfaces that can be supported with only one set of external field coils. Spheromaks require neither toroidal field coils nor central solenoids, and thereby, relative to a tokamak, eliminate most of the need for inboard-side superconducting magnets that would be particularly exposed to radiation in a fusion reactor and would add mass for space propulsion applications.

The price of eliminating these external coilsets is that the magnetic field must be generated by the plasma internally, and this requires a substantially greater plasma current to be generated compared to a tokamak of similar size, such as 41.7 MA for a proposed spheromak fusion reactor[11] versus 17 MA for ITER[45]. Current drive, as used on tokamaks, is generally power-hungry, in terms of the power loads necessary for the generation of plasma currents via the use of neutral beam injectors[46] or RF heating[47]. The already-significant power expenses in tokamak devices would be magnified considerably by the greater demands of comparable spheromaks.

Alternative forms of current drive applicable to spheromaks (as well as tokamak start-up[48]) have been employed that depend on the Taylor minimum energy principle, such as Coaxial Helicity Injection[49], has been explored on several experiments, including the Sustained Spheromak Physics Experiment (SSPX[50]), but the use of pulsed CHI has been found to be incompatible with good confinement[19]. The need for regular periods of magnetic reconnection in order to refresh helicity in the spheromak's core required regular dumping of the confined energy, and as such was not compatible with the sustainment needs for a fusion reactor.

Indeed, steady-state axisymmetric dynamos are forbidden by Cowling's Anti-Dynamo Theorem[23], so some sort of nonaxisymmetric activity is necessary for a steady-state dynamo. On experiments including SSPX, this activity was generated by instabilities, and its amplitude was poorly controlled.

A method of current drive to produce a steady-state dynamo with better control over the amplitude of nonaxisymmetric activity has been tested on the HIT-SI[14] (shown in Fig. 2.2) and HIT-SI3[52] experiments at the University of Washington. Steady Inductive Helicity Injection[21] uses multiple semi-toroidal helicity injectors attached to the main confinement volume. The injectors have flux coils and voltage coils wrapped locally-poloidally and locally-toroidally around the semi-toroids that are fired synchronously for each injector to induce twisted magnetic fields (i.e., with net helicity content) with a sinusoidal pattern to their

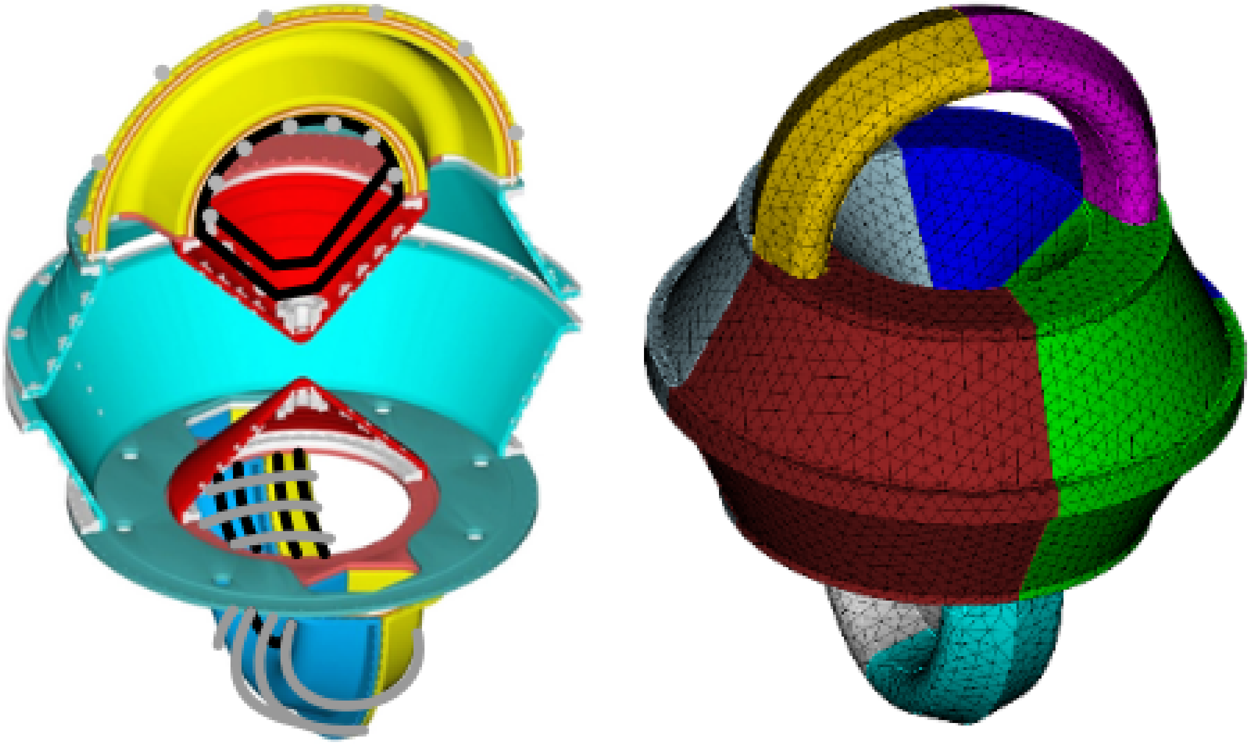

Figure 2.2: (Left) Cutaway of the HIT-SI experimental geometry, showing half of the main flux conserver (cyan and red) and the two half-toroidal helicity injectors (yellow and blue) at the top ("Y-injector") and bottom ("X-injector"), rotated 90° with respect to each other. Flux (gray) and voltage (black) coil locations are shown. The fields produced by these injectors are plotted in Fig. 4 of Ref. 51. (Right) exterior of the unstructured tetrahedral grid used for PSI-Tet simulations of HIT-SI.

amplitude. These multiple helicity injectors are fired out of phase, so that the sum of the squares of their amplitudes, proportional to the rate of helicity injection, remain constant.

This means that the helicity injection rate into the main flux conserver remains constant, and therefore the MECH state remains constant without decaying. Note that this presumes that this method of current drive includes a steady-state cross-field component, a mechanism for which has been proposed[22].

Ideally, HIT-SI and HIT-SI3 are supposed to produce Taylor-state like spheromaks (although with the outermost flux surfaces sacrificed for reconnection with the injector fields[22].) Worth noting is the fact that the presence of the injectors connected to the main spheromak volume means that the boundary conditions have significant nonaxisymmetric features, potentially altering the topology of the target spheromaks. In order to evaluate that possibility, numerical solutions of Taylor states will be presented using the PSI-Tet Taylor state equilibrium solver, as discussed in Sec. 1.3.2.

2.1.2 Interpreting Poincaré Plots

Many of the results presented here are the results of evaluations of Poincaré plots produced with PSI-Tet's field line tracer. Here is a brief guide to the different features that may be observed in the plots that follow.

The field line tracers used to identify the puncture points are launched from a single line on the outboard midplane, usually on the X- or Y- axis (where the axis of revolution is Z for an axisymmetric volume,) with a typical resolution of 200 points per launch line, and the inner side manually placed as close to the magnetic axis as possible. The coordinates of the field line tracers' crossings of YZ, ZX, or XY planes are recorded and plotted as colored dots, with the color ranging through the spectrum from red to purple based on whether the launch point was near or far from the magnetic axis, respectively.

These Poincaré plots are capable of identifying magnetic islands, and Fig. 2.3 provides a demonstration of what does and what does not show an island. In order to be considered confirmed by a Poincaré plot like the ones shown, there must be some width to an apparent

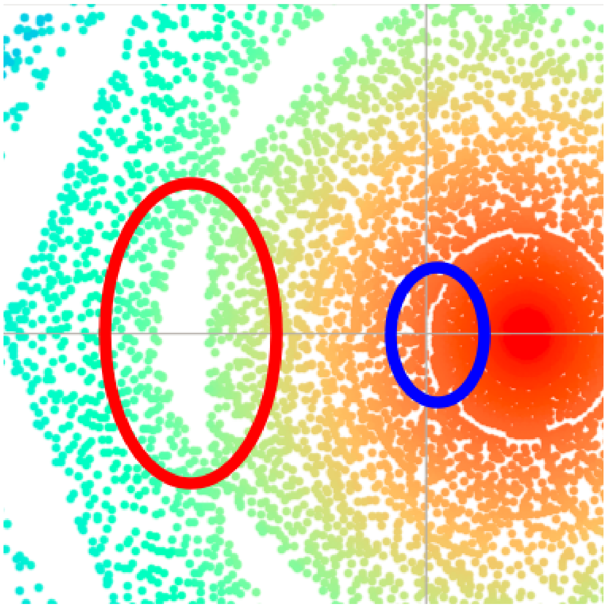

Figure 2.3: A look at the difference between real islands and artifacts of the Poincaré tracing: outlined in red is an island with definite width; the absence of internal structure is due to its orientation being such that it missed the launch point line; outlined in blue is what is likely not to be an island: its stepwise pattern and lack of curvature indicates that it is likely a series of nearly rational surfaces that were not filled in due to the finite number of steps taken in the field line traces.

island, and the minimum visible width is set by the geometry and artifacts due to near-rational surfaces.

Islands appear as gaps (as shown in Fig. 2.3) in the puncture points if the field line trace launch point happens to miss the island's flux tube, or as concentrations of same-colored puncture points if the field line trace launch point happens to hit the island's flux tube. If no particular concentrations or gaps with definite width are observed, the area can be said to be free of major islands (of the size resolvable by these plots.)

2.1.3 Structure of this chapter

The remainder of this chapter will be organized as follows: Section 2.2 will focus on the effects of boundary shapes on equilibrium topology, with a focus on (Sec. 2.2.1) the observed differences between variations in axisymmetric shapes versus nonaxisymmetric shapes, (Sec. 2.2.2) the effects of boundary shapes on what magnetic islands appear; (Sec. 2.2.3) the effects of elongation on the q-profile and the available islands; (Sec. 2.2.4) the limiting cases where nonaxisymmetries are distant or fine; (Sec. 2.2.5) a study of the effects of the grid resolution as itself a source of nonaxisymmetry, and (Sec. 2.2.6) an exploration of the rate at which islands emerge with increasing boundary feature prominence.

Section 2.3 will focus on the effects of nonaxisymmetric magnetic boundary conditions, as demonstrated through composite Taylor states, in particular (Sec. 2.3.1) the inducement of magnetic islands through the activation of helicity injectors (on instantaneous equilibria), (Sec. 2.3.2) the suppression of (some) magnetic islands through helicity injector action, and (Sec. 2.3.3) the influence of flux boundary conditions on equilibria within axisymmetric volumes.

Section 2.4 will present conclusions and remarks on potential implications and future followup.

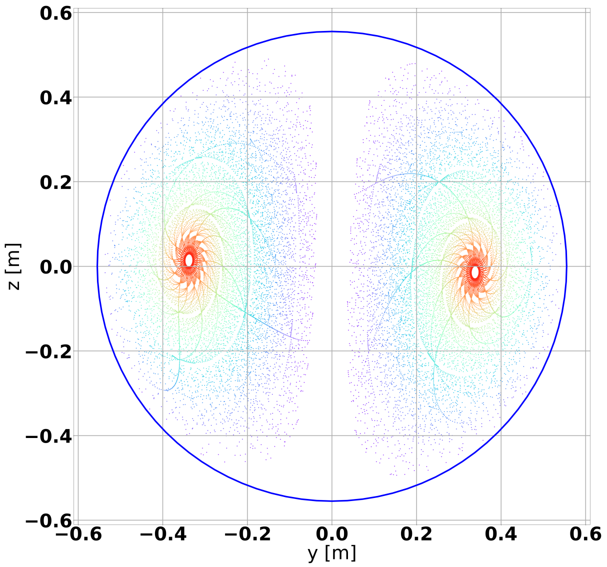

Figure 2.4: Poincaré plot of a Taylor state in a spherical flux conserver, with points colored according to their launch point (purple towards the wall, launched from 0.33 m to 0.55 m along the +X axis.) Note that the center of the spheromak is not reached by the field line traces owing to its slight tilt[53] tipping the magnetic axis away from the launch point line.

2.2 *Effects of boundary shapes on equilibrium topology*

As long known in stellarators[40, 41], three-dimensional equilibria often include magnetic islands not found on two-dimensional (generally axisymmetric) equilibria.

Taylor states, as evaluated here, are defined by Eq. 2.2 subjected to perfectly-conducting boundary conditions: $\boldsymbol{B} \cdot \hat{\boldsymbol{n}} = 0$, where $\hat{\boldsymbol{n}}$ is the boundary normal.

2.2.1 Axisymmetric shapes versus nonaxisymmetric shapes

This holds true for Taylor states; the original spheromak described by Rosenbluth and Bussac[16] was a two-dimensional equilibrium inside a spherical volume, and many investigations used cylindrical[53] or nearly-cylindrical volumes.

For both of the simple geometric cases, as shown in Fig. 2.4 and Fig. 2.5, the initial

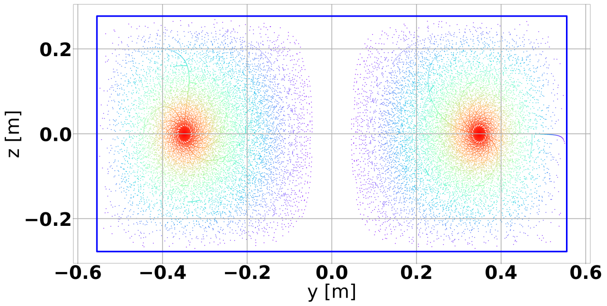

Figure 2.5: Poincaré plot of a Taylor state in a "tuna can" flux conserver, where the diameter is greater than the height, so as to avoid tilt instability[54], with launch points and coloration as described for Fig. 2.4.

axisymmetric equilibria hold true: while there do exist spots of clustering in the punctures, it must be noted that clusters without *width* are taken as representing only rational surfaces rather than islands; only when the punctures double back on themselves, as shown in Fig. 2.3. As such patterns are not seen in Figs. 2.4 and 2.5, these cases can be judged to be effectively island-free, as expected.

The lack of islands remains provided the volume is toroidally symmetric and with a radius large enough compared to its height to avoid producing a helical or tilted equilibrium. Islands do not appear regardless of the complexity of the poloidal cross-section, as Fig. 2.6 shows. Here, the poloidal cross-section is a pentagram, and even with this highly non-convex cross-section, the magnetic topology remains island-free. (For the purposes of numerical stability, sharp interior corners as on the pentagram cases have been blunted.)

But if the boundary is stretched by a factor of 1.2 in the out-of-page direction, inducing a toroidal variation that can "resonate" with the poloidal variation in the cross-section, the magnetic topology shifts considerably, as Fig. 2.8 shows.

A similar effect is seen with an ellipsoid: an oblate ellipsoid, shown in Fig. 2.7 shows topology congruent to the spherical case, but a scalene ellipsoid, once more with a factor of 1.2 stretch in the out-of-page direction compared to the axisymmetric case, shows the

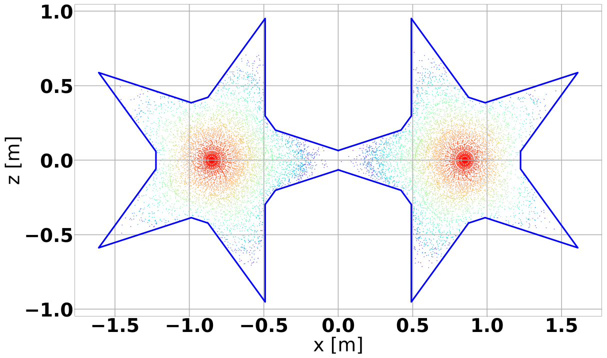

Figure 2.6: Poincaré plot of a Taylor state in an axisymmetric volume with a pentagram-shaped poloidal cross-section, showing monotonically-nested flux surfaces: a field topology similar to that in Fig. 2.7.

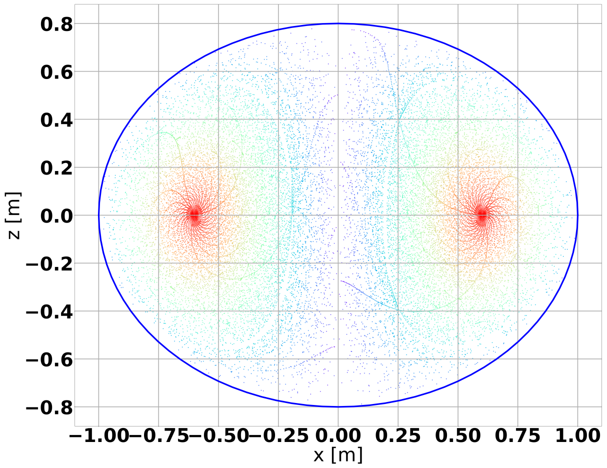

Figure 2.7: Poincaré plot of a Taylor state in an oblate-ellipsoidal (axisymmetric) flux conserver, showing monotonically-nested flux surfaces.

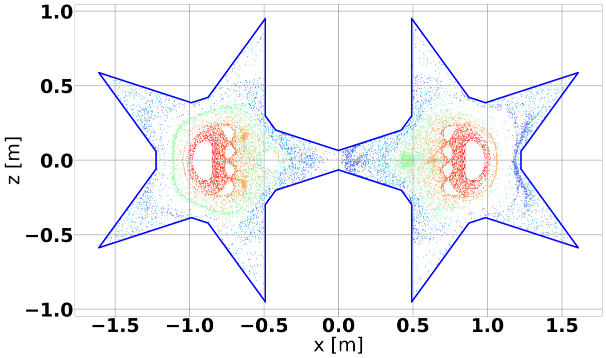

Figure 2.8: Poincaré plot of a Taylor state in a nonaxsymmetric volume with a pentagram-shaped poloidal cross-section, (scaled by 1.2 normal to the page) showing many distinct islands.

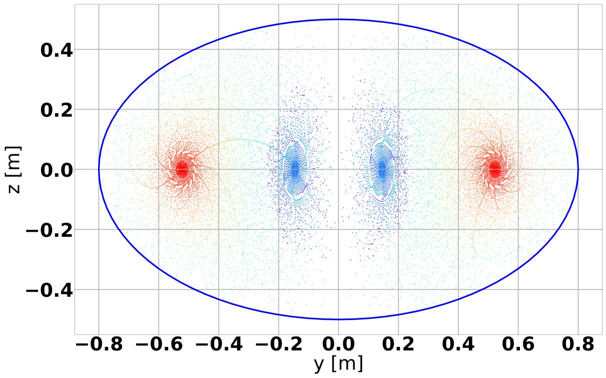

Figure 2.9: Poincaré plot of a Taylor state in a scalene-ellipsoidal (nonaxisymmetric, scaled by 1.2 normal to the page) flux conserver, showing a single major m=1/n=2 island in blue.

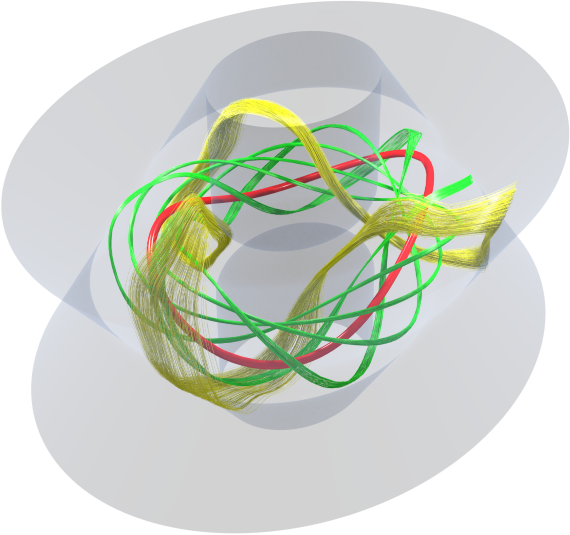

Figure 2.10: Field line traces of some of the most major islands in the nonaxisymmetric pentagram-cross-section flux conserver of Fig. 2.8, showing: m=1/n=3 in yellow, m=5/n=12 in green, and (faintly: the o-point trace of) m=1/n=2 in red.

presence of a major island structure, as seen in Fig. 2.9

2.2.2 Boundary shape versus excited islands

Despite their similar cross-sections in the toroidal plane (ellipses of eccentricity 0.663...), the cases in Fig. 2.8 and Fig. 2.9 show very different island structures, also visible in the 3D field line traces of the same, in Figs. 2.10 and 2.11.

Note the particular difference in the spread of the island spectrum; the boundary shape with greater poloidal complexity has many more islands, and in particular a pronounced island with m-number equal to the five points of the star-shaped poloidal cross-section.

The corresponding n-number of the $m = 5$ island on the elongated pentagram is 12; as expected, it is the case that the island mode numbers, m/n, correspond to the value of q at the flux surface from which they emerge. This is seen in these q-profile plots from Poincaré

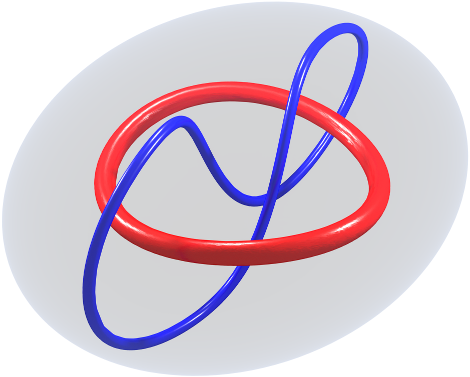

Figure 2.11: Field line traces of the main spheromak (red) and the o-point of the only (m=1/n=2) island (blue) in the scalene ellipsoidal flux conserver of Fig. 2.9.

plotting data, as seen in Fig. 2.16. With q equal to the number of toroidal transits per poloidal transit, the value can be approximated as the number of crossings of a poloidal plane divided by the number of transits of the toroidal plane, (presuming the spheromak is not tilted and its midplane is on the sampling midplane.) Via this method, islands that happen to intersect the launch point line appear as broadened plateaus in the q-profile; significant islands that happen to be missed by the launch point line appear instead as "reverse plateaus" in the q-profile (regions of lower but not flat slope surrounding a narrow, steep incline.) An example of both is shown in Fig. 2.12. Either way, significant islands appear as artifacts in the plot that persist even as the number of punctures taken is raised and as the grid resolution is also increased.

Of note is that the fact that the q-profile spreads of the different cases have different limits, both approaching 0 at the wall but with values at the magnetic axis of 0.44 for the star-shaped profile and 0.75 for the elliptical profile. This results in a different basis set of modes available for decomposition of the boundary shape: that the pentagram's peak q-value is below 0.5 means that the m=1/n=2 (q = 0.5) island is not available despite the plasma boundary containing a major n = 2 component; consequently other islands must

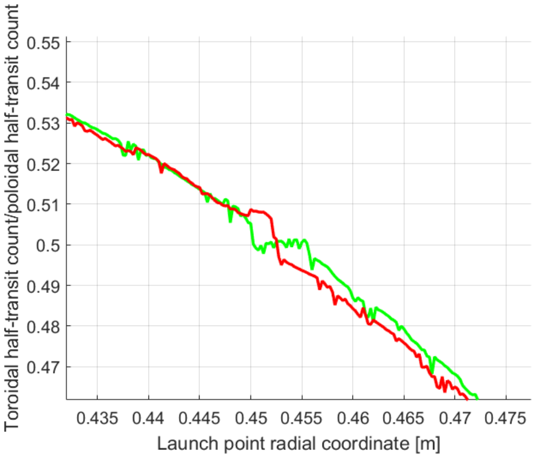

Figure 2.12: A close-up of the q-profiles of two different geometries (HIT-SI and HIT-SIU), both of which have islands at $q = 0.5$ that are visible despite the noise. HIT-SI3 is the case in green and its launch points intersected its islands, producing a plateau. HIT-SIU is the case in red and its launch points missed these islands, producing a ”reverse plateau.”

have large amplitudes to decompose the boundary shape. This, along with the complexity of the poloidal profile, is likely to contribute to much of the additional complexity of the resulting island structure within the equilibrium.

Further demonstrating that the excited islands do indeed result from a Fourier-like decomposition of their boundary shape are the equilibria for the volumes of HIT-SI, HIT-SI3, and the forthcoming HIT-SIU, as well as a version of HIT-SI with no injectors, whose overall boundary shapes are shown in Fig. 2.13.

Poincaré plots for HIT-SI, HIT-SI3, HIT-SIU, and the zero-injector boundary are shown in Fig. 2.14, and field line traces for the Taylor states in the same order are shown in Fig. 2.15. The no-injector case, as expected due to its axisymmetry, has no significant islands. Rational surfaces can be identified, but their traces are not shown in Fig. 2.15a as the focus of Fig. 2.15 is islands with identifiable width; consequently the only field line traced for this case is the magnetic axis.

For the other cases, pay particular attention to the islands identified as being excited

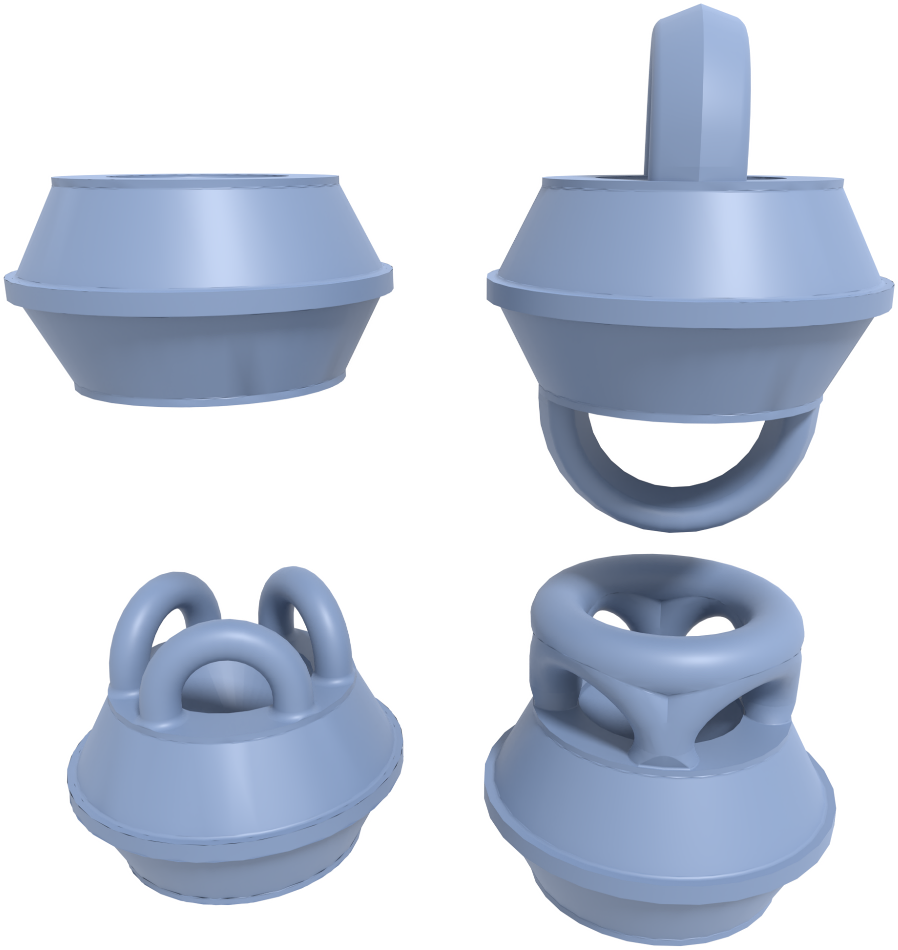

Figure 2.13: Shapes of the volume boundaries for four HIT-type geometries. Clockwise from top left: zero-injectors HIT-SI, HIT-SI, HIT-SIU, and HIT-SI3.

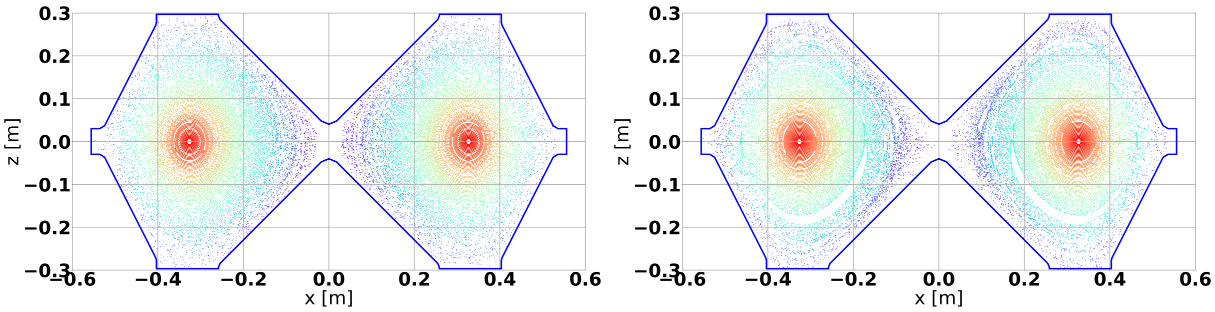

(a) HIT-SI without injectors (Axisymmetric)

(b) HIT-SI

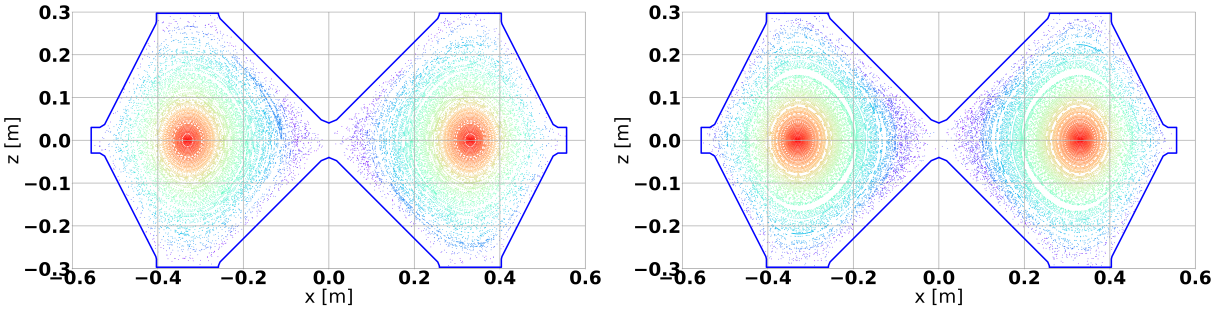

(c) HIT-SI3

(d) HIT-SIU

Figure 2.14: Poincaré plots of Taylor states in HIT-type boundary volumes, arranged as shown in Fig. 2.13. (Injectors are excluded from plots.)

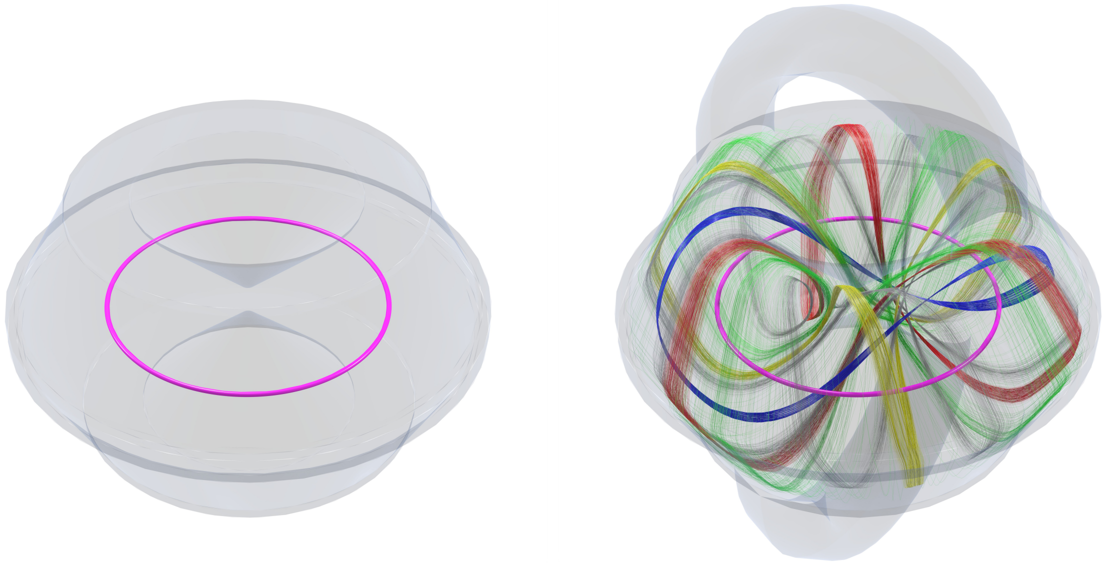

(a) HIT-SI without injectors

(b) HIT-SI

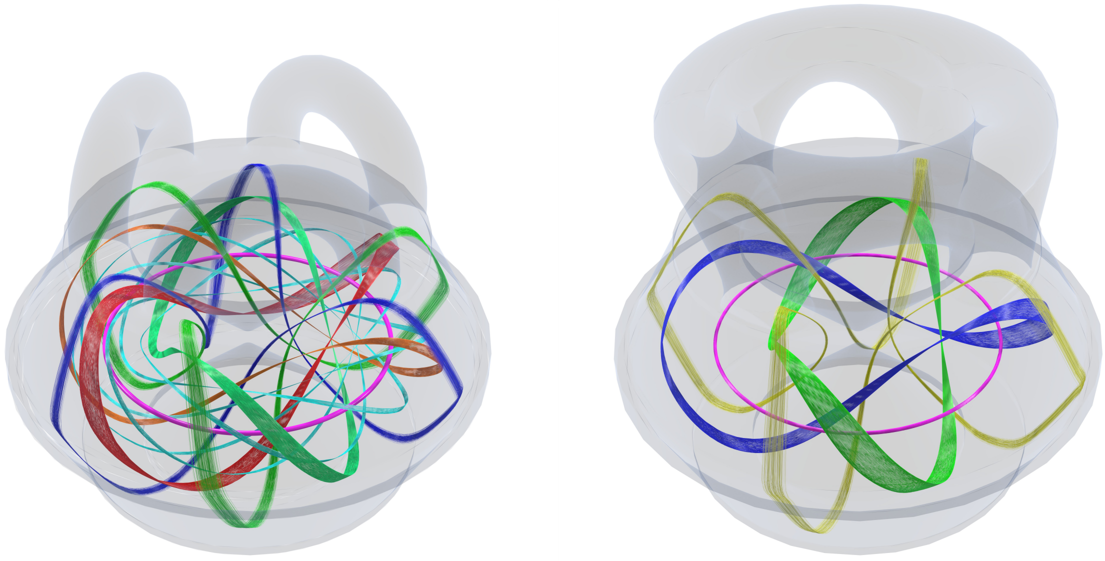

(c) HIT-SI3

(d) HIT-SIU

Figure 2.15: Field line traces of the most major islands and/or rational surfaces in Taylor states in HIT-type boundary volumes, arranged as shown in Fig. 2.13.

from the $q = 1/2$ surface: for each of the three injector configurations, a different number and pattern of m=1/n=2 ($q = 1/2$) islands are seen, and they are always aligned such that they “bulge into” the mouths of the injectors.

HIT-SI’s equilibrium is able to accomplish this with a single $q = 1/2$ island, as its four injector mouths are separated by 90° toroidally and, sequentially, 180° poloidally. Several other islands are also observed, including two prominent $q = 1/3$ islands, each of which touch two injector mouths (in Fig. 2.15b, the red $q = 1/3$ island touches upper right and lower left injector mouths; the yellow one touches the other pair) in a manner that is not geometrically trivial: if the islands’ progressions through poloidal angles were a linear function of toroidal angle, completing three even poloidal revolutions for every toroidal revolution, then the parts of the islands that presently bulge into the injector mouths should be separated by sixty toroidal degrees (being separated by half a poloidal revolution and thus a sixth of a toroidal revolution) rather than ninety degrees, as they are observed to be. However, this is an expected feature of spheromak equilibria; the toroidal twisting was observed even in the original spheromak equilibrium to be more pronounced on the inboard side than on the outboard side, such that field lines that are purely poloidal all along the wall can nonetheless have nonzero q-values from finite twist on the geometric axis[17]. A $q = 1/4$ island (shown in green in Fig. 2.15b) is also present and also touches each injector mouth, but it is not an especially voluminous island, for reasons that are discussed with the following cases.

HIT-SIU’s equilibrium takes two $q = 1/2$ islands to touch all four injector mouths, because there is no poloidal angular separation between the injector mouths. HIT-SIU also sees a significant $q = 1/4$ island (shown in yellow in Fig. 2.15d) that is nonetheless less prominent than the pair of $q = 1/2$ islands, despite being a single island structure that would touch all the injector mouths at once. The cause of this appears to be increased q-shear at the edge; there is less room for the islands to expand where the q-value is changing rapidly with minor-radial position versus the core, where the q-profile is flatter, varying less with minor-radial position and enabling the islands to inflate in size more substantially without deviating far from the value of q that the surrounding regions would have if the island were not present. This suggests that a naïve Fourier-type decomposition where all possible modes have equal weight in terms of their ability to contribute amplitude to the resulting boundary decomposition is not the situation observed here: modes can split into “unreduced fractions” if higher m- and n-numbers are needed than are *easily* available elsewhere in the q-profile, as is repeatedly observed in the cores of these spheromak-experiment volumes’ equilibria.

Indeed, HIT-SI3’s equilibrium, in turn, takes three $q = 1/2$ islands to decompose the boundary shape in such a way as to touch all the injector mouths. Notice additionally for the HIT-SI3 case the two $q = 1/3$ islands that also are spaced as to bulge into the injector mouths (which are not spaced at 60° increments toroidally) and distinctly not spaced equidistant from each other, as the minimum-energy arrangement would suggest if two islands from the same flux surface were excited for any other cause. Note also that despite the six injector mouths, this did not excite a significant $q = 1/6$ island; the lack of complete sixfold toroidal symmetry likely split the influence of the injector mouths into toroidal-mode-number divisors of six that could be more easily fit to the boundary shape; this is also likely due to the fact that the $q = 1/6$ surface is pressed closely against the wall in the equilibrium anyway, and that it therefore has little room to expand even if the injector mouths were spaced with equal angular separation.

Altogether, the islands that appear in the Taylor state equilibria seem to be distinctly overall due to, as well as responsive in the details to, the boundary shape in which the equilibrium is confined. Also, the shapes of the islands themselves are typically not elementary mode structures, but are shaped and sculpted by the boundary in which they are formed, which suggests difficulties in attempting to analytically define the prominence of any given island structure without computationally solving the equilibrium, for there are many degrees of freedom to consider in exploring the space of possible components for boundary decomposition that have been computationally observed to matter to the resulting equilibrium topology.

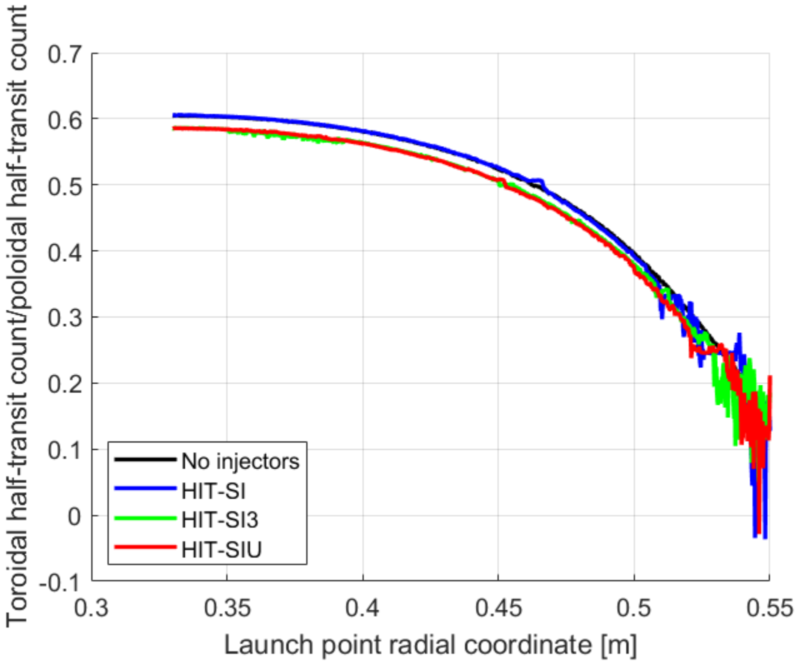

Figure 2.16: q-profiles (versus distance radially outward along the midplane from the magnetic axis of 0.33 m) for the different bowtie flux-conserver cases as calculated from the Poincaré data in Fig. 2.14.

2.2.3 Volume elongation effects on q-profile and excited islands

While the magnetic islands respond to the boundary shape in order to form a modal decomposition of it, the islands available depend on the range of the q-profile that the overall shape naturally provides.

The cases of the bowtie flux conservers (Fig. 2.16) indicate that the overall peak value of q is broadly independent of the nonaxisymmetric features possessed by the boundaries, at least, those of the scale of injector mouths, and is instead dependent largely on the elongation of the overall volume: notice how the q-profile traces generally align in their peaks for HIT-SI and the no-injector case, and then for the HIT-SI3 and HIT-SIU cases; the HIT-SI and no-injector flux conservers are slightly more elongated, with the top and bottom angled sections being separated by an extra 2 cm compared to the the HIT-SI3 and HIT-SIU cases.

Note again that the q-profile plots in Fig. 2.16 are produced from Poincaré plot data used for the plots in Fig. 2.15. The artifacts at the low end of the q-profiles come from the difficulties in tracing with appropriate fidelity in regions confined close enough to the wall such that the characteristic cell size is large in comparison. Finer grid resolutions would reduce the artifacts at the cost of greater memory usage than was available for the production of these plots.

This is further visible in the islands excited in their equilibria; in Fig. 2.14, it can be seen that HIT-SI has a $q = 3/5$ rational surface visible near the core (appearing as an $m = 3$ pattern of gaps just before the Poincaré plot becomes opaque red as the core is approached in Fig. 2.15b) that is not present in HIT-SI3 or HIT-SIU, because the q-profiles for the other cases do not peak above 3/5, and thus that q-value is unavailable for boundary decomposition.

Despite being an surface close to the magnetic axis and thus with broad room to expand into, it does not form a voluminous island because the boundary shape does not have an m=3/n=5 component with large amplitude.

However, if this were not true, and a volume's equilibrium q-profile peaked just above a value that *did* correspond to a major component of the boundary shape, this could potentially lead to performance difficulties, as the major island near the core could spoil confinement in this critical region. If this facet of spheromak behavior is experimentally observed, then this q-profile analysis may be of significant preliminary importance to ensuring that a device will be able to perform as well as intended.

Even though the q-profile for all explored bowtie geometries peak distinctly below $q =$ 1, the equilibria are generally responsive to boundary shapes even with the truncated set of modes available to them: recall, for example, how the q=0.5 surface in HIT-SI3 contains three separate m=1/n=2 islands, (i.e., an m=3/n=6 shape) shown in orange, red, and mint green in Fig. 2.15c, demonstrating that multiple occupancy of the same flux surface is possible.

Again note that the ability of the islands to expand to match the boundary shape largely corresponds to the shallowness of the shear in the q-profile at the resonant surface. Low values of q are associated with flux surfaces confined close to the wall and therefore have limited room to grow spatially without the q-shear growing too extreme for it; note that HIT-SIU sees a more-prominent pair of $q = 1/2$ islands than a single $q = 1/4$, because the $q = 1/2$ islands have more room to grow.

2.2.4 Effects of distant or fine nonaxisymmetries on equilibirum topology

The effects of boundary nonaxisymmetries on the magnetic topology are not without limit; removing the nonaxisymmetric features from proximity to the main spheromak region can reduce the impact of those features on the resulting island structure to near-zero with only a finite change. An example of this principle is a set of cases characterized by a midplane manifold injector system whose mouths are separated from the main flux conserver volume with a "lip" of increasing size, shown in Fig. 2.17.

The first case has the injector mouths intruding into the main spheromak volume, and producing many $q = m/10$ islands out of the available q-profile (that peaks below $q = 6/10$, so $m = 5$, $m = 4$, and $m = 3$ island structures are distinguishable.) The second case has the injector mouths removed radially by 10 cm, greatly reducing island volume; the islands visible in Fig. 2.17a are all imperceptible in Fig. 2.17b. The third case has the injector mouths removed radially by a further 20 cm (30 cm total), producing no observable difference from the step before: the islands remain imperceptible and devoid of volume.

This suggests that if nonaxisymmetric features are separated from the main volume by a channel of a width that is adequately small compared to $1/\lambda$ (proportional the characteristic distance it takes for the field to complete a full rotation) then, provided the depth of the channel is past a given threshold, the influence of the boundary nonaxisymmetries is effectively nullified.

This indicates that it is possible to include nonaxisymmetric features within the volume that nonetheless do not produce islands, provided they are appropriately insulated from the region of the main spheromak. For helicity injectors, a balance may need to be struck between connecting them closely enough to the spheromak to be able to operate efficiently

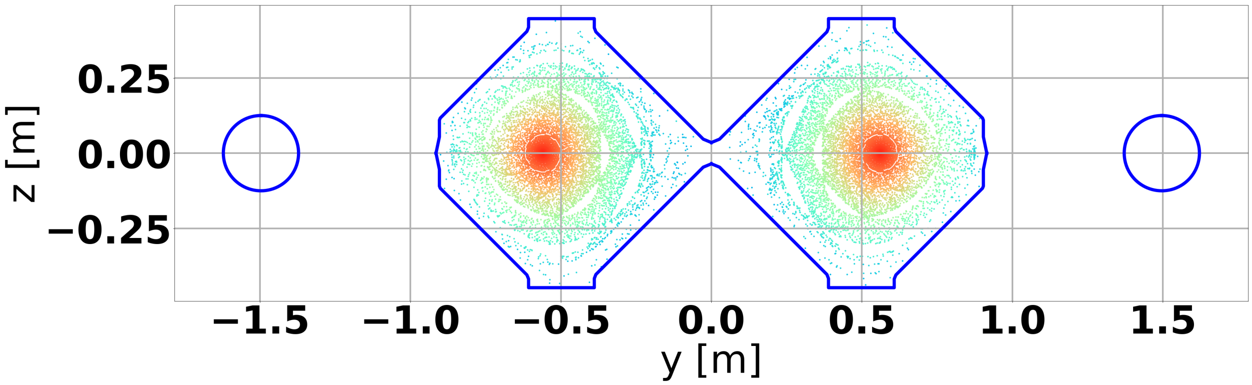

(a) 0 cm lip

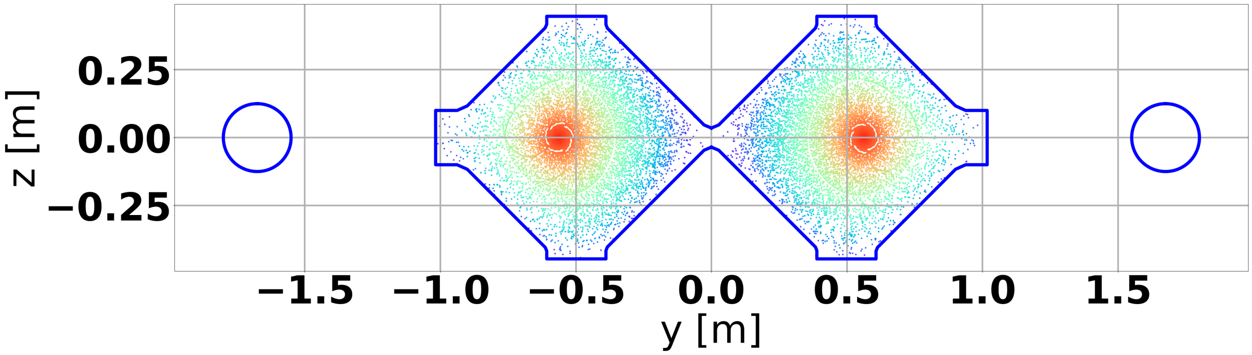

(b) 10 cm lip

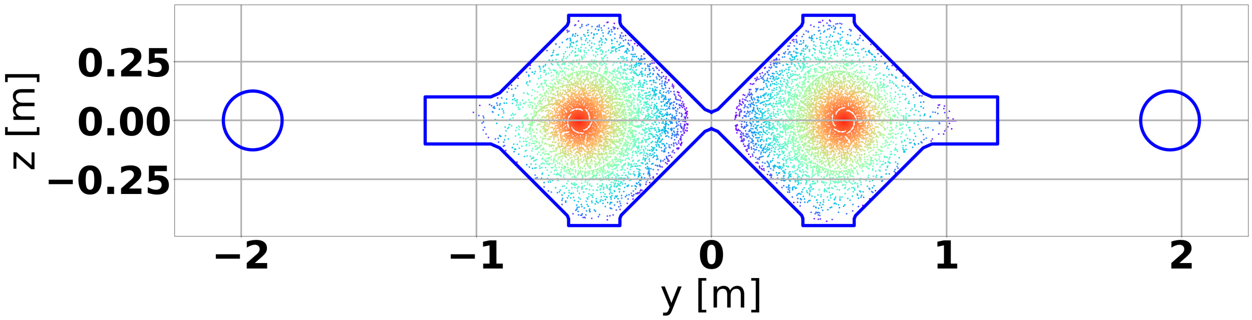

(c) 30 cm lip

Figure 2.17: Poincaré plots of Taylor states in a midplane-manifold geometry, with the gap between the injector mouths and the main spheromak volume changing according to the "lip" size listed above.

while also being removed from it sufficiently to keep their nonaxisymmetry from complicating the topology of the resulting equilibrium. This may be simpler than the constant-λ equilibria presented here suggest, as helicity injectors as used on HIT experiments operate at higher lambda (and thus with more tightly-curved magnetic field lines that are thus able to maneuver in tighter spaces) than the λ of the spheromak itself. However, investigating this effect requires an equilibrium code capable of computing 3D ideal MHD equilibria with variable λ[28].

Fine features also have limited effect on the island structures, as the case of the oblate spheroid from Fig. 2.7, now modified with a cylindrical insertion comparable in relative size to the Langmuir probe of HIT-SI. Even with the perfectly-conducting cylindrical insertion, the Poincaré plots show that only few and small islands have been excited by the change to the boundary shape. This is shown in Fig. 2.18, where in particular an n=3 island is visible as a set of threefold-symmetric gaps near the geometric axis, but the overall structure is largely free of major and pronounced islands, indicating that the disturbances to the topology that fine features produce, while extant, are themselves only fine. Note that most probes are not well-approximated as perfectly conducting and therefore this is not necessarily representative of the effects of real probes; it is instead an exploration of an idealized sharp boundary feature.

2.2.5 Effects of mesh resolution on equilibrium solving

The unstructured tetrahedral grids used in PSI-Tet calculations of these equilibria in boundary shapes are themselves, to a small degree, innately nonaxisymmetric; the extent to which this affects the resulting equilibria is explored in this grid convergence study of the HIT-SI flux conserver without injectors. Fig. 2.19 shows the result of varying the grid used in Sec. 2.2.2 from its characteristic grid size of 2.8 cm up and down by a factor of 2. In all cases, no substantial islands were observed, but the relative prominence of minor rational-surface-type effects diminished with increasing grid resolution; generally these surfaces are observed to have high m and n numbers. Altogether, this does indicate that gross islands as seen to

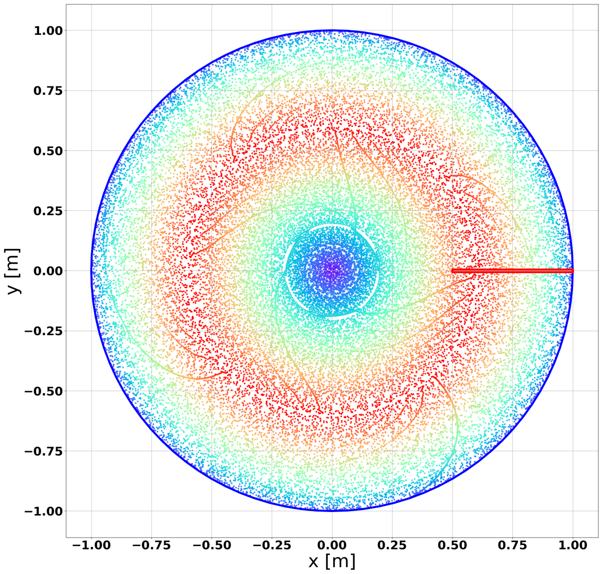

Figure 2.18: Poincaré plot of an oblate spheroid, as in Fig. 2.7, but modified with a cylindrical insertion visible as the red rectangle on the outboard right, demonstrating that while some islands are visible that were not present in the unmodified case, they are small and few.

correspond to features such as injector mouths are unlikely to be significantly affected by grid resolution effects.

2.2.6 Scaling of magnetic islands with boundary perturbation size

To evaluate the influence of boundary shape features on magnetic topology, a brief scan of boundary perturbation amplitude size was performed across multiple mode combinations, on a form defined as a torus with major radius $R_0 = 1$ m, and minor radius $a_0 = 0.55$ m with boundary perturbations of the form m- and n-numbered sinusoidal modes of amplitude α imposed in the minor radius in the poloidal and toroidal directions, respectively, as such:

$$r = a(1 + \alpha(\cos(m\theta)\cos(n\phi) + \sin(m\theta)\sin(n\phi)) \tag{2.3}$$

The final volume was the Boolean union of the shape defined by that boundary with

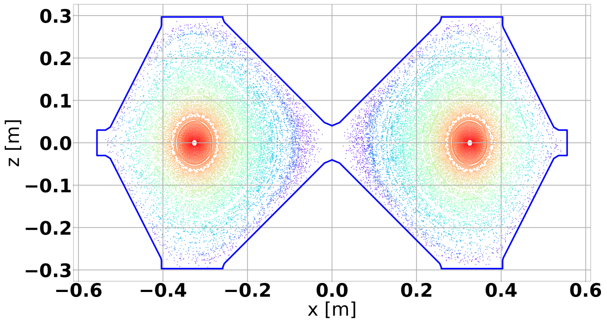

(a) 5.6 cm grid size

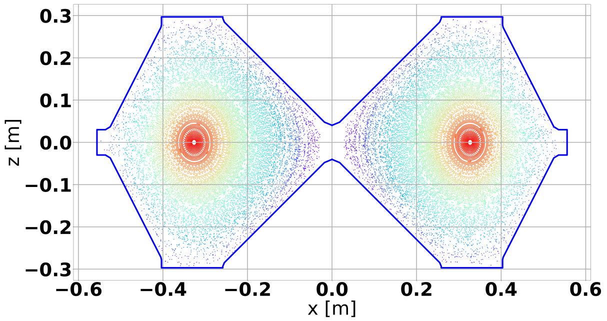

(b) 2.8 cm grid size

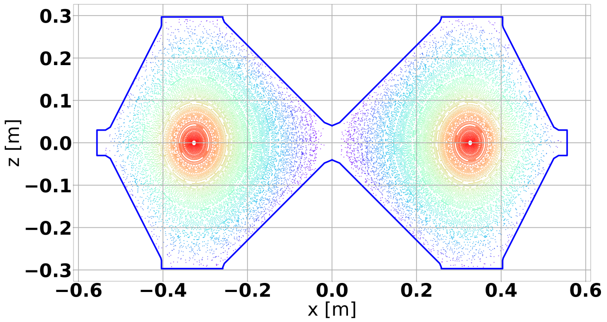

(c) 1.4 cm grid size

Figure 2.19: Poincaré plots of Taylor states in the zero-injector HIT-SI geometry, with increasing grid resolution, demonstrating that at the typical grid resolution (middle) there are no significant islands formed by the inherent nonaxisymmetry of an unstructured tetrahedral grid.

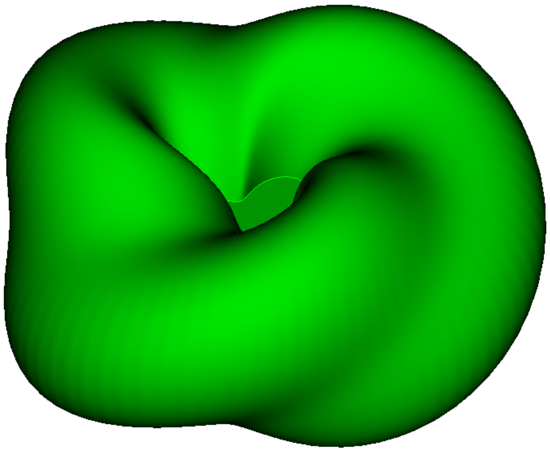

Figure 2.20: Volume created in CUBIT[55] for the purpose of geometric boundary perturbation analysis, with $m = 2$, $n = 3$, and $\alpha = 0.2$.

a cylinder centered on the origin of radius R_0 and height $a_0/10$, to produce the simply-connectedness needed for the equilibrium inside to be a spheromak, and further scaled by a factor of 1.2 in the z-direction in order for its resulting basic q-profile to peak above $q = 0.5$, so as to provide room for islands of all toroidal mode numbers greater than 1 to form. An example of this volume, shown with $m = 2$, $n = 3$, and $\alpha = 0.2$, is shown in Fig. 2.20.

A Python script for producing the CUBIT input file to generate all variants of the geometry used here is given in Appendix A.

With the basic shape defined, and with islands appearing out of the q-profile in a spheromak being of the form $m/n < 1$, the combinations chosen for investigation were $(m, n) = (1, 2), (1, 3), (2, 3)$ and $(2, 4)$, with α varied linearly from $\alpha = 0.00$ to 0.20 in increments of 0.01, to explore the effects of the size of boundary perturbations on the size of the resulting islands. λ remained within 5% of its unperturbed value for all cases, being 3.48 m^{-1} for $\alpha = 0$ and 3.63 m^{-1} for $\alpha = 0.2$ for (m,n) equal to both (2,3) and (2,4), and all other cases being no further from the unperturbed state. The islands chosen for evaluation from these Taylor states were the $q = 1/2$ island for $(m, n) = (1, 2)$, the $q = 1/3$ island for

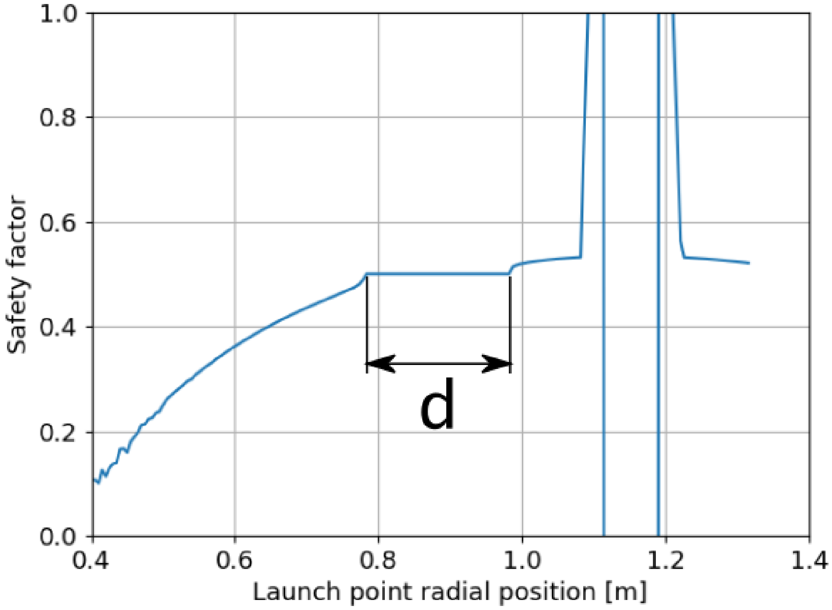

Figure 2.21: Distance d used as a measure of island prevalence, shown on the case with $m = 2$, $n = 3$, and $\alpha = 0.2$; the distance is the width of the flat region corresponding to the island's q-value, which in this case is 1/2. The Poincaré launch points along the x-axis of this were spaced at a distance of 5 mm apart extending outward from R = 0.4 along the positive or negative x- or y-axes, with the axis chosen for evaluation being the one that cut directly through the middle of the inboard side of the evaluated island. Note the discontinuities around what would have been the peak: when the perturbation gets sufficiently strong that near-axis flux surfaces rise above or below the XY-plane, the method of q-profile calculation fails.

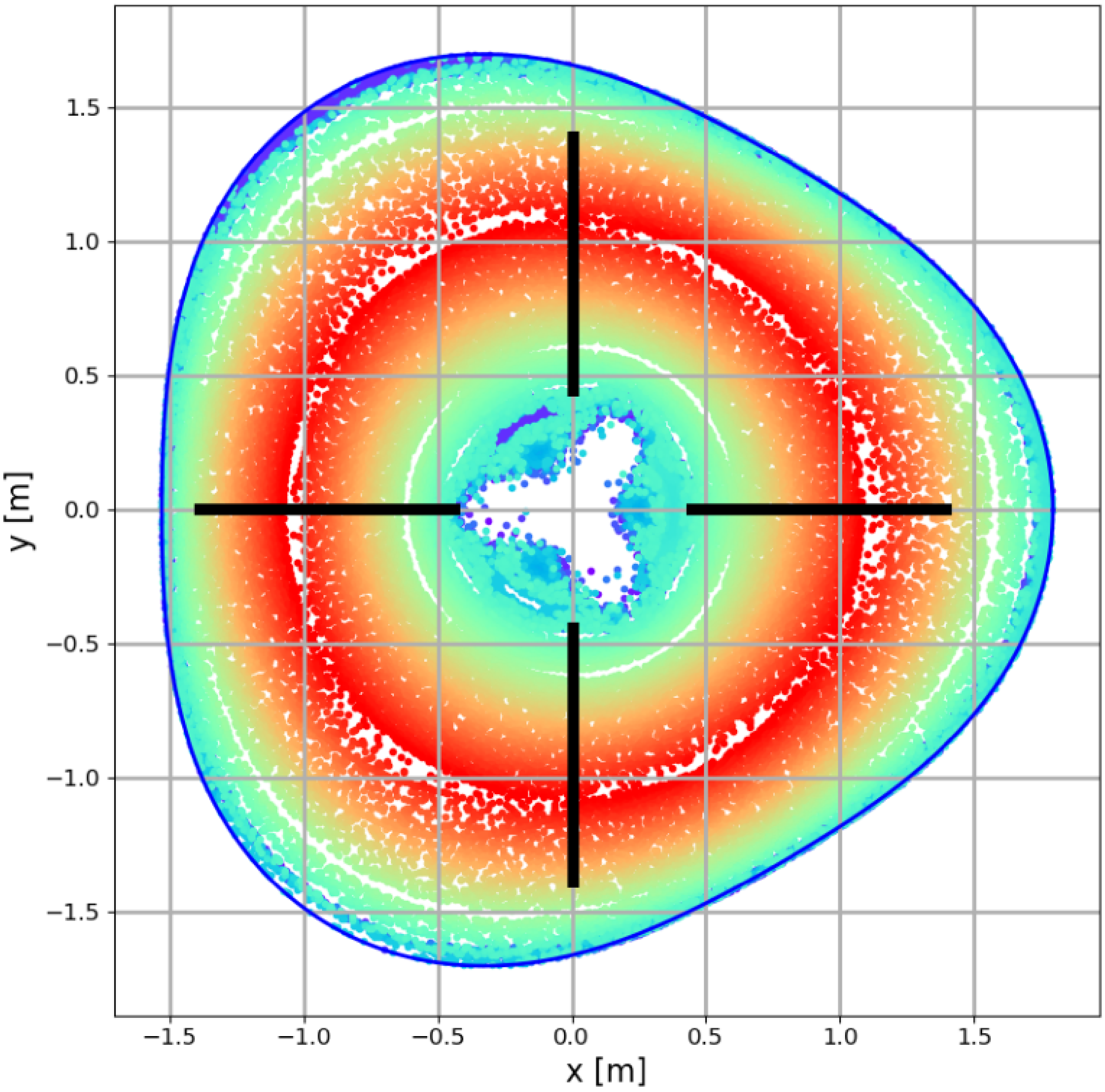

Figure 2.22: Location of the launch points used for q-profile evaluation, superimposed on a plot of an $m = 2$, $n = 3$, $\alpha = 0.2$ case (though the launch points used for this Poincaré plot do not correspond to the q-profile calculation launch points.) The black lines correspond to the locations lines of launch points used to calculate q-profiles as in Fig. 2.21; their radial extent is from R = 0.4 to R = 1.4, and along a given Cartesian axis depending on which one best crosses an island on the inboard side. For $(m,n) = (1,2)$, that is the -x axis; for (1,3), it is the $+x$ axis; for (2,3) it is the $-x$ axis, and for (2,4) it is the $+y$ axis.

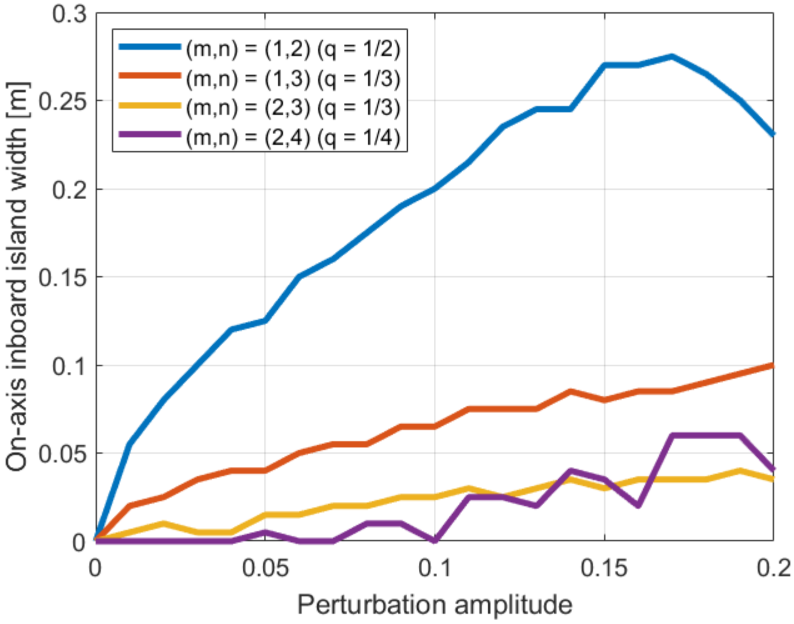

Figure 2.23: Plot of the inboard island width (along whichever +/- x/y axis directly crossed the island) versus boundary perturbation amplitude for four poloidal/toroidal mode number combinations, finding, to a precision of 0.5 cm, that the island width generally increases with perturbation amplitude and is strongly dependent on the island's placement in the q-profile for the rate and extent to which the island grows.

$(m, n) = (1, 3)$ and $(2, 3)$, and $q = 1/4$ for $(m, n) = (2, 4)$. The $(2, 3)$ case could not explore a $q = 2/3$ island as the q-profile did not peak above $q = 2/3$, and the $q = 1/4$ island was chosen over the $q = 2/4$ island for the $(2, 4)$ case to explore the dynamics of islands closer to the edge.

The metric chosen to characterize island prominence was the width of the inboard side of the island where it intersected a Cartesian axis, as shown in Fig. 2.21. With launch points separated by 0.005 m, this enabled a precision of a half-centimeter in island width, approximately the maximum that the computational resources used allowed. This still resulted in noise: small islands or the precise limits of the islands' boundaries were sometimes obscured.

A plot of the resulting island widths is shown in Fig. 2.23, where it can be seen that indeed island dominance trends upward with geometric perturbations, and that the island mode number, and thus its placement on the q-profile, determines how rapidly the islands develop and appear to saturate. For the unperturbed case, dq/dx was equal to 0.27 m^{-1} at $q = 1/2$, 1.0 m^{-1} at $q = 1/3$, and 1.4 m^{-1} at $q = 1/4$.

The $q = 1/2$ island of the $(m, n) = (1, 2)$ case, located in the core in a region of flat q, grew very rapidly with the slightest geometric perturbations, while the $q = 1/4$ island remained narrow enough that the 5 mm resolution could not reliably capture it until α exceeded 0.05. Islands corresponding to flux surfaces with low q' are therefore strongly weighted to contribute to the boundary decomposition that the equilibrium produces.

Initial trials of this survey did not include the scale factor of 1.2 along z. In those trials it was observed that when the q-profile did not contain the value corresponding to the boundary perturbation or a common factor thereof, such as the $q = 1/2$ case, when peak q fell below that value, was that the island spectra differed qualitatively between different values of α. Without the possibility of exciting an island that closely corresponds to the boundary-shape perturbation, that perturbation must be decomposed from a multitude of different components, and the prominence of the different ones appeared to vary with α.

Altogether, the available q-profile strongly determines island growth due to boundary features; boundary perturbations that correspond to q-values near the core produce islands much larger than those that correspond to q-values near the wall.

2.3 Effects of magnetic boundary conditions

2.3.1 Inducing islands with helicity injectors

It is possible to alter the calculated equilibrium within a given volume by imposing additional magnetic boundary conditions in the form of $\boldsymbol{\Psi} \cdot \boldsymbol{n}$, where $\boldsymbol{\Psi}$ is the net magnetic flux vector and $\boldsymbol{n}$ is the normal vector of a defined surface.

For analysis of HIT-type experiments, this technique is generally used to visualize the equilibrium that would be sought by the energy-minimizing helicity-conserving physics in the plasma at an instant at which the amplitude of the magnetic flux within the spheromak is at a given ratio to the flux through the helicity injectors. The necessary $\boldsymbol{\Psi} \cdot \boldsymbol{n}$ boundary conditions are applied to a surface that is not on the geometric boundary but cuts through through an injector throat. The resulting equilibrium is referred to as a "composite Taylor state." These additional magnetic boundary conditions, as with the boundary shapes, are capable of inducing islands in the magnetic topology.

Visible in Fig. 2.24 is a set of four Taylor states; in Fig. 2.24a is shown the composite Taylor state with the flux-boundary-condition "injector states" mixed in at a ratio of 1:200 to the original Taylor state, with the strength of the injector action varying in an n=1 pattern around the ten injector mouths. This produces no visible islands; an n=1 pattern for an injector manifold of sufficient symmetry, such as this ten-injector case, induces no more islands than the original non-composite Taylor state possesses. This is due to the q-value of the island it would excite being 1, which is out-of-range for this geometry, and is recognized as being a major threshold for current-driven instabilities on tokamaks[56] and similarly, though that value would be approached from below rather than above, for spheromaks.

Fig. 2.24b is as Fig. 2.24a but with the injectors operated in an n=2 pattern. This produces a major n=2 island, visible as a set of four crescent-shaped white gaps, bounded by green Poincaré punctures; two inboard of the magnetic axis, and two outboard. No other

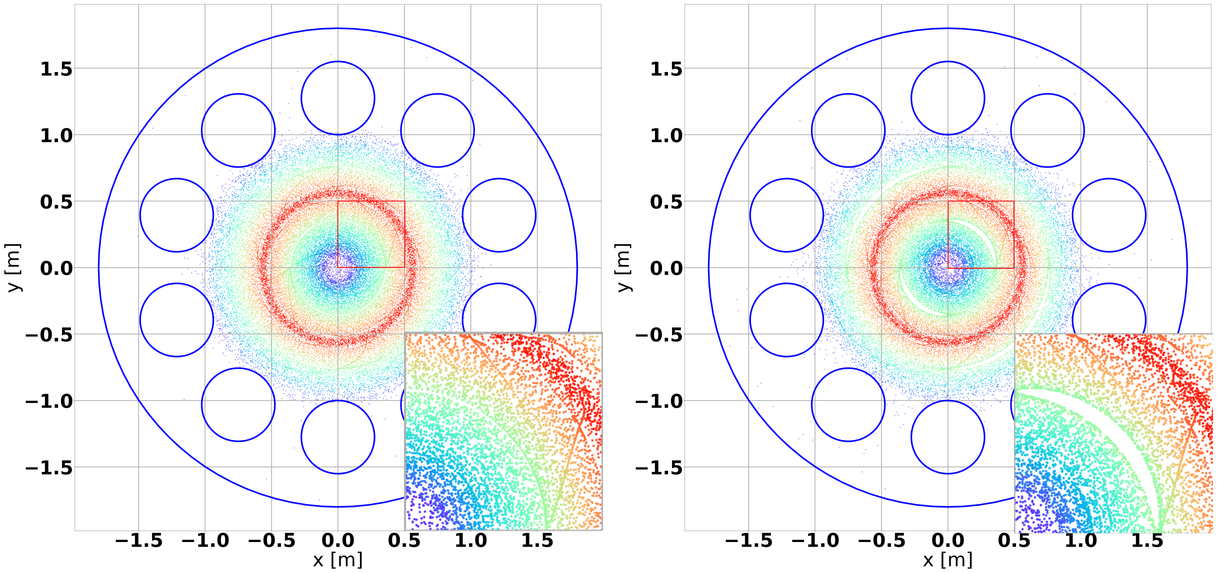

(a) $n = 1$ (b) $n = 2$

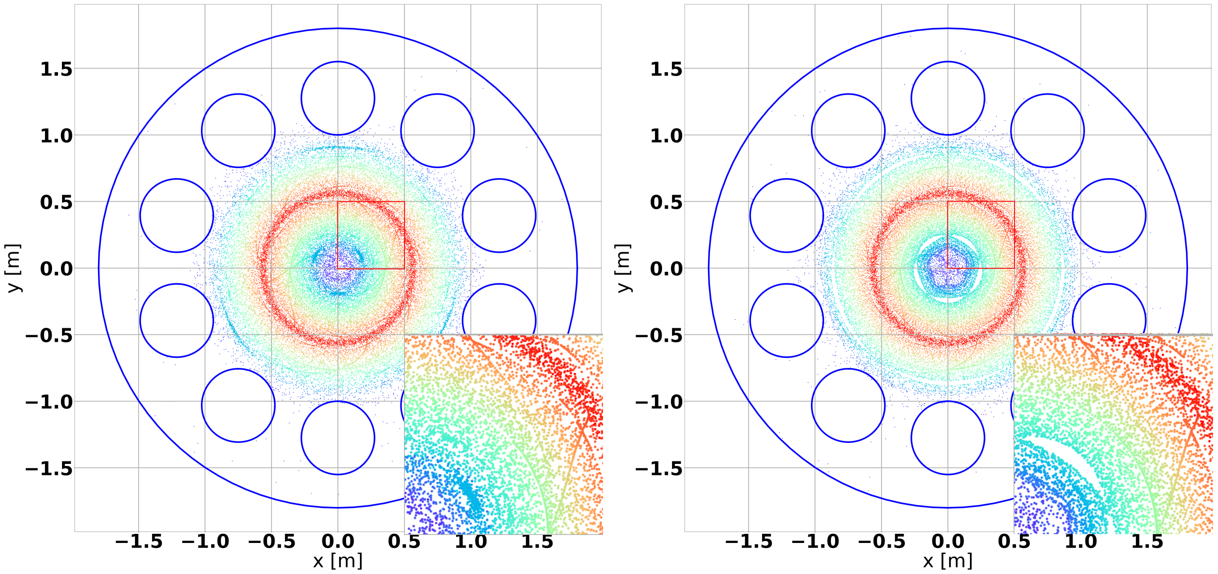

(c) $n = 3$ (d) $n = 5$

Figure 2.24: Poincaré plots of composite Taylor states in a ten-injector midplane manifold geometry (with cross-section as shown in Fig. 2.17b. All cases have the ratio of injector flux to spheromak flux at 200; a) has the injectors operated at $n = 1$, b) at $n = 2$, c) at $n = 3$, and d) at $n = 5$, showing (as gaps or as dark spots) the appearance of the corresponding n-numbered islands in all cases except $n = 1$. The insets at the bottom right show the area within the red squares.

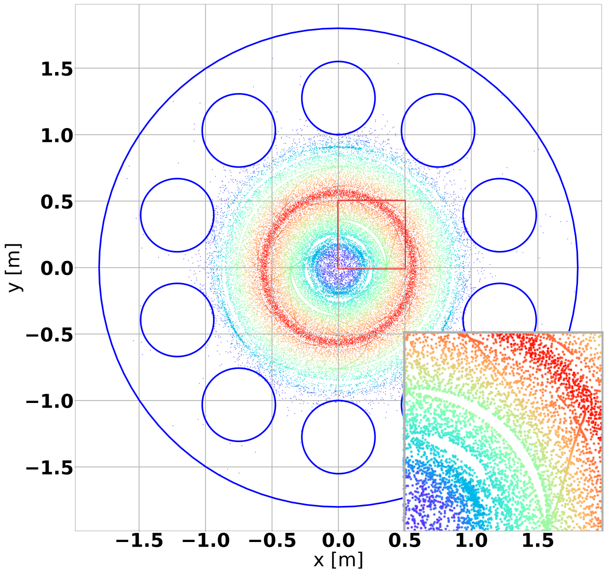

Figure 2.25: Poincaré plot of a composite Taylor state: cases b), c), and d) (n=2, n=3, n=5) from Fig. 2.24 mixed in even proportion, showing islands from all three injector-action components. The inset at the bottom right shows the area within the red square.

major island structures are visible, and while the n=2 island width is relatively smaller than seen on some previous cases that are induced due to geometric effects (such as, for example, Fig. 2.14b) this is with a geometry that naturally has no islands in the core and with the magnitude of the flux through an injector mouth being 0.5% of the flux in the spheromak; even small magnetic boundary conditions are capable of producing large effects.

Fig. 2.24c is as the previous two, but with the imposed perturbation being n=3, and this also results in an $n = 3$ island being visible, here seen as dense concentrations of blue Poincaré punctures, three inboard and three outboard. (For purposes of orientation, one concentration is visible at $(x,y) = (0,0.9)$.) Note that this illustrates the inducement of an island structure that corresponds to a toroidal mode number that is not present in the geometry alone: there are ten injector mouths, and yet with magnetic boundary conditions it can produce a well-defined n=3 island despite ten not being evenly divisible by three. A manifold with $2N$ injectors is thus capable of inducing modes of number up to $n = N$, and this is demonstrated in the next case:

Fig. 2.24d has the injectors run in an n=5 perturbation, and indeed major islands are visible at $q = 2/5$ (visible on both inboard and outboard as white gaps bounded by blue-green punctures) and, to a lesser degree, at $q = 1/5$ (visible close to the geometric axis as not-completely-empty gaps bounded by blue punctures.) This demonstrates the upper limit in terms of n-number of the major islands that can be deliberately introduced with this geometry: not all possible islands have been shown (n=4 is possible by the same principle as n=3) but n-numbers above 5 would be undersampled for this manifold.

Additionally, Fig. 2.25 includes the injector action being run in a linear combination of n=2, n=3 and n=5 at a proportion of one-third each compared to the cases in Fig. 2.24, (which, when put together, still add up to one part in 200 of the spheromak's flux magnitude per injector mouth,) and all three perturbations' corresponding islands are visible in the same positions they are found in Figs. 2.24b, 2.24c, and 2.24d, which demonstrates that it is possible to excite multiple sets of islands via injector action in the composite Taylor state model. To the extent that the composite Taylor state model corresponds to reality, it can thus be presumed that the effects of different n-numbers of injector operations can be stacked if the imposed perturbations are also stacked.

2.3.2 Suppressing islands with helicity injectors

As it is possible to create islands, using injector boundary conditions, that are not present due to the boundary shape alone, it is also possible to, at least instantaneously, in the composite Taylor state model, suppress islands with injector action.

Fig. 2.26a shows the non-composite Taylor state of a midplane-manifold geometry that has been stretched by a factor of 1.05 in the y-direction, resulting in a major n=2 island from the q=1/2 surface.

Fig. 2.26b shows the effects of activating the injectors in an n=2 pattern to produce destructive interference. (The injector states were mixed in at an amplitude 1/12th that of the spheromak.) While this results in significant n=5 islands, the n=2 island has been largely

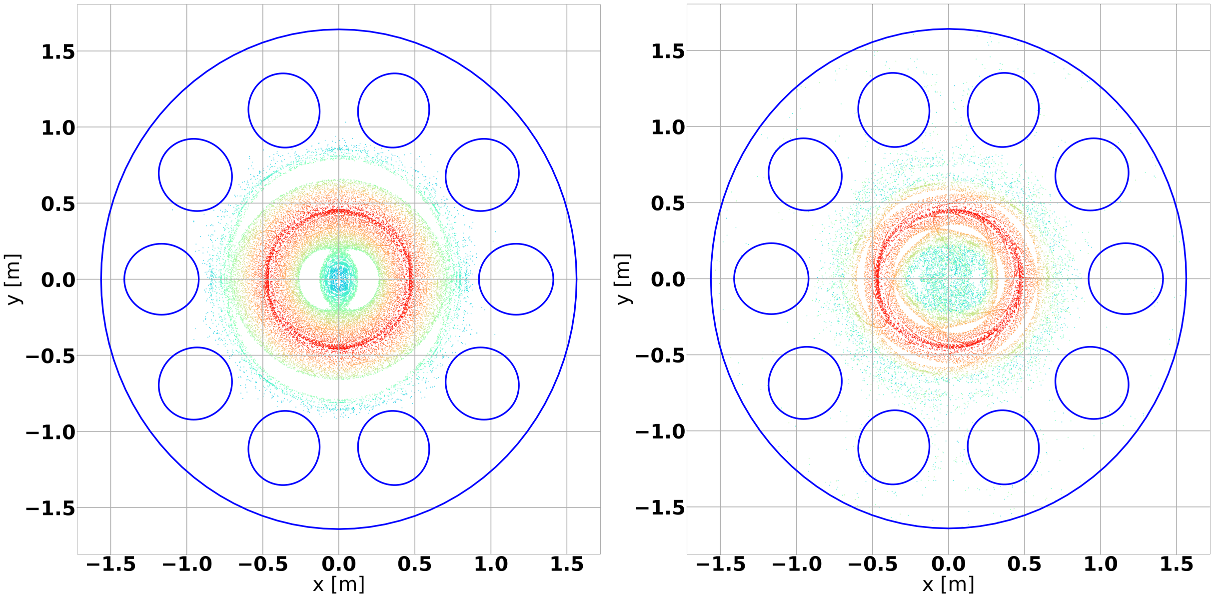

(a) Original Taylor state

(b) Injectors at n = 2, gain of 12

Figure 2.26: Poincaré plots of (composite) Taylor states in a ten-injector midplane manifold geometry (with cross-section as shown in Fig. 2.17b that has been elongated by a factor of 1.05 in the y-direction, producing a large n=2 island in the original Taylor state, as seen at left. With the injectors run in an n=2 pattern with a ratio of injector flux to spheromak flux of 12, the n=2 island is majorly suppressed, though replaced with a major n=5 component.

eliminated. The two types of boundary conditions are therefore capable of counteracting each other, at least under the composite Taylor state model. Potentially, an application of a further n=5 component to the imposed perturbations could reduce the n=5 islands, as well.

2.3.3 Distinguishing the impact of flux versus shape boundary conditions

In order to further disentangle the impact of flux boundary conditions from the influence of boundary shape, an additional test was run on the zero-injector HIT-SI volume (shown in Fig. 2.13 at lower right) to determine whether boundary nonaxisymmetries, such as those present in the preceding two subsections, are necessary for producing islands, or if magnetic boundary conditions alone are sufficient to produce magnetic islands.

To test this, two variations on the original axisymmetric zero-injector case were run: one including a "wall perturbation" as shown in Fig. 2.27, with the topmost surface, which was a ring with inner radius $R_1 = 25.33$ cm and an outer radius $R_2 = 40.35$ cm, displaced according to the following formula:

$$\Delta z = \alpha \frac{(R - R_1)(R_2 - R)}{(R_2 - R_1)^2} \cos(2\phi) \tag{2.4}$$

Where α is the perturbation amplitude, here equal to 5 cm. The CUBIT script for generating this geometry is given in Appendix B.

The result of this applied wall perturbation was a clearly-visible $n = 2$ island, as expected, and shown in Fig. 2.28:

While the resulting island is clearly visible, it is also neatly-defined and not especially voluminous; this is to be expected owing to the perturbation being a modification to just one of the curves that make up the volume's poloidal cross-section, and of an amplitude limited to less than a quarter of the spheromak's minor radius.

The case of the other kind of perturbation returned to geometric axisymmetry but put a flux boundary condition on that same surface instead of a physical displacement to it, with the usual $\boldsymbol{B} \cdot \hat{\boldsymbol{n}} = 0$ insulated-conducting boundary condition being replaced for that surface

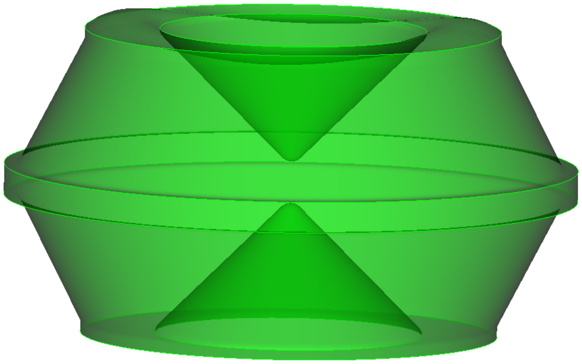

Figure 2.27: View of the modified zero-injector HIT-SI volume used for the evaluation of the noncomposite Taylor state shown in Fig. 2.28: the modification is to the uppermost surface, which has been displaced according to Eq. 2.4 from its original position, which spanned between major radii of $R_1 = 25.33$ cm and $R_2 = 40.35$ cm.

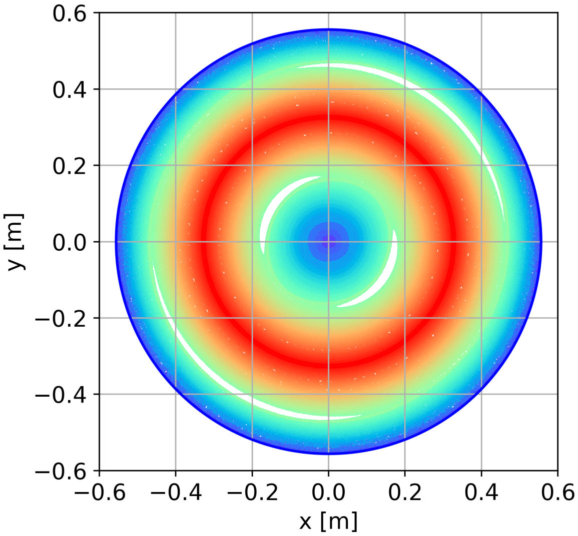

Figure 2.28: Poincaré plot of the XY plane for the “wall perturbation” case Taylor state, with the boundary perturbation applied as shown in Fig. 2.27 and described in Eq. 2.4.

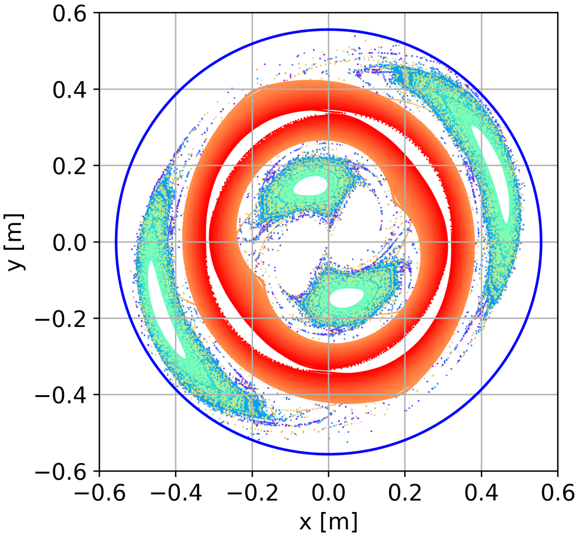

Figure 2.29: Poincaré plot of the XY-plane of the Taylor state in the axisymmetric (no-injectors) HIT-SI volume with a flux boundary condition defined in Eq.2.5 rather than being $\boldsymbol{B} \cdot \hat{n} = 0$ across the entire volume, showing the presence of an island and thus that boundary nonaxisymmetries are not necessary for island inducement.

with:

$$\boldsymbol{B} \cdot \boldsymbol{\hat{n}} = (R - R_1)(R_2 - R)\sin(\phi) \tag{2.5}$$

As the magnitude of the resulting equilibrium is arbitrary, no further amplitude normalization was applied. The result of this boundary condition was the equilibrium with the midplane Poincaré plot shown in Fig. 2.29:

This “wall flux” case results in an $n = 2$ island that is even more pronounced than the “wall perturbation” case, and demonstrates that flux boundary conditions do not need boundary nonaxisymmetries in order to produce islands.

This is to be expected: consider the “wall perturbation” case and suppose that the top ten centimeters were shaved off the flux conserver, with a flux boundary condition set on the new uppermost surface that is everywhere equal to the flux magnitude and direction at the corresponding point within the volume of the "wall perturbation" Taylor state. Below that plane, the resulting equilibria should appear exactly the same, as the hypothetical boundary within the "wall perturbation" case would be exactly transferred to the new real boundary on the "shaved top" case.

The effects of the presence of injectors, as seen in Fig. 2.14, could also be expressed as "flux boundary conditions" when dealing with magnetic equilibria only: if appropriately and accurately modeled, a boundary condition on a wall could substitute exactly for a nonaxisymmetric feature. This supports the practice of approximating helicity injectors in NIMROD simulations of SIHI experiments as boundary conditions where fluxes through the wall are defined[57].

2.4 Summary and conclusions

Taylor states, solutions to the equation $\nabla \times \boldsymbol{B} = \lambda \boldsymbol{B}$ subject to given boundary conditions, possess magnetic islands when those boundary conditions are sufficiently nonaxisymmetric, as the equilibria of stellarators do.

The mode-numbers and amplitudes of the islands are determined by the boundary shape, in the absence of flux boundary conditions beyond $\boldsymbol{B} \cdot \hat{\boldsymbol{n}} = 0$, and while the excited islands correspond well to particularly gross nonaxisymmetric features, they amount to a Fourier-type decomposition of the boundary shape in a base that corresponds to the spheromak inside rather than the flux conserver volume's shape, and so for small perturbations the island structures excited by a nonaxisymmetric feature can be complex compared to the feature's apparent simplicity.

This has implications for confinement for devices such as HIT-SI and its successor experiments, which seek to use nonaxisymmetric helicity injectors for current drive, in persuit of minimum-energy-with-conserved-helicity equilibria.

Nevertheless, the effects of boundary nonaxisymmetries can be limited by removing them from the spheromak region or by keeping them fine, and thus it is possible to have a Taylor state equilibrium in a boundary that includes helicity injectors without having significant islands in the spheromak core.

If such islands are desired, however, it is possible to create them using injector action, under the assumptions of the composite Taylor state model. Magnetic topology and profiles, at least in the ideal case, are capable of being altered by injector action.

Flux boundary conditions of other sorts than just helicity injector action also determine the shapes of the equilibria, and boundary shape nonaxisymmetry is not necessary to produce islands.

Whether and to what extent these nonaxisymmetric effects are present in full time-dependent MHD simulations are the subject of Chap. 4.

Chapter 3

HALL MHD SIMULATIONS OF THE HIT-SI EXPERIMENT AT MULTIPLE INJECTOR FREQUENCIES

3.1 Introduction

3.1.1 Testing the capabilities of the PSI-Tet 3D MHD Code

Numerical simulations of plasmas are useful for exploring and analyzing plasma behavior subject to the accuracy of the physics models used in the computations. However, the physical accuracy of the model must be traded off against computational tractability, with simpler models generally easier to calculate at the expense of physical accuracy.

Magnetohydrodynamics is a single-fluid plasma model well-established for the simulation of plasma experiments such as HIT-SI. Typical experimental parameters translate to a well magnetized plasma with an ion gyroradius of 8 mm[58] and modest Lundquist number (10^3 – 10^4)[59]. Inclusion of the Hall terms is motivated by an ion inertial length (8 cm)[57] comparable to experimental length scales such as the characteristic scale of the Taylor state (10 cm) and injector diameter (14 cm), and prior simulations[57, 60, 61]. The NIMROD code[62] in particular has been employed for HIT-SI simulations[57, 29], and the MHD model used in the simulations here has largely been tested in NIMROD simulations[61], but NIMROD's requirement that the plasma volume be axisymmetric means that the helicity injectors of HIT-SI, as previously shown in Fig. 2.2, cannot be directly included in such simulations. The MHD model used on PSI-Tet has also been tested through the GEM reconnection challenge[63], some results for which are presented in Appendix C.

The PSI-Tet code[64, 60, 28] is used for simulations of plasmas in complex volumes like the complete plasma volume of HIT-SI: it solves the extended MHD equations on unstructured tetrahedral grids using a high-order finite element method, and is capable of interfacing with

CAD software through the meshing software T3D[65] and CUBIT[55] so as to be able to model with gross geometric fidelity the plasma volumes of laboratory experiments such as HIT-SI. Fig. 2.2 shows the HIT-SI geometry and a corresponding PSI-Tet mesh used for the simulations presented here.

For the simulations presented here, two variants of the Hall MHD model shown previously in Eqns. 1.11– 1.18 are used, and explicated in Eqns. 3.1– 3.4: 1) a simplified version where density and temperature are uniform and constant ("zero-beta"), which omits the terms in blue and 2) the complete version where pressure effects are present ("finite-beta"). For the remainder of this chapter, the terms "finite-beta" and "zero-beta" will be used to refer to the full and simplified models, respectively.

$$\frac{\partial \boldsymbol{B}}{\partial t} = -\nabla \times \boldsymbol{E} \tag{3.1}$$

$$\frac{\partial n}{\partial t} + \nabla \cdot (n\boldsymbol{u}) = D\nabla^2 n \tag{3.2}$$

$$\rho \left[\frac{\partial \boldsymbol{u}}{\partial t} + \boldsymbol{u} \cdot \nabla \boldsymbol{u} \right] = \boldsymbol{J} \times \boldsymbol{B} - \nabla(2nkT) - \nabla \cdot \Pi \tag{3.3}$$

$$\frac{n}{\gamma - 1} \left[\frac{\partial T}{\partial t} + \boldsymbol{u} \cdot \nabla T \right] = -nkT\nabla \cdot \boldsymbol{u} - \nabla \cdot \boldsymbol{q} + Q/2 \tag{3.4}$$

With the following closures to Eqns. 3.1 — 3.4:

$$\begin{aligned} \boldsymbol{E} = (&-\boldsymbol{u} \times \boldsymbol{B} + \eta \boldsymbol{J} + \\ &\frac{1}{ne}(\boldsymbol{J} \times \boldsymbol{B} - \nabla nkT) + f_{m_e} \frac{m_e}{ne^2} \frac{\partial \boldsymbol{J}}{\partial t} \Big) \end{aligned} \tag{3.5}$$

$$\boldsymbol{q} = -n \left[\chi_{\parallel,e} \hat{\boldsymbol{b}}\hat{\boldsymbol{b}} + \chi_{\perp,i}(I - \hat{\boldsymbol{b}}\hat{\boldsymbol{b}}) \right] \cdot \nabla T \tag{3.6}$$

$$Q = \eta \boldsymbol{J}^2 - (\nabla \boldsymbol{u})^T : \Pi \tag{3.7}$$

$$\Pi = -\nu(\nabla \boldsymbol{u} + (\nabla \boldsymbol{u})^T - \frac{2}{3} I \nabla \cdot \boldsymbol{u}) \tag{3.8}$$

The Hall term is of particular interest in simulations of HIT-SI as a postulated mechanism of its current drive is expected to depend on the Hall effect[22], and its inclusion has been found in NIMROD simulations to improve agreement with experiment[61]. Additionally, the inclusion of finite beta with Hall physics enables capturing important diamagnetic effects[66, 67]. The MHD models for PSI-Tet and NIMROD simulations of HIT-SI are identical with the exception of numerical $\nabla \cdot \boldsymbol{B}$ cleaning[62] and a small hyper-diffusivity ($D_H = 10^{-4}$ m^4/s^2) that are used in NIMROD and not PSI-Tet, making the version of Eq. 3.2 used in NIMROD simulations

$$\frac{\partial n}{\partial t} + \nabla \cdot (n\boldsymbol{u}) = D\nabla^2 n + \nabla^2 D_H \nabla^2 n \tag{3.9}$$

For more information on the NIMROD implementation see Refs. 62 and 29 .

For this work local anisotropic thermal conduction coefficients are determined by a classical Braginskii thermal conduction model[68] with both magnetization and temperature dependence[69]. Approximated Spitzer resistivity[70] of the form $\eta = \eta_0 T_e^{-3/2}$, and fixed isotropic viscosity were used. Both PSI-Tet and NIMROD use the full 3D form of thermal conduction and resistivity. The artificial diffusivity D is included to avoid numerical issues with unresolved oscillation at the grid scale.

3.1.2 HIT-SI Injector Frequency Scan

As experimental results have indicated increased plasma pressures at higher frequency on HIT-SI[25], simulating temperature and density evolution in HIT-SI is of interest in exploring its dynamics. In order to compare the effects of the inclusion of temperature and density evolution on PSI-Tet simulations, as well as to compare the results of PSI-Tet simulations to previous results[60], similar datasets from experiment[25, 71] and simulations[72, 29] with the NIMROD code[62, 73], the simplified model where density and temperature are uniform and constant ("zero-beta") will be used for comparison. These models and experimental results are applied to a scan of injector frequency in four steps: 14.5 kHz, 36.8 kHz, 53.5 kHz, and 68.5 kHz; each case will be referred to in this chapter by the truncation of its frequency value to an integer value in kHz. These frequencies correspond to the range of best-performing experimental shots, with the highest-magnitude toroidal currents (∼90 kA[71]) obtained at "low frequency" (here meaning 14 kHz) and the highest current gain ($G = I_{tor}/I_{inj}$) of 3.9[25] at "high frequency" (68 kHz).

Dirichlet boundary conditions, equal to the initial conditions were used for density, temperature, and velocity (zero flow). While the PSI-Tet initial temperature was 3.0 eV exactly, the NIMROD initial temperature was 3.31 eV; this was the only difference in the simulation conditions besides those required by the differences between the codes. An insulated-conductor boundary condition, where $J_\perp = 0$ and $B_\perp = 0$, in conjunction with injector drive, was used for the magnetic field. For more information on the boundary condition see Ref.60. A deuterium plasma is simulated, with enhanced electron inertia(f_{m_e}=36.72) in Eq. 3.5 equivalent to $m_i/(f_{m_e} m_e) = 100$. This term, which is enhanced compared to its nominal value, is included to improve the condition number of the system of equations with the Hall term. The specific value of the enhancement factor is the highest value possible without significant impact on the solution as determined by previous parameter scans[57, 60, 61]. Injector current and voltage were held constant across injector frequencies. Other parameters of interest, chosen to roughly match conditions in 68 kHz experimental shots, are given in Table 3.1, and were held in common for the PSI-Tet and NIMROD simulations.

For the PSI-Tet simulations, the tetrahedral HIT-SI mesh used is as shown in Fig. 2.2, with an average cell size of 2.8 cm with a polynomial degree of 3. For the NIMROD simulations, the average cell size in the poloidal plane was 1.8 cm with a polynomial degree of 4 and 11 Fourier modes in the toroidal direction, corresponding to a toroidal node spacing of approximately 8.3 cm at the mid-radius of the domain (sim27.5 cm). Grid resolution studies for both PSI-Tet[60, 28] and NIMROD[57, 29] have shown convergence of results at these resolutions.

A key difference in these simulations is that PSI-Tet directly models the injector regions,

Table 3.1: Common parameters for PSI-Tet simulations

Parameter	Value [Units]
Injector flux (ψ)	0.5 [mWb]
Injector current (I)	8 [kA]
Initial density (n)	0.75×10^{19} [m^{-3}]
Initial temperature (T)	3 [eV]
Viscosity (ν)	550 [m^2/s]
Diffusivity (D)	250 [m^2/s]
Reference resistivity (η_0)	5.327×10^{-4} [Ohm-m $\mathrm{eV}^{\frac{3}{2}}$]

which are included in the unstructured tetrahedral grid along with the main flux conserver volume, while NIMROD does not. In the NIMROD simulations, the injector fields are instead modeled through magnetic boundary conditions on the main flux conserver volume, while density, temperature and velocity are held fixed at their wall values across this interface. This prevents coupling "through" the injector volumes and also produces significantly different profiles for the plasma fluid quantities across the injector mouths, which show significant variation from the wall values in PSI-Tet simulations. For more information on the boundary conditions used in NIMROD simulations of HIT-SI, see Ref. 57, and for PSI-Tet boundary conditions, see Ref. 60.

The value of the uniform isotropic artificial diffusivity D given in Table 3.1 is the lowest possible value while avoiding numerical issues for this frequency scan, as determined by a parameter scan, and significantly lower than was used in previous work[61]. Dynamics appear relatively insensitive to the value of this term; a detailed study of this and other chosen parameters will be presented in a paper to follow.

3.1.3 Organization of this chapter

The remainder of this chapter will be organized as follows: a comparison between the zero-beta and finite-beta models will be presented in Section 3.2, including evaluations of temperature dynamics (Sec. 3.2.1), density dynamics (Sec. 3.2.2), and current gain (Sec. 3.2.3), and this will be followed by comparison of both models' results to experimental data and NIMROD simulations in Section 3.3, through the comparison of current gain behavior (Sec. 3.3.1), internal magnetic probe results (Sec. 3.3.2), current centroid behavior (Sec. 3.3.3), and analysis using biorthogonal decomposition and Fourier decomposition of surface probe measurements (Sec. 3.3.4).

3.2 Comparison of finite-beta and zero-beta models

While the HIT-SI experiment has been modeled before[74, 72, 29], including its complete volume using PSI-Tet[60], presented here are the results of the first set of simulations that evolve the continuity and energy equations (Eqns. 3.2 and 3.4), enabling explorations of the effects of temperature and density dynamics on current-drive performance, and of the temperature and density behaviors inside the injectors.

PSI-Tet is capable of exploring local temperature dynamics throughout the entire volume of HIT-SI, including through the injectors. For the purpose of a direct comparison between finite-beta simulations and zero-beta simulations of the type shown in Ref.60, a new set of zero-beta simulations was run with uniform resistivities set to levels equivalent to the final average temperatures of the corresponding finite-beta simulations, as shown in Fig. 3.2 (6.4 eV, 8.3 eV, 9.9 eV, and 11.2 eV). The exception being the 14 kHz zero-beta simulation, which failed to start up (current gain greater than 1) at its corresponding finite-beta simulation's final average temperature, and so a higher temperature of 7.4 eV equal to the midpoint of the final average temperatures reached by the finite-beta 14 kHz and 36 kHz simulation was used.

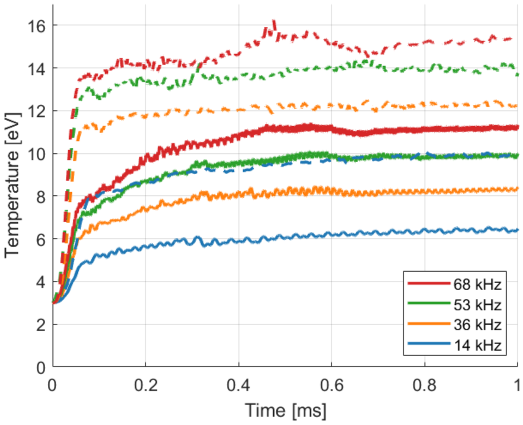

Figure 3.1: Average (solid lines) and maximum (dashed lines) temperature for finite-beta PSI-Tet simulations versus time. The maximum temperatures have been low-pass filtered at twice the injector frequency.

3.2.1 Temperature dynamics

Starting from an initial condition of 3 eV, after a steep rise corresponding to the initial injector ramp, all finite-beta PSI-Tet simulations see increases in average temperature as the simulation continues, as shown in Fig. 3.1. Average temperatures level off near the halfway point of the simulation and remain steady after that, with only minor oscillations corresponding to injector action. Final average temperatures rise linearly from 6.4 eV for the 14 kHz finite-beta PSI-Tet simulation to 11.2 eV for the 68 kHz PSI-Tet simulation as shown in Fig. 3.2.

Fig. 3.3 shows the plasma temperature on a cross-section of the simulation domain for the 14 kHz and 68 kHz simulations for the same phase in the injector cycle. Of note are the hot regions in both the main volume as well as in the injectors: the peak temperatures in the injectors rise with the peak temperatures in the main volume with frequency as well as with time.

Peak temperatures within the volume at 1 ms into the simulation increase monotonically

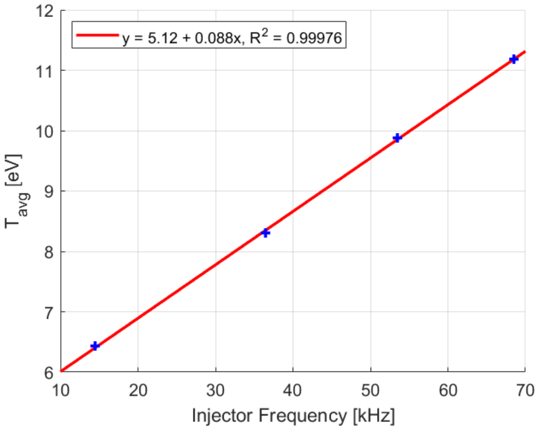

Figure 3.2: Average temperature at the end of the simulated millisecond for finite-beta PSI-Tet

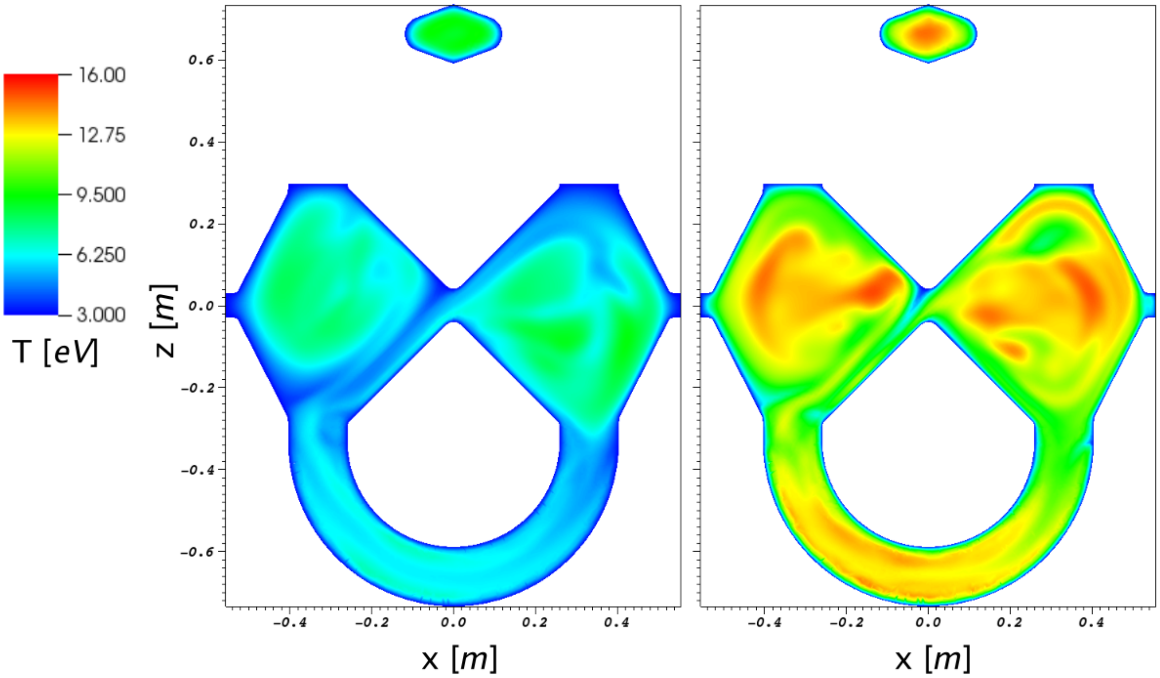

Figure 3.3: Temperature slice plots at the same phase in the injector cycle at approximately 1 ms into 14 kHz (left) and 68 kHz (right) frequency finite-beta PSI-Tet simulations of HIT-SI

from 9.3 eV in the 14 kHz case to 15.1 eV in the 68 kHz case. Peak temperatures in the injectors and the main volume increase at the same rate, suggesting that, in these simulations, the increases in temperature and current gain are primarily due to an increase in power injection (as power injection is proportional to injector frequency with fixed injector current[75]) and not an increase in energy confinement. This is in contrast with experimental results, which see higher current gain (expected to correlate with temperature due to conductivity) with lower power injection as the injector frequency increases[76]. Visible in both cases in Fig. 3.3 is a relatively-hot central region that resembles in shape the closed-flux spheromak regions identified in composite Taylor analysis[14]. Surrounding it is a region in which channels of higher temperature form, linking to the injector mouths, appearing on opposite sides of the spheromak from each mouth every cycle. As shown, the remnants of channels are visible in the lower-left inboard, connecting to the $-x$ injector mouth. Due to the oscillations of the injector fields, these connections appear and disappear in regular cycles. The 'disconnection' part of this cycle can be clearly seen in the 14 kHz case of Fig. 3.3, showing the complicated 3D connectivity that exists through the injectors.

These large variations in temperature and corresponding plasma conductivity cannot be captured the zero-beta model. The fact that channels of plasma of temperature significantly higher than the final mean temperature exist throughout the finite-beta simulations is likely responsible for some of the observed differences in current-drive performance between the two models, presented in section 3.2.3.

3.2.2 Density dynamics

A consistent finding for all finite-beta PSI-Tet simulations, shown in Fig. 3.4 is that the average density rises during startup and then falls below the initial/boundary condition in agreement with experimental observations early in discharges. While the 14 kHz case levels off relatively close to the initial condition, the three higher-frequency cases all approach the same value of 6×10^{18} m^{-3} as of the end of the simulation, and the oscillations in total density diminish monotonically with frequency.

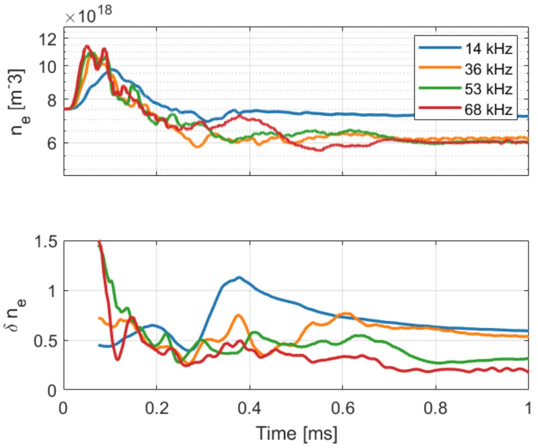

Figure 3.4: Time-averaged (top) and relative oscillation amplitude (bottom) of volume-averaged density for finite-beta PSI-Tet HIT-SI simulations

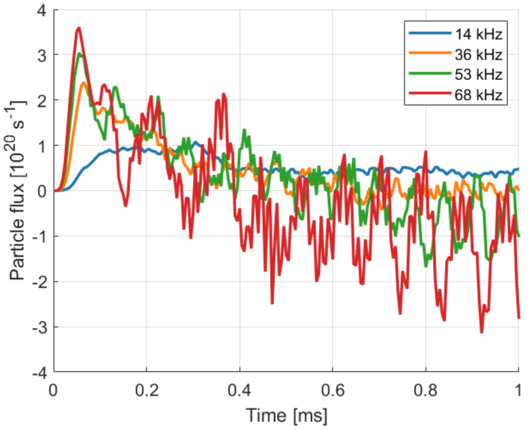

Figure 3.5: Particle flux through all four injector mouths for the four finite-beta PSI-Tet HIT-SI simulations

The increase in density early in time, before spheromak formation, suggests that the injectors are a source of density. To investigate this, the particle flux through the injector mouths, which cannot be measured in experiment and must be specified as boundary conditions in NIMROD simulations, is sampled. Fig. 3.5 shows the total net particle flux, low-pass filtered at the respective injector frequencies, into the main confinement volume through all four injector mouths for the four finite-beta PSI-Tet simulations, indicating that there is an initial burst of net particle flux into the main volume from the injectors at all frequencies at the beginning of the simulations, and the net particle flux decreases as the shot continues. As the frequency increases, the particle flux reverses late in the simulations.

In addition, the net particle flux through the injector mouths is observed to develop an oscillation with increasing injector frequency with a frequency well below the injector frequency. As the 53 kHz and 68 kHz curves show, the frequency of these oscillations decreases with increasing injector frequency, in contrast to other observed phenomena.

This marks a point of interest for future studies of injector dynamics, particularly as the density flux is expected to generally flow out of the injectors in the experiment due to fueling; further attempts to investigate injector density dynamics should include fueling and more detailed comparisons of synthetic interferometer measurements to experimental data. Once this phenomenon is fully understood and validated, it may be used to improve boundary conditions for NIMROD simulations.

Similar evolution is also seen on density at points along the experimental interferometry chord, located as shown in Fig. 3.7 evaluated from PSI-Tet simulations. Fig. 3.6 shows an initial surge in density observed at all frequencies. Additionally, spatial variation in the amplitude of density oscillations is observed to become more pronounced with increasing frequency, with Fig. 3.6d showing two changes in the location of low-density regions at approximately 0.4 and 0.6 ms, well after startup, indicating that at high frequencies, density behavior does not settle qualitatively into stable cycles immediately after startup, but that gross changes in the dynamics occur well into the simulations.

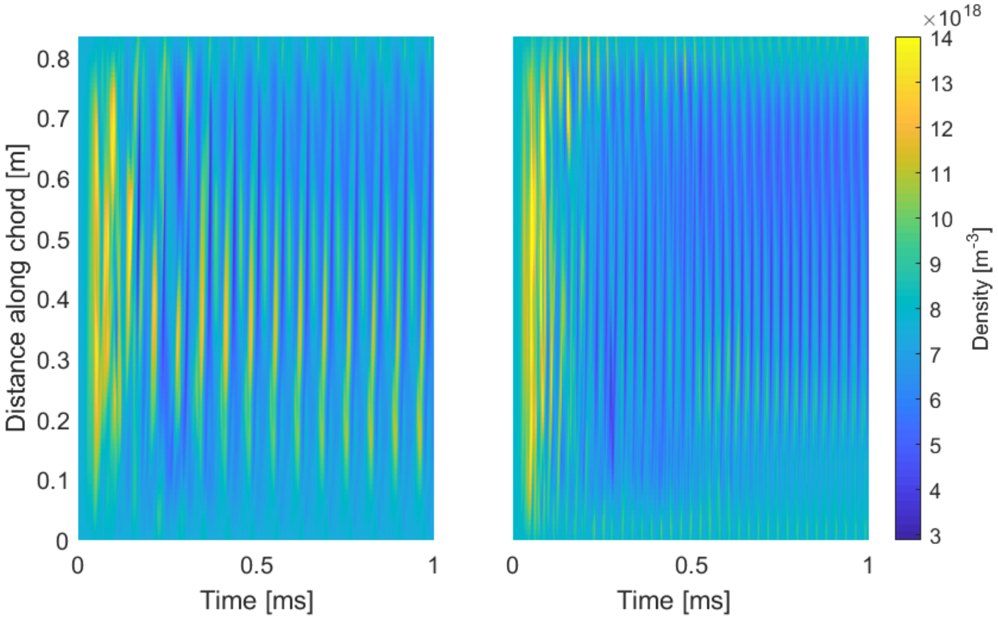

(a) 14 kHz (b) 36 kHz

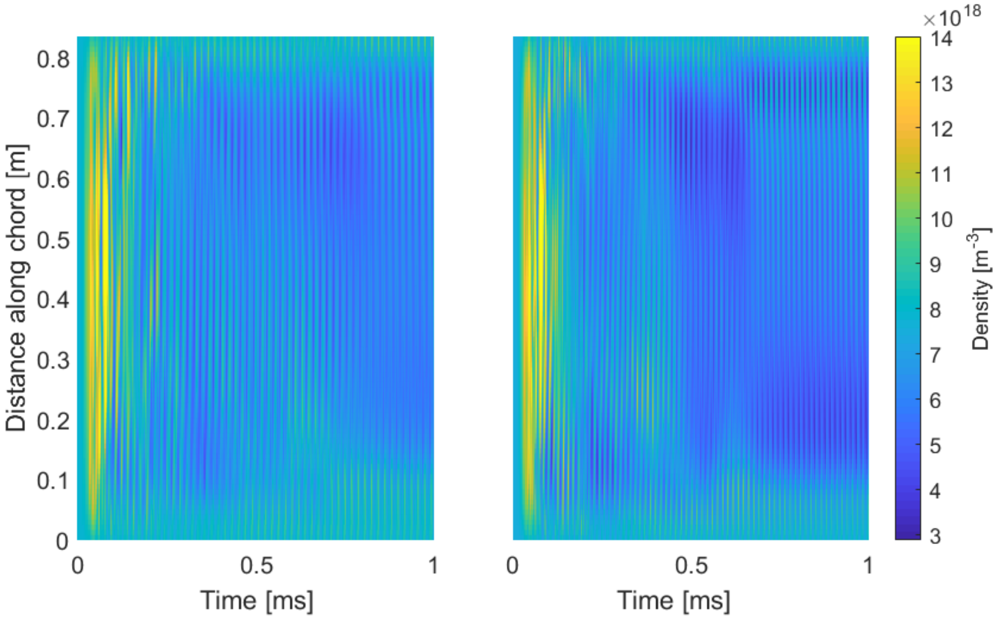

(c) 53 kHz (d) 68 kHz

Figure 3.6: Density values along the interferometer chord (shown in Fig. 3.7) from the finite-beta PSI-Tet simulations.

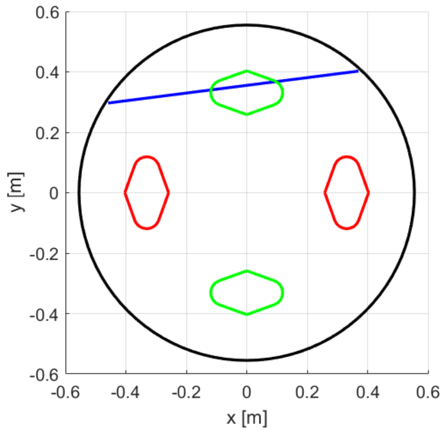

Figure 3.7: Location of the interferometer chord on the HIT-SI midplane, with the zero-point in Fig. 3.6 at left.

3.2.3 Current Gain

Fig. 3.8 shows that current gain increases with increasing injector frequency under both zero-beta and finite-beta models. However, much of the zero-beta increase is due to the lower specified resistivity at higher frequency, while the finite-beta simulations reach both their temperatures and current gains self-consistently from the same initial conditions.

The zero-beta simulations all level off after approximately half a millisecond, while the finite-beta simulations follow the zero-beta simulations closely until breaking away into continued growth. These transitions correspond roughly in time with a change in Fourier mode spectra, as discussed in Sec. 3.3.4. The 36 and 53 kHz simulations show this transition occurring at approximately the same time but at different gains, while the 68 kHz case transitions earlier, as does the 14 kHz case, though the low-gain steady-state of the zero-beta 14 kHz case interferes with its ability to be used as a marker. Among the finite-beta cases, only the 14 kHz simulation appears to be nearing steady-state by the end of the simulated millisecond; the other finite-beta cases show continued growth until the end of the simulations. This is in contrast to the behavior of the average temperatures (Fig. 3.1) which see no such

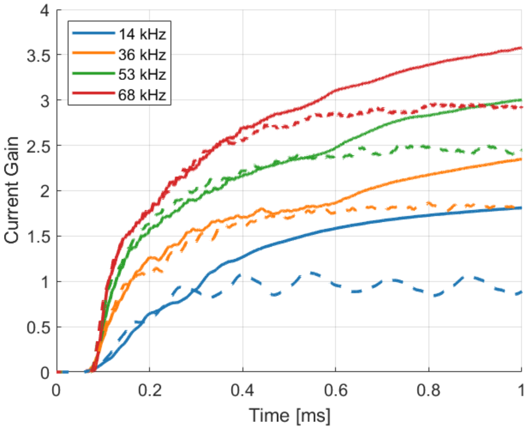

Figure 3.8: Cycle-averaged current gain for PSI-Tet finite-beta (solid lines) and zero-beta (dashed lines) simulations.

continued growth, which indicates that, since the higher currents are not producing higher average temperatures, the current distribution is likely changing, as the temperature profiles in Fig. 3.3 may display.

3.3 Comparisons to experimental data and NIMROD simulations

Of even greater interest than how the two models compare to each other is how either one compares to experimental data. Diagnostics used on the experiment to gather that data include an array of surface magnetic probes, (arranged as shown in Fig. 3.9) and an internal magnetic probe extending from the outboard midplane to the approximate radius of the magnetic axis, also as shown in Fig. 3.9. Synthetic versions of both of these probe arrays are included in PSI-Tet and NIMROD simulations. These probes are the primary diagnostics used to study HIT-SI and for comparisons of datasets.

3.3.1 Current Gain

The observed trend in both models is that the current gain, increases with increasing injector frequency, matching the observed experimental trends, as shown in Fig. 3.10.

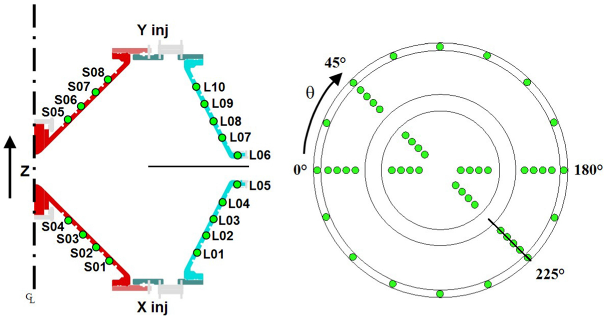

Figure 3.9: Poloidal (left) and toroidal (right) locations of the surface magnetic probes. Also shown (in black) is the location of the internal magnetic probe array, at the toroidal angle of 225°.

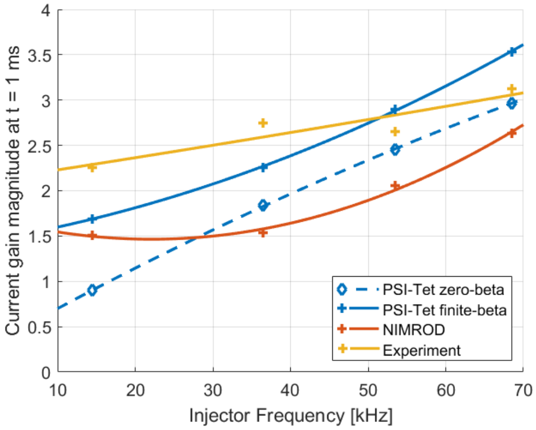

Figure 3.10: (Cycle-averaged) current gain at 1 ms versus frequency for finite-beta (solid) and zero-beta (dashed) PSI-Tet, NIMROD, and experimental data. Equations for the best-fit quadratic curves are given in Table 3.2.

Table 3.2: Best quadratic fit curves ($y = ax^2 + bx + c$) for Fig. 3.10

Source	a	b	c	R^2
PSI-Tet zero-beta	-1.2×10^{-4}	0.048	0.23	0.99993
PSI-Tet finite-beta	2.5×10^{-4}	0.014	1.43	0.9996
NIMROD	5.5×10^{-4}	−0.024	1.73	0.994
Experiment	1.4×10^{-4}	0.013	2.10	0.838

The experimental shots are not direct matches to the frequency-scan simulations, most pertinently in that the injectors were run at higher power at lower frequencies, while in the simulations, injector flux and current were held constant across frequencies.

Nevertheless, the experimentally-observed trend of increasing current gain with injector frequency is observed in all MHD simulations. The PSI-Tet trends show a stronger dependence on frequency than the other two; for the NIMROD simulations, as they use the same conditions (except the aforementioned 10% greater boundary temperatures) as the PSI-Tet simulations, the difference in current gain is likely due to the different models of injector action. In particular, the temperature and resistivity at the injector mouths is likely to affect the temperatures and current gains reached.

Fig. 3.10 shows quadratic fits to the final current gain values versus frequency, (equations given in Table 3.2, with y in eV and x in kHz,) and of particular note is the difference in concavity between the fits to the zero-beta and finite-beta PSI-Tet simulations. The finite-beta simulations increase faster with increasing frequency than the zero-beta simulation and this suggests that some of the increase in current gain in the finite-beta simulation is due to the evolution of the current profile through changes to resistivity that temperature evolution permits.

The source of the differences between experimental and simulated datasets is less easy to discern, as the input power increased with decreasing injector frequency. Direct comparison

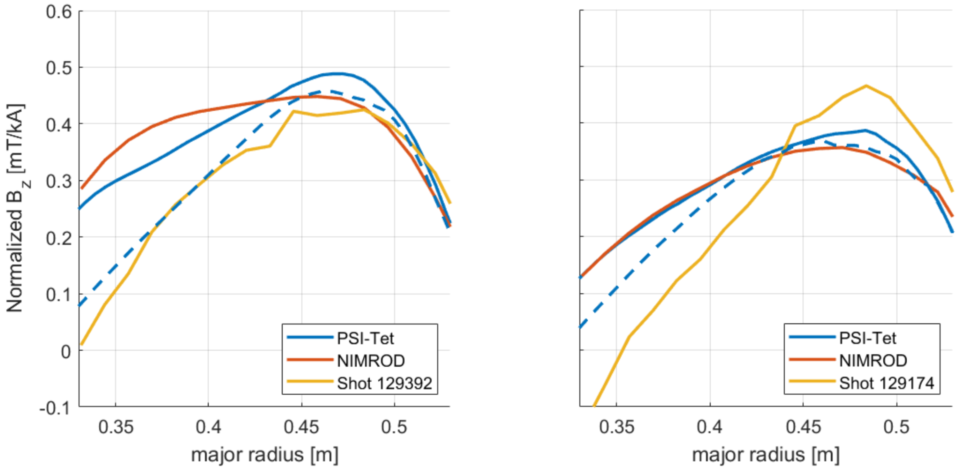

(a) 14 kHz

(b) 68 kHz

Figure 3.11: Mean magnetic field profiles (normalized by toroidal current) along the internal probe at 1 ms from finite-beta (solid) and zero-beta (dashed) PSI-Tet, NIMROD, and experimental data.

requires more detailed validation simulations where injector power is matched[64], and may also require a more complete model of the injector circuits[77], both of which will be explored in future work.

3.3.2 Internal Magnetic Probe Profiles

HIT-SI's internal magnetic probe (IMP) extends inward from the outboard midplane to the approximate location of the magnetic axis: as can be seen in Fig. 3.9, and provides a direct source of magnetic field measurements in the interior of HIT-SI. A simulated version of the probe has been implemented in PSI-Tet, with greater radial extent and spatial resolution than the real probe.

Fig. 3.11 shows time-averaged magnetic field measurements in the z-direction B_z from both experimental shots and simulations, averaged over the final five (three for the 14 kHz case) injector cycles before 1 ms in order to extract the mean fields corresponding to the spheromak equilibrium. Zero-crossings of these curves should correspond to the radial location of the magnetic axis for the mean field equilibrium for each case.

The zero-crossing is observed to be significantly further outward for the experimental data than it is for any of the MHD simulations, and it also sees an outward shift with increasing frequency, while the MHD simulations of all types do not see any monotonic trends in the behavior of the zero-crossing of their poloidal magnetic field profile, with their zero-crossings remaining largely at the same radial positions without consistent changes in direction across all four simulated frequencies.

However, the 14 kHz case deviates from the others in seeing the zero-crossings for the finite-beta simulations be significantly farther inward than they are at any other frequency, or for the zero-beta simulation and experimental measurements at the same frequency. Finer investigations may reveal whether the 14 kHz result was an outlier or a sign of a trend similar to the outward shift seen on experiment.

3.3.3 Current Centroid Position

Similar trends to the behavior seen on the IMP datasets are seen in the behavior of the current centroid[25]. The behaviors seen in PSI-Tet simulations, shown with NIMROD and experimental data in Fig. 3.12, are broadly similar to each other, but there is a pronounced difference between simulations and experiment.

The current centroid is the weighted average of the poloidal field measurements from the surface magnetic probe array; the radial position of the current centroid is computed for each of the four poloidal slices as (from Ref.25:)

$$R_c = \frac{\sum_{i=1}^{16} R_i B_{pol,i}}{\sum_{i=1}^{16} B_{pol,i}} \tag{3.10}$$

One significant experimental finding was that the current centroid was observed to shift outward and become more symmetric with increasing frequency. This effect is consistent

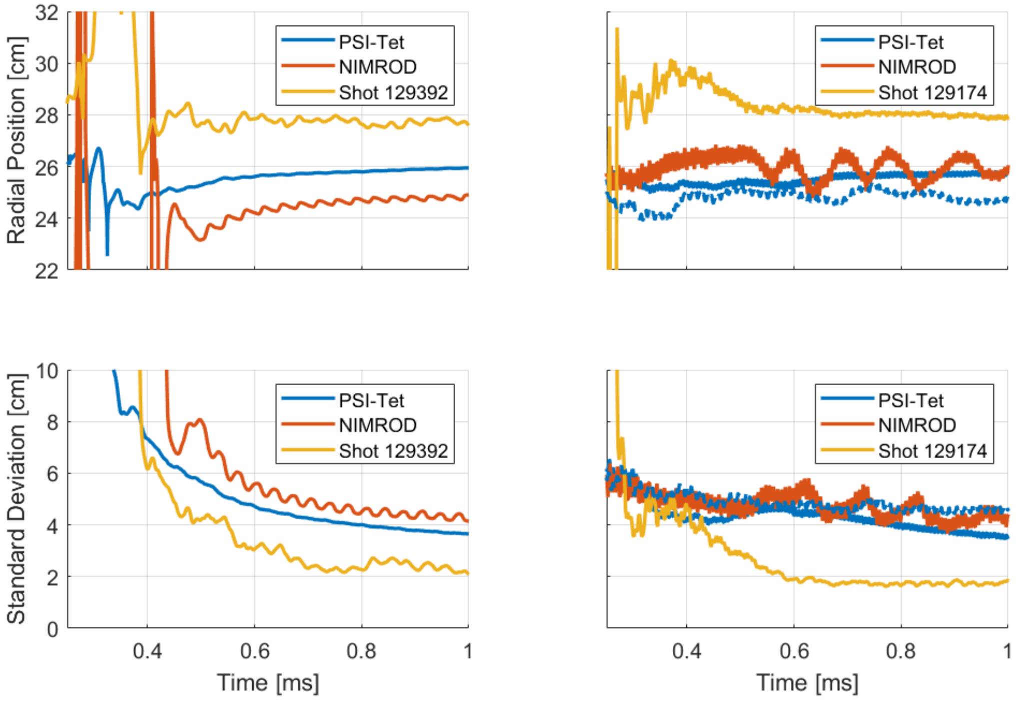

(a) 14 kHz

(b) 68 kHz

Figure 3.12: Radial positions and standard deviations of the current centroids, as computed from surface probe data, for finite-beta (solid) and zero-beta (dashed) PSI-Tet, NIMROD, and experiment for the lowest and highest injector-frequency cases. The 14 kHz zero-beta PSI-Tet case is omitted as it did not reach sufficient gain for the calculation.

with a Shafranov shift[25] and so indicates that there may be confined pressure in HIT-SI discharges at high frequency.

However, there is neither significant confined pressure in the finite-beta PSI-Tet simulations, nor is there any similar trend in the behavior of the current centroid. Additionally, the oscillations observed of that current centroid are much greater in amplitude than the experimental oscillations are, and further, there is no observed trend in the outward shift of the current centroid with increasing frequency in either PSI-Tet or NIMROD. There is a trend dependent on time but not frequency observed in the simulations: the simulations see improved symmetry as time continues.

Another possible explanation for shifts in the current centroid seen experimentally are non-pressure related changes in the current profile. However, PSI-Tet simulations see no significant trends in centroid position with frequency despite significant changes in resistivity and current profiles. This is consistent with the interpretation of the observed shift as pressure related.

3.3.4 Mode-Subtracted Fourier Decomposition

Most of the information on the magnetic field and current structures within the HIT-SI experiment are obtained from the surface magnetic probe signals, including information about the toroidal current being driven, as the simply-connected plasma volume does not enable the use of a Rogowski coil, commonly used in other toroidal plasma devices.

Biorthogonal Decomposition (BD)[78] is a tool for analysis of large datasets, such as measurements from experimental data arrays[79, 80] and simulated datasets[81] that cannot be easily analyzed signal-by-signal or all at once, and has been employed for analysis of the measurements from HIT-SI's surface probe array[82] and simulations thereof[60]. BD uses singular value decomposition to decompose the signals into an ordered sequence of modes, each with a corresponding temporal evolution ("chronos") and spatial structure ("topos"). For HIT-SI shots, the most-prominent time-evolution observed (the "first chrono") is observed to correlate with the toroidal current in the main plasma volume, and the second and

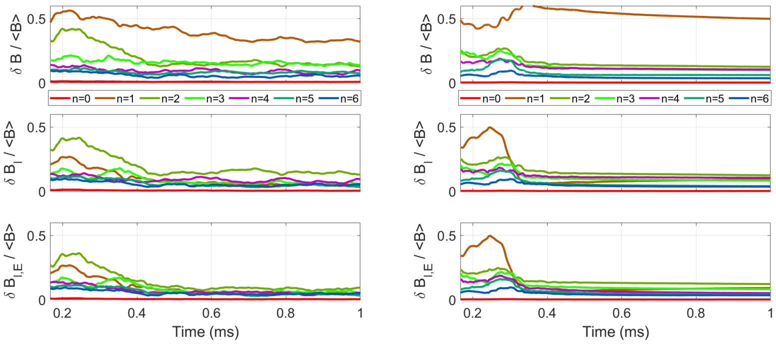

(a) Shot 129392 (b) Finite-beta PSI-Tet

Figure 3.13: Fourier spectra of 14 kHz datasets, showing, top row to bottom, in each subfigure: row 1: perturbation Fourier spectrum normalized to the mean magnetic field (with toroidal mode numbers given in the legend located between the first and second rows); row 2: normalized perturbation spectrum of modes obtained from Fourier decomposition of the dataset with injector-correlated BD modes subtracted (see Eq. 3.11); row 3: As row 2, with equilibrium-correlated BD modes also subtracted (see Eq. 3.12).

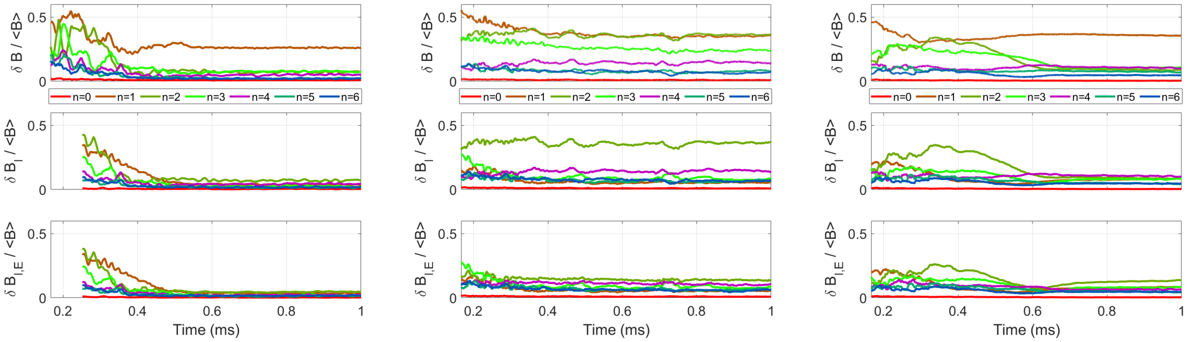

(a) Shot 129174 (b) Zero-beta PSI-Tet (c) Finite-beta PSI-Tet

Figure 3.14: Fourier spectra of 68 kHz datasets, with the contents of the subfigure rows as in Fig. 3.13.

third chronos correlate with the injector perturbations[82]. These time correlations enable the isolation of the different components, enabling the toroidal current or injector current-correlated components to be inspected directly, or for the remainder of the signal, with the toroidal current and/or injector modes subtracted out, to be analyzed.

The set of surface magnetic probes arranged around the outboard midplane enables the analysis of toroidal Fourier components of the field up to n=7, and this Fourier decomposition enables investigation of the toroidal mode spectrum of each isolate perturbation set. This is performed using an analysis algorithm previously discussed in Ref. 71. This modal analysis is not meant to identify or diagnose potential instabilities in the experimental or simulated plasmas. Instead it is meant to identify similarities and differences in field structure between experimental and the two numerical models by utilizing BD modes to filter out specific field components from the full signals.

Specifically, the injector-correlated BD modes can be subtracted out from the total fields as shown, and the toroidal mode spectrum of the uncorrelated remainder can be analyzed:

$$\delta B_I = \sum_{i \neq 2,3} \delta B_i \text{ for BD modes } \delta B_i \tag{3.11}$$

Additionally, the injector- and equilibrium-correlated BD modes can also be subtracted out, for investigation of activity correlated with neither injector activity nor spheromak evolution:

$$\delta B_{I,E} = \sum_{i \neq 1,2,3} \delta B_i \text{ for BD modes } \delta B_i \tag{3.12}$$

Figures 3.13 and 3.14 show that, experimentally, when the injector-correlated BD modes are subtracted out, the n=1 component is significantly reduced. With the toroidal current-correlated mode also subtracted out, only modes that are correlated with neither the toroidal current nor with injector frequency are left behind, and their amplitudes suggest the presence and strength of possible self-generated plasma activity, such as instabilities.

Fig. 3.14 shows that, for the 68 kHz case, experimentally lower amplitudes are observed for all mode numbers before and after any mode subtraction is done than on PSI-Tet, particularly for the zero-beta case. The finite-beta case sees a transition to lower mode amplitudes from approximately 0.4-0.6 ms while the zero-beta case does not, corresponding to the period of deviation in which the toroidal current in the zero-beta case plateaus while the toroidal current of the finite-beta case continues to grow. Even after this transition, and with the injector- and equilibrium-correlated BD odes subtracted out, there is still much more mode activity (particularly in n=2) for the finite-beta case than there is in the experimental shot. PSI-Tet simulations also see the relative dominance of the n=4 component in the injector-subtracted case, unlike on experiment, where n=4 is always at a lower amplitude than n=2.

Fig. 3.13 shows that, for the 14 kHz case, the differences between experimental and simulated mode spectra are partially reversed: aside from the greater n=1 amplitude in the PSI-Tet case, the mode amplitudes before subtractions are approximately the same between PSI-Tet and the experimental shot, and only once the toroidal current-correlated BD mode is subtracted out do the experimental mode amplitudes become clearly lower than the PSI-Tet mode amplitudes.

Additionally, the PSI-Tet mode amplitude curves are significantly smoother in time for both frequencies than the experimental curves are: there is high-frequency activity in the mode amplitudes (visible especially in Fig. 3.13a as being higher-frequency than injector action) that is not captured by the PSI-Tet simulations.

3.4 Conclusions and Summary

The results of a simulated scan of injector frequency in the HIT-SI experiment that includes temperature and density evolution using the 3D MHD code PSI-Tet have been presented, and have been compared to similar datasets, including zero-beta PSI-Tet in Section 3.2 and experimental shots and NIMROD simulations in Section 3.3.

The comparisons between finite-beta and zero-beta models in Section 3.2 found that average temperature rises linearly with frequency with constant injector current and flux. Additionally, above a threshold injector frequency (between 36 and 53 kHz), the inclusion of dynamic density is found to result in oscillations in particle flux through the injector mouths at frequencies lower than the injector frequency. Simulations using the finite-beta model are found to reach higher current gains than zero-beta simulations with equivalent average resistivity, and experience continued growth in the toroidal current after the zero-beta equivalents have reached steady-state, implying continued evolution of the current profile. The finite-beta 68 kHz PSI-Tet simulation is also found to see a transition in its mode spectrum, correlating in time to its transition to steady toroidal current growth not seen in the zero-beta case.

Comparisons between PSI-Tet and experimental shots and NIMROD simulations in Section 3.3 found that, in agreement with experimental trends, current gain increased with increasing injector frequency, though direct comparisons to experiment require further, more detailed validation owing to the differences in input power. Neither internal magnetic profiles nor current centroid measurements on PSI-Tet or NIMROD simulations showed the experimentally-observed outward shift with increasing frequency, nor did the simulated current centroid measurements show the experimentally-observed decrease in standard deviation, further implying that the experimental trends are not due to changes in the current profile but possibly pressure confinement. Similarly, in Section 3.3.4, mode-subtracted Fourier analysis found that high-frequency HIT-SI experimentally shows fewer signs of self-generated plasma activity than simulations have been able to capture, as PSI-Tet simulations see higher toroidal mode amplitudes even after injector and toroidal-current BD mode subtraction.

To investigate these discrepancies, future work should further look at the temperature models, including separate ion and electron temperatures[83, 84], to explore the effects of more physical features on the results of simulations of SIHI experiments. Further validation simulations[64] matching more features of experimental shots should be performed to clarify any differences in current-gain scaling.

Chapter 4

EXPLORATION OF THREE-DIMENSIONAL EFFECTS ON SIMULATED SIHI INJECTOR CONFIGURATIONS

4.1 Combining what came before

The two previous sections have focused on two major themes: the effects of boundary shapes and magnetic boundary conditions on the equilibria contained within the evaluated volumes in Chapter 2, and the use of PSI-Tet's finite-pressure, single-temperature Hall MHD model for a scan of a single variable's influence upon device performance.

Let those two themes now be joined in an attempt to explore the effects of three-dimensionality on the simulated behavior of SIHI devices under the finite-pressure, single-temperature Hall MHD model used in PSI-Tet.

The question to be addressed, primarily, is this: are effects due to boundary shapes on the time-dependent plasma simulations observed, and if so, do they correlate at all with the effects observed in Taylor state equilibria as shown in Chap. 2? That is, do the effects observed in the Taylor state equilibria have analogues in the time-dependent MHD simulations? For example, do the presence or lack of islands in the Taylor state at a given location affect performance? If so, that would be a sign that the effects of boundary conditions on the ideal equilibria of Taylor states may be a guide to qualitatively predicting beahvior under full full time-dependent physics, potentially, if not counteracted by physics unaccounted for in the single-temperature Hall MHD model, all the way to reality.

If so, that could amount to a serious design concern for future SIHI devices, and potentially plasma devices of many types. If the effects of nonaxisymmetric magnetic boundary conditions are pronounced enough to disturb the magnetic topology of real plasmas as much as they disturb Taylor state equilibria, and this is to the detriment of the field configurations that these devices are seeking, that would amount to evidence for a mechanism by which symmetry in magnetically-relevant boundary conditions is of much more importance to plasma device design than hitherto recognized. If the result of features such as ports of vacuum vessels are sufficient to turn the field topology to which the plasma would prefer to relax into one with pronounced magnetic islands rather than one with smoothly-nested flux surfaces, and this tendency towards relaxation is significant, this could mean that device symmetry would be an important consideration in avoiding plasma instabilities.

However, that is not a conclusion that should be too readily assumed. First, *is* the tendency towards relaxation, or specifically of relaxation towards a field configuration that contains features as relatively-fine as the observed islands in Chap. 2, significant enough to affect the behavior of real devices, or does the dynamic injector action prevent the plasma from closely approaching the Taylor state? Second, if it is possible that effects homologous to the equilibrium islands can be seen in real plasmas, could they potentially be *good things*? Could a tendency that nature provides be, rather than struggled against, potentially harnessed? Philosophically, it should not be too readily assumed that it cannot: it has been observed multiple times in this study so far, with the tendency of plasmas to relax to the state of minimum energy with conserved helicity being used to provide a stable plasma configuration conducive to confinement in the spheromak, and the formidable energy contained within nuclei is itself danger on one side and power on the other. Additionally, targeted island inducement has been used for other configurations: resonant magnetic perturbations (RMPs) on tokamaks help avoid edge-localized modes, and island divertors in stellarators help control heat flux.

Answering either of those two concerns, in the general case, is beyond the scope of this exploration. Particularly the latter: the mechanism by which boundary-shape effects might be harnessed for particular use in real plasmas depends on the nature of those boundary-shape effects on *real* plasmas, and this work concerns computational comparisons only, on this front. Nevertheless, some avenues of potential promise can be seen already: it has been noted, as one of the foundational premises on which SIHI devices are proposed to work, that their inherent nonaxisymmetry is critical to their ability to drive current[22], as required by Cowling's Anti-Dynamo Theorem[23]; perhaps boundary effects could be of use in fine-tuning SIHI dynamos.

The concern about the tendency towards relaxation, or similar boundary-condition-induced effects, being observable on real plasmas is one that a step shall be taken toward addressing. But only one step: this research into computational plasmas is necessarily limited by the assumptions in its model and theoretical derivations from Hall MHD should not be considered validated discoveries of new plasma dynamics on their own. In the next section, the approach taken towards the search for boundary-shape effects in time-dependent, finite-pressure, Hall MHD simulations of SIHI devices only (the dynamics of plasmas in devices that do not seek to harness helicity conservation will not be considered here,) will be outlined, and a preliminary discussion of the limitations of the search will be provided, as well as the limitations of all potential routes that were available at this era in the simulation of SIHI spheromak plasmas.

4.2 Approach to the exploration of boundary effects in time-dependent MHD simulations

4.2.1 Limitations of this study

As comparing and contrasting the equilibria in differently-shaped volumes helped to highlight the impact of boundary features on equilibrium topology in Chap. 2, so too might comparing and contrasting the time-dependent performance of SIHI devices with different boundary features, using Hall MHD as in Chap. 3. To that end, two other SIHI experimental configurations (HIT-SI3 and HIT-SIU) have been simulated, with similar flux conservers in size and shape, and the same injector power, at the same perturbation-cycling frequencies, as HIT-SI was in Chap. 3, and the results of those simulations are to be compared here to each other and to the single-temperature Hall MHD frequency scan of HIT-SI.

However, before those simulations are described further, in the interests of contextualizing the limits of this approach, those limits shall be described first. Two primary questions about

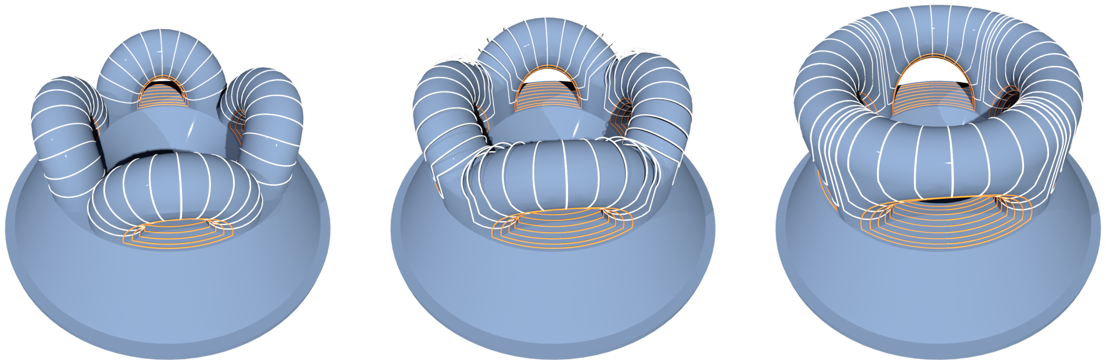

(a) Four discrete injectors (b) Intermediate (c) Four-mouthed manifold

Figure 4.1: Demonstration of the topological equivalence between a SIHI device with N discrete mug-handle injectors and a SIHI device with an N-mouthed manifold, including an intermediate state in the topologically-constant transformation.

the utility of this approach in uncovering true boundary-geometry-dependent effects on the behavior of these simulated devices must be kept in mind:

The first utility question is whether these simulations amount to an adequate isolation of boundary-geometry effects, or if other differences between the devices are more salient. The differences that could be more salient include the fact that the helicity injectors, for these three devices, are not only different in placement but different in number: HIT-SI has two injectors with four mouths; HIT-SI3 has three injectors with six mouths, and HIT-SIU has four injectors with four mouths, connected to a manifold. Topologically, there is no difference between the boundary shapes of HIT-SIU and a hypothetical "HIT-SI4" with four discrete HIT-SI3-type injectors; a manifold can be constructed by "pushing out" on the border region between the discrete injector mouths, as shown in Fig. 4.1.

However, while a manifold is *topologically* equivalent to a device with as many mug-handle injectors as the manifold has mouths, it is not necessarily *functionally* equivalent: geometric features that do not change the topology can nevertheless strongly affect the simulated plasma dynamics: for example, in HIT-SI3 (or “HIT-SI4”,) a current path that runs through multiple injectors must pass through the main flux conserver volume on its route from injector to injector; in HIT-SIU or other manifold configurations, it is possible for current to flow from injector to injector without touching the spheromak confinement volume.

Whether that is a good or bad influence on device performance depends on which side of a trade-off matters more: on one side, there exists the possibility for the injectors to drive current entirely within themselves that does not affect the spheromak, and this could potentially degrade the observed current gain; on the other side, the reduction of “noise” resulting from this effect (without multiple injector mouths blasting into the spheromak confinement volume in close proximity yet pronouncedly out-of-phase with each other) could potentially result in a cleaner perturbation on the spheromak, and perhaps that could counterbalance the loss in current gain, or alternatively produce benefits in confinement quality instead.

Either way, the mere fact that one of these device configurations uses a manifold injector while the others do not adds an additional variable on simulated device performance that will cloud the extraction of boundary-shape influences on time-dependent plasma behavior in this scan.

That HIT-SIU has a manifold while the others do not is not the only difference: HIT-SI3 and HIT-SIU both have their injector mouths located on the same side of the main flux conserver; HIT-SI’s two pairs of injector mouths are located on opposite sides. This means that there is not only a toroidal variation in the boundary perturbations that are injector mouths, but also a poloidal variation, further clouding the correlation between boundary shapes and time-dependent plasma dynamics.

A further and related point is that the magnetic boundary conditions (of injector action) also differ between devices: as they have different numbers of injectors, the imposed perturbation spectrum is necessarily going to differ between devices. While the overall construction of the simulations used for comparison here targets an injector-imposed perturbation in the form of an n=1 mode rotating counterclockwise around the plasma volume at a frequency of f_{inj}, whether that is the proper comparison versus another shared condition (for example, all the injectors firing in-phase for all devices) remains questionable, but it is a plausible baseline for comparison, and is useful as a planned target for future experiments.

However, while these devices may not be the optimal set for a direct comparison of geometric effects on plasma dynamics, they *do* share one valuable condition: all three geometries correspond to experimental devices that either have (HIT-SI,) do (HIT-SI3,) or will (HIT-SIU) exist, meaning that these frequency scans are of use on their own for comparisons with experimental data in ways that would not be as practical if a set of hypothetical devices were invented for a boundary-effects scan alone. Unlike in Chap. 3, however, the three devices will be compared only to each other rather than further experimental validation being presented here.

The second utility question about the value of such an exploration is whether boundary effects are extricable at all from simulations of SIHI plasmas in the experimentally-achieved performance regime in ways that would be relevant to higher-performing regimes. If the current gain is too low, and the plasma dynamics are dominated throughout the entire volume by direct injector action, then the effects of boundary shapes are likely too fine to discern through the relative strength of the injectors, even if the boundary-effect shapes would potentially dominate over injector action in defining the equilibrium topology for a high-gain spheromak.

It is also notable that a SIHI plasma is not ever exactly in a static equilibrium of the same sort as the Taylor states explored in Chap. 2; there is a dynamic, though steadily periodic and ideally smooth, influence from injector action maintaining the dynamo. The resulting equilibrium that the plasma seeks when being dynamically stirred by the injectors could be qualitatively different from the static Taylor state equilibrium, particularly in the range where a spheromak has formed yet current gain is still relatively low. At the limit of infinite current gain, however, the effects of injector action should approach zero.

However, the matter of pressure confinement, which would ideally exist at high current gains, provides yet another difference between the ideal Taylor state cases and what would be observed in reality. Further effects such as nonzero dissipation are likely to also alter the target equilibrium's topology, with the total result that the influences of boundary features in themselves on plasma dynamics may be difficult to identify, particularly if the boundary features are not sufficiently global to dominate the nested-flux-surfaces spheromak entirely, as while those cases would be easier to read, they would also be unlikely to produce high-current-gain, pressure-confining plasmas.

Nonetheless, it is the low-current-gain regime that is of concern here: experimentally, injector current has always been tens of percent of the spheromak current, and the simulations presented here do not produce spheromaks with current gains better than has been experimentally observed. As such, the possibility that direct injector action may swamp any observed boundary-feature influence is a probability. Even so, the comparisons of these experimental geometries under matched conditions may still illuminate the influence of different design decisions in broad strokes.

4.2.2 Conditions of the three-device frequency scan

The two additional devices being simulated for the purposes of geometric comparison are HIT-SI3 and HIT-SIU, the geometries for both of which were shown in Fig. 2.13 (As the final, zero-injector, version from that figure cannot be driven, it is excluded from this scan,) and the same parameters used for HIT-SI and given in Sec. 3.1.2 are applied where possible. That is, all but the first two rows in Table 3.1 apply to the HIT-SI3 and HIT-SIU frequency scan simulations; also, the same four injector frequencies of 14.5, 36.8, 53.5, and 68.5 kHz were used for all three devices.

What is not held constant is the injector conditions. For the purpose of targeting the same plasma conditions, the injector flux and voltage were not held constant per injector across devices, as that would result in an increasing power flux with increasing number of injectors, necessarily heating the plasma more and enabling greater current gains due to the lowered resistivity. Instead, to maintain the same ratio of injector flux to current as HIT-SI, the injector flux and voltage were both scaled by a factor SF for the case with N injectors:

$$SF = \sqrt{\frac{2}{N}} \tag{4.1}$$

such that

$$\sum_{i=1,N} (SF)^2 = 2 \quad \forall N \in \mathbb{Z}+ \tag{4.2}$$

and thus power injection, presumed from NIMROD simulations to be proportional to the sum in Eq.4.2, remains theoretically constant.

Also of interest is the injector phasing: while the HIT-SI injectors were fired ninety degrees out of phase in order to produce Steady Inductive Helicity Injection (due to the orthogonality of the waveforms at that phasing,) HIT-SI3 and HIT-SIU both have more injectors, and an equivalent phasing for each was chosen so as to produce, as much as is possible, an $n = 1$ imposed perturbation rotating counterclockwise (when viewed from above) in the volume at the injector frequency; that is, the three HIT-SI3 injectors were simulated as running 120° out-of-phase sequentially in this counterclockwise order and the four HIT-SIU injectors were simulated as running 90° out-of-phase in the same counterclockwise order.

This results in the injector parameters for each case given in Table 4.1.

Table 4.1: Injector parameters for three simulated devices

Parameter (Symbol, Units)	HIT-SI	HIT-SI3	HIT-SIU
Injector flux (ψ, mWb)	0.500	0.408	0.354
Injector current (I, kA)	8.000	6.532	5.657
Injector phasing (ϕ, °)	$0 - 90$	$0 - 120 - 240$	$0 - 90 - 180 - 270$

As in Chap. 3, the injector frequency cases will be referred to by their truncations to the nearest whole kHz (14, 36, 53, and 68 kHz).

Under those conditions, for all four injector frequencies, all three devices were simulated for a full simulated millisecond; the results of the three-device frequency scan are given in the following section.

On all curve plots in this chapter where the three devices are compared, HIT-SI's results will be shown in blue, HIT-SI3's results in green, and HIT-SIU's results in red.

4.3 The Three-Device Frequency Scan

4.3.1 Current Gain

As the three geometries in question are all those of plasma current drive experimental device designs, the most immediately salient metric for the overall performance of these devices is the total current gain achieved.

Note the definition of current gain: it is the total toroidal current I_tor divided by the root-sum-square of the current in each injector:

$$CG = \frac{I_{tor}}{\sqrt{\sum_{i=1,N} I_{inj,i}^2}} \tag{4.3}$$

The amplitude of the current waveform for each injector is the same, set so the denominator in Eq. 4.3 is 8 kA, and is held constant through the simulation after an initial ramp from zero over the first 50 μs. The current gain values displayed in Fig. 4.2 therefore are defined identically for all devices, and as the values given are at the end of the simulated millisecond, they also correspond directly to toroidal current divided by 8 kA.

It can be seen that current gain rises with injector frequency for all devices except, at the upper range of the frequency domain, HIT-SIU, which alone among the three sees a decrease in current gain at $f_{inj} = 68$ kHz compared to $f_{inj} = 53$ kHz. This immediately marks that case as being the most obvious for investigation, but other trends visible in Fig. 4.2 also deserve mention:

HIT-SI's current gain increases the fastest with increasing frequency of the three: HIT-SI3 sees higher current gains than HIT-SI at lower frequencies but not at higher frequencies. HIT-SIU sees lower current gains than its sister devices at all frequencies, with its trendline's

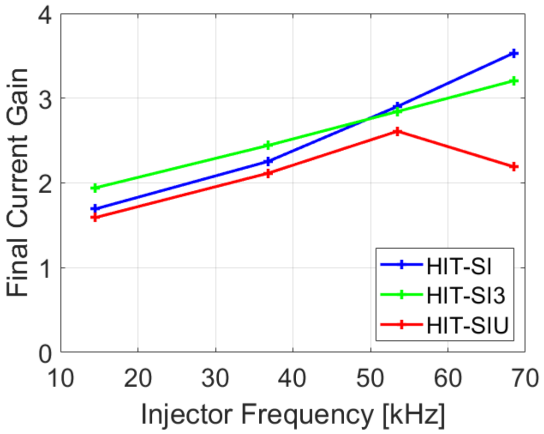

Figure 4.2: Cycle-averaged current gain at the end of the 1 ms simulated shots for PSI-Tet simulations of HIT-SI (blue), HIT-SI3 (green), and HIT-SIU (red).

slope initially tracking between the slopes of the other two (seeing an increase from 36 to 53 kHz over 14 to 36 kHz that is greater than HIT-SI3's but less than HIT-SI's) until the slope reverses between 53 kHz and 68 kHz.

To explore the dynamics further, plots of current gain versus time are given for all four frequencies and all three devices in Fig. 4.3.

Here the difference in current-drive dynamics between devices becomes apparent: a general trend can be observed that HIT-SI3 reaches higher current gains first (is faster to start up) compared to the other two, but its overall ability to build up current with time after that lags behind HIT-SI's.

HIT-SI sees faster-increasing current gain with time for the duration of the simulated millisecond for all four frequencies than the other two devices do, though HIT-SIU's performance closely follows HIT-SI's at 36 kHz.

HIT-SIU is also noteworthy for having the flattest plateaus in current gain, particularly for the 14 kHz and 36 kHz cases; the 14 kHz case is very flat and sees no change in the last forty percent of the simulated millisecond; the case of 68 kHz, where HIT-SIU sees much lower current gains than the other two devices do, is also not necessarily due to starting

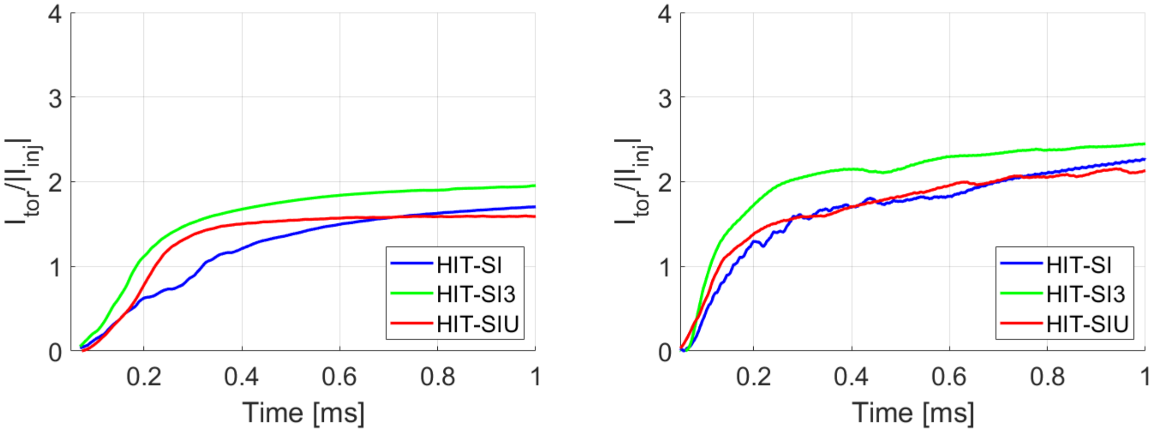

(a) $f_{inj} = 14$ kHz (b) $f_{inj} = 36$ kHz

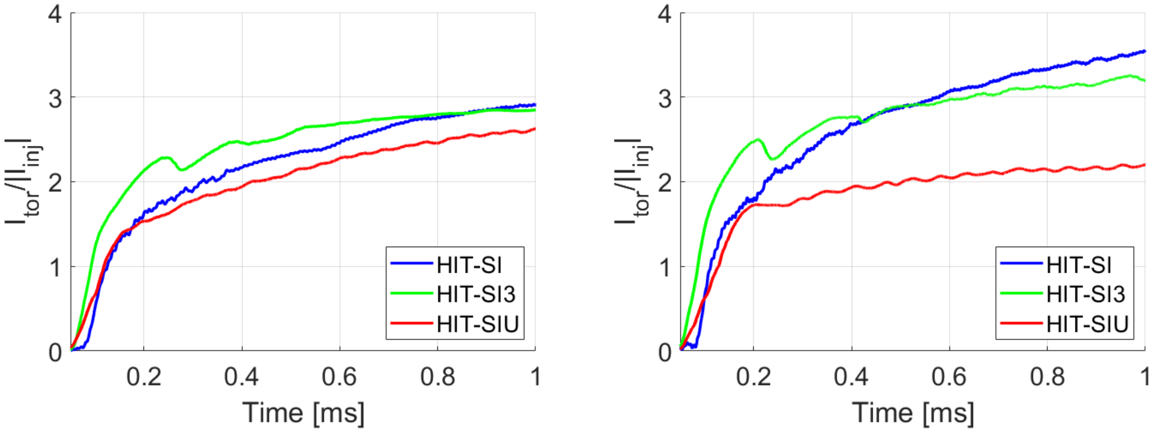

(c) $f_{inj} = 53$ kHz (d) $f_{inj} = 68$ kHz

Figure 4.3: Plots of current gain versus time for each device: HIT-SI (blue), HIT-SI3 (green), and HIT-SIU (red).

up at lower gains than the other two devices (although the shape of the HIT-SIU 68 kHz current gain curve closely tracks the HIT-SI3 68 kHz current gain curve if scaled by a factor of approximately two-thirds, it also tracks the HIT-SI curve closely until 0.2 ms) but instead due to the post-startup throttling up of current gain being significantly less than the other two, in absolute terms.

Overall, it appears that, at $f_{inj} = 68$ kHz, HIT-SIU sees HIT-SI-like startup and HIT-SI3-like sustainment. The strengths of both preceding devices are in the opposite phases of their shots, so that does not bode well for the operation of HIT-SIU at 68 kHz, but current plans for the experimental HIT-SIU do not extend to operating it at such a frequency anyway.

4.3.2 Surface Probe Comparisons (Current Centroid Behavior)

In Sec. 3.3.3, it was found that PSI-Tet (and NIMROD) single-temperature simulations of HIT-SI did not observe the experimentally-observed changes in current centroid behavior: an outward radial shift in average current centroid position, and a reduction in the standard deviation of the measured current centroid radial position, with increasing f_{inj} indicating that the structure of the spheromak shifted to the outboard and became more symmetric on experimental HIT-SI.

Instead, PSI-Tet-simulated HIT-SI was observed to have considerably *greater* current centroid radial position standard deviation and a more-inboard mean radial position than experiment at all frequencies, and no significant net change was observed in mean position with injector frequency.

To explore whether those trends persist for PSI-Tet simulations of the other two devices, Figure 4.4 shows traces of the current centroid radial positions mean and standard deviations versus time for all three devices, enabling direct comparisons across geometries of this aspect of the simulated plasma behavior.

Fig. 4.4 shows that, for all three devices, there is no significant outward shift in current centroid radial position between 14 kHz and 68 kHz. The ordering of which device has the most-outward mean current centroid position shifts from frequency to frequency, with the

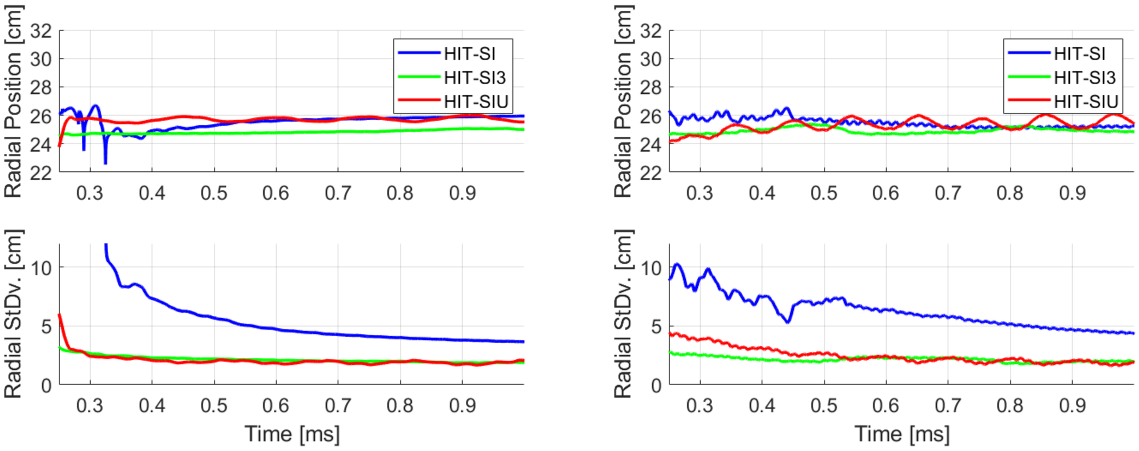

(a) $f_{inj} = 14$ kHz (b) $f_{inj} = 36$ kHz

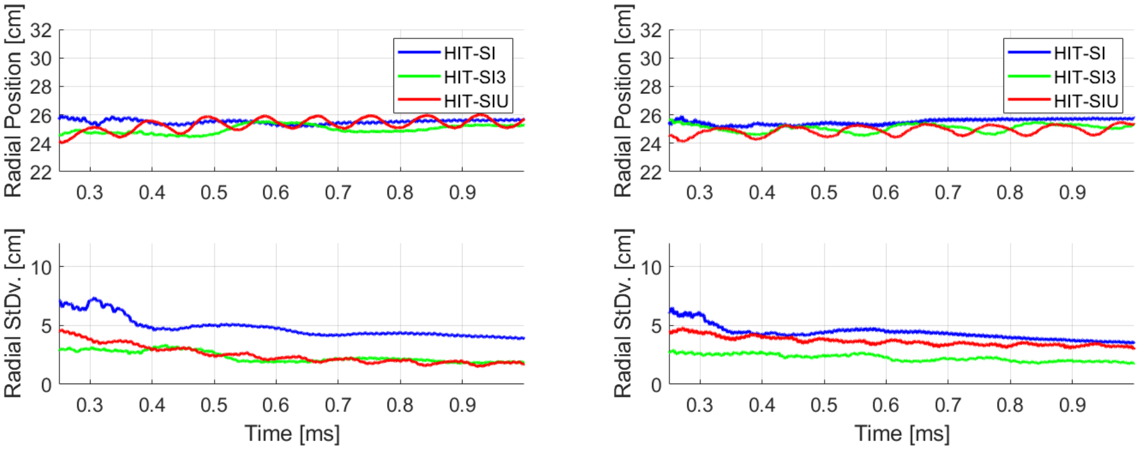

(c) $f_{inj} = 53$ kHz (d) $f_{inj} = 68$ kHz

Figure 4.4: Plots of current centroid mean radial position (upper half of each quadrant) and the standard deviation (lower half of each quadrant) thereof for each device: HIT-SI (blue), HIT-SI3 (green), and HIT-SIU (red), for each frequency, as in Fig. 3.12.

relation that is closest to constant being that HIT-SI3's mean radial position tends to be inward from HIT-SI's.

HIT-SIU, however, sees an *inward* shift in mean radial position at 68 kHz, relative to the other three frequencies.

Simultaneously, it sees an increase in current centroid radial standard deviation, which goes from closely tracking HIT-SI3's standard deviation curve at the three lower frequencies to being always greater than HIT-SI3's standard deviation at 68 kHz. HIT-SI's standard deviation curve remains greater than the other two devices' curves across all four frequencies; the markedly high standard deviation observed in the PSI-Tet simulations Chap. 3 does appear to be a feature more pronounced in HIT-SI than in either of the other two devices.

Another feature of note is the low-frequency activity observed in the mean radial position curves for HIT-SIU. There is a radial oscillation visible with a frequency that varies from approximately 6 kHz for the $f_{inj} = 14$ kHz case to approximately 14 kHz for the $f_{inj} = 53$ kHz case, and it clearly is not monotonically increasing with injector frequency, because the frequency of the oscillation decreases as f_{inj} increases from 53 kHz to 68 kHz, reversing the trend seen at lower frequencies, dropping from about $f_{osc} = 14kHz$ to $f_{osc} = 10$ kHz with the final upward step in injector frequency. Again the change in trend trajectory happens at the same place in the frequency scan as did the change in current gain.

Overall, the three devices see similar dynamics in their current centroid behavior to each other, and none display the outward shift and symmetrization experimentally observed on HIT-SI. HIT-SIU's behavior reveals a low-frequency oscillation and a change in dynamics from $f_{inj} = 53$ kHz to $f_{inj} = 68$ kHz, in common with other parameters for that simulated device.

4.3.3 Internal Magnetic Probe Comparisons

In Chap. 3, it was shown that internal magnetic probe behavior correlated with current centroid behavior for the different datasets, with an outward shift in mean current centroid radial position being observed to correlate with an outward shift in the zero-crossing of the

z-component of the magnetic field as measured by the internal magnetic probe.

The same analysis as in Sec. 3.3.2 has been performed on these three devices' simulated frequency scans, with the internal magnetic probe signals being cycle-averaged over the final five injector cycles (three for the 14 kHz cases) and normalized by the toroidal current; the results are plotted in Figure 4.5, grouped by injector frequency to compate the performance of different devices.

The shapes of the field profiles appear to be somewhat consistent per device across frequencies, relative to each other. HIT-SI's zero-crossing is by far the most inboard; while HIT-SI3's zero-crossing is generally the most outboard. HIT-SI3 also sees a higher, sharper peak towards the outboard in contrast to the lower and smoother profiles seen by both HIT-SI and HIT-SIU. The multiple switches between positive and negative curvature for HIT-SI3 are also not seen in the other two devices.

The relative order of the zero-crossings of the z-component of the magnetic field does not appear to correlate with the relative order of the current centroid mean radial positions seen in Sec. 4.3.2; however, it may correlate with the relative order of the standard deviations seen towards the end of the simulated milliseconds, with HIT-SI having a distinctly greater standard deviation in the radial position of its current centroid, as well as a much further-inboard zero-crossing at all frequencies. HIT-SI3 and HIT-SIU, by contrast, see lower standard deviations and more-outboard zero-crossings, and their curves are generally closer to each other than either is to HIT-SI.

Overall, the dynamics seen in these studies of internal magnetic probe profiles point to effects more complicated than these normalized-and-cycle-averaged metrics can effectively diagnose; while it may not be enough to reveal a full working theory of the plasma dynamics, more spatially-varying measures, as will be looked at in the next section, may also be of use.

4.3.4 Temperature Dynamics

All simulations of this three-device frequency scan were performed using the single-temperature Hall MHD model in PSI-Tet; while this lacks separate ion and electron temperature dynam-

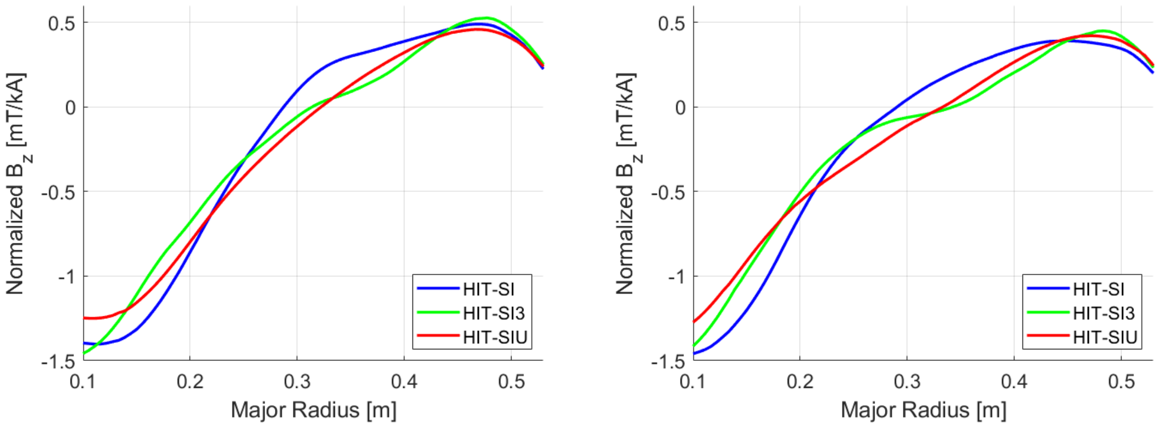

(a) $f_{inj} = 14$ kHz

(b) $f_{inj} = 36$ kHz

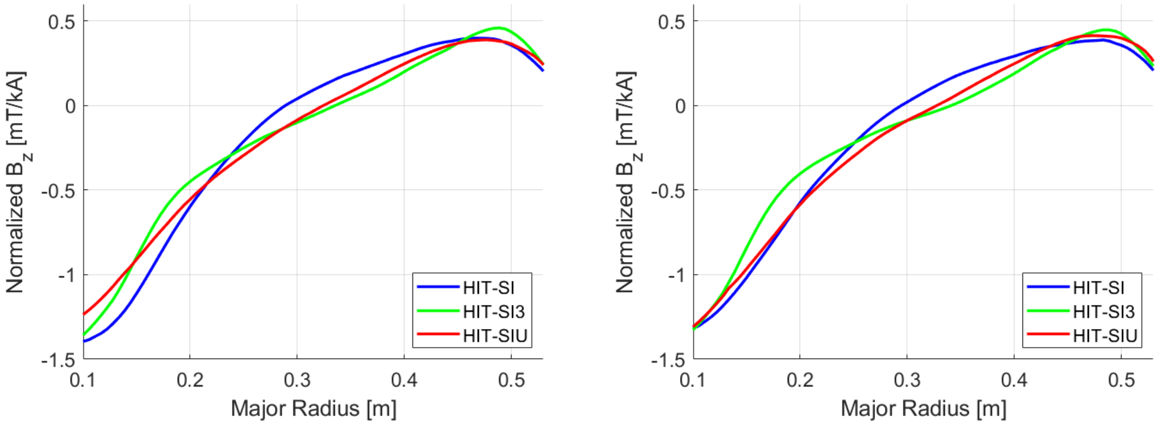

(c) $f_{inj} = 53$ kHz

(d) $f_{inj} = 68$ kHz

Figure 4.5: Plots of normalized mean internal magnetic field profiles at the end of the shot versus probe radial position for each device: HIT-SI (blue), HIT-SI3 (green), and HIT-SIU (red), for each frequency, as in Fig. 3.11.

ics, that may be of use in approaching experimental behavior in simulations (See Sec. 3.4,) the fact that the same model is being used for all cases here still allows for some comparisons that are more direct than the ones included in Chapter 3.

To begin, the equivalent comparisons as shown in Fig. 3.1 are shown in Fig. 4.6, giving the average (solid lines) and maximum (dashed lines) temperatures for all three devices for each of the four injector frequency cases.

The relative placement of the three devices' temperatures (both their averages and their maxima) is consistent across the four injector frequencies: the temperature curves for HIT-SI and HIT-SI3 track each other closely, while the temperature curves for HIT-SIU are always below their equivalents for the other two devices.

Almost entirely: if not for one moment around 0.2 ms in the 14 kHz case where the average temperature for HIT-SIU briefly rises above the average temperature for HIT-SI, the average and maximum temperatures for HIT-SIU would be strictly below those of the other two devices' at all times after the initial conditions. Regardless, the trend is clearly strong, and indicative that HIT-SIU is either receiving or confining energy less effectively than the other two devices are.

Recall that the injector voltage and flux were set specifically to keep the total power injection into the plasma constant across devices (at given injector frequencies.) However, as power input is not defined explicitly for these simulations, it cannot be said for sure that these measures succeeded. If they did succeed, then perhaps thermal confinement is responsible for the difference.

But the temperature dynamics studied in single-temperature PSI-Tet before (Sec. 3.2.1) do not suggest that proper closed-field-line energy confinement of the category needed for scaling to fusion conditions is yet significantly captured in these simulations of SIHI devices at this scale; it is likely that significant parallel (i.e., unconfined) thermal conduction is playing a role in setting the peak temperature.

Specifically, the more complex manifold structure of HIT-SIU compared to the half-tori injectors of HIT-SI and HIT-SI3 may allow the heat injected in the plasma to dwell in the

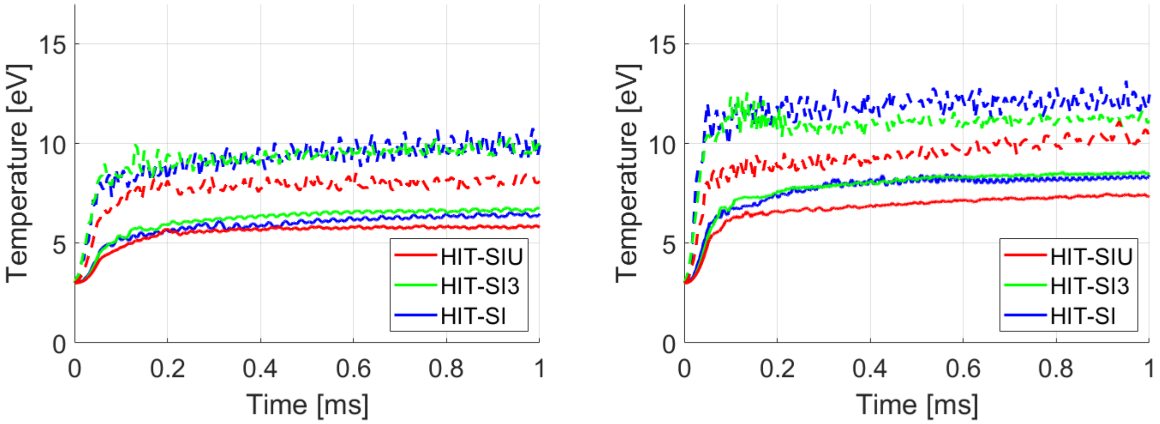

(a) $f_{inj} = 14$ kHz (b) $f_{inj} = 36$ kHz

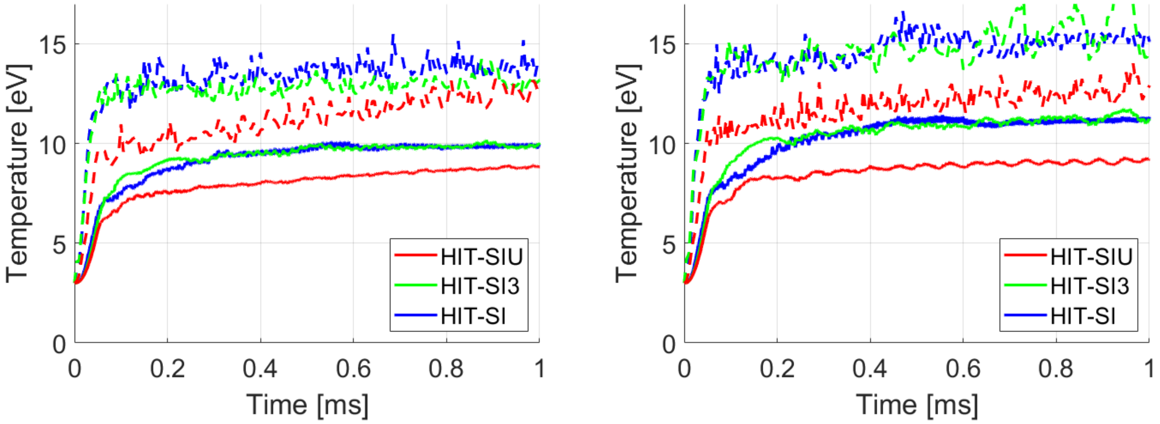

(c) $f_{inj} = 53$ kHz (d) $f_{inj} = 68$ kHz

Figure 4.6: Plots of average (solid lines) and maximum (dashed lines) plasma temperature versus time for each device: HIT-SI (blue), HIT-SI3 (green), and HIT-SIU (red), for each frequency, as in Fig. 3.1.

injector regions for more time, and since the injectors have smaller characteristic length scales, and thus shorter average distance to the wall, than the main volumes do, this may produce by greater wall losses in the injector manifold compared to the losses in the half-tori injectors of the other two devices. As the injectors have also been found in practice to be significant risk sites for damage due to experimental operation, the possibility that injector manifolds could potentially see greater heating due to operation is an operational consideration that deserves awareness.

Potentially this is the source of the lower current gain of HIT-SIU compared to the other two devices: if it is less efficient at heating the plasma, it will have to drive current in colder and more-resistive plasma.

Simulations of the entire plasma volume mean that these questions do not need to be speculated upon based on line plots alone; Figures 4.7 through 4.9 show pseudocolor plots of the plasma temperature for all three devices (Fig. 4.7 for HIT-SI; Fig. 4.8 for HIT-SI3, and Fig. 4.9 for HIT-SIU) at all three frequencies, according to a constant color scale, with the slices taken at equivalent times in the shots: near the end of the simulated millisecond, at the same phase in the cycle, visible by the presence of a filament of high-temperature plasma wrapping around the outboard side of the positive-X side of the plasma from the positive-X-most injector.

Various features of temperature dynamics present themselves: Fig. 4.7 shows a steady progression of peak temperature from $f_{inj} = 14$ kHz to $f_{inj} = 68$ kHz, until the peak temperatures within the main flux conserver begin to exceed the peak temperatures within the injectors at the highest injector frequency.

Fig. 4.8 shows a similar trend for HIT-SI3, including a hint of temperatures in the main flux conserver volume exceeding those in the injectors at the highest injector frequency. (The yellow patches in the main volume in Fig. 4.8d may not be as distinct as the patches in Fig. 4.7d, but they are discernible.)

Fig. 4.9 does not show such a pattern; as seen with the overall trends in current gain and average or peak temperatures, the $f_{inj} = 68$ kHz case does not see significant improvement

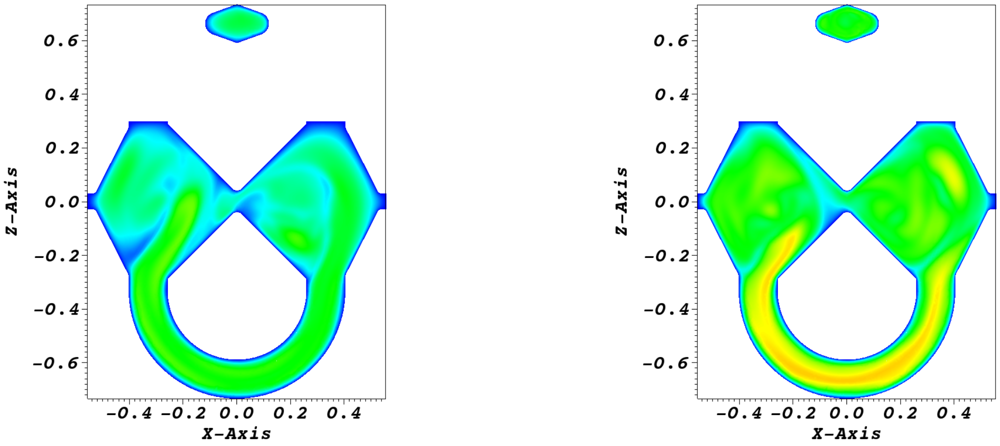

(a) $f_{inj} = 14$ kHz

(b) $f_{inj} = 36$ kHz

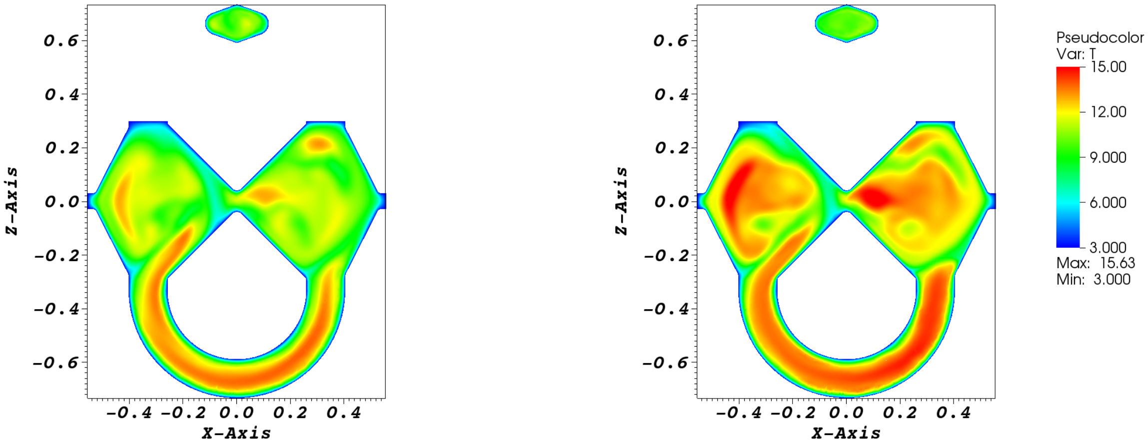

(c) $f_{inj} = 53$ kHz

(d) $f_{inj} = 68$ kHz

Figure 4.7: Temperature slice plots at the same phase in the injector cycle at approximately 1 ms into each frequency's simulation for HIT-SI, as in Fig. 3.3.

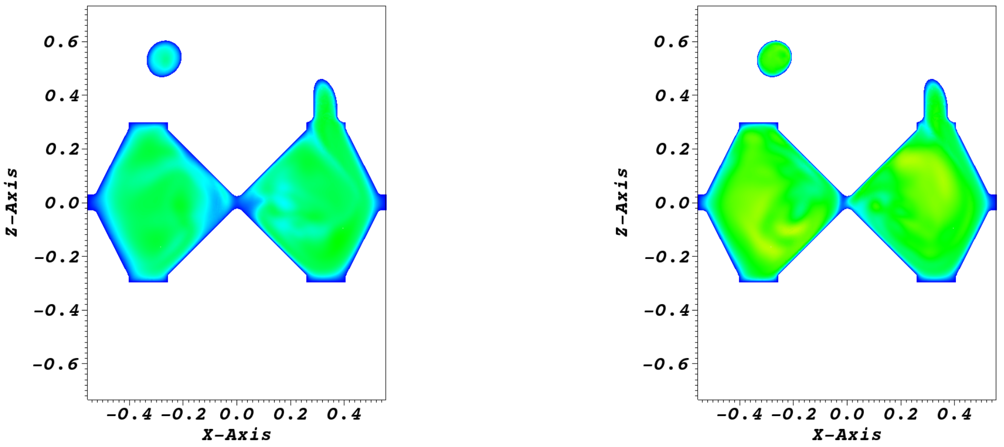

(a) $f_{inj} = 14$ kHz

(b) $f_{inj} = 36$ kHz

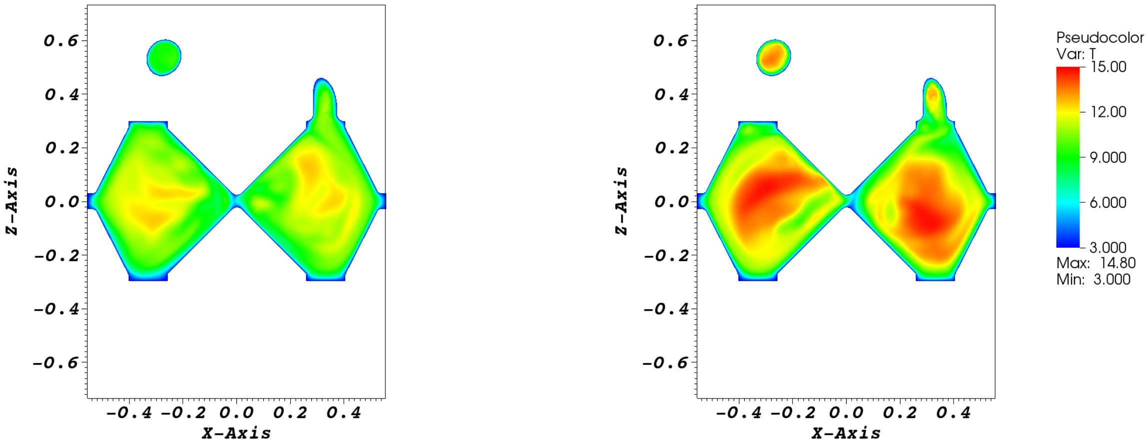

(c) $f_{inj} = 53$ kHz

(d) $f_{inj} = 68$ kHz

Figure 4.8: Temperature slice plots at the same phase in the injector cycle at approximately 1 ms into each frequency's simulation for HIT-SI3.

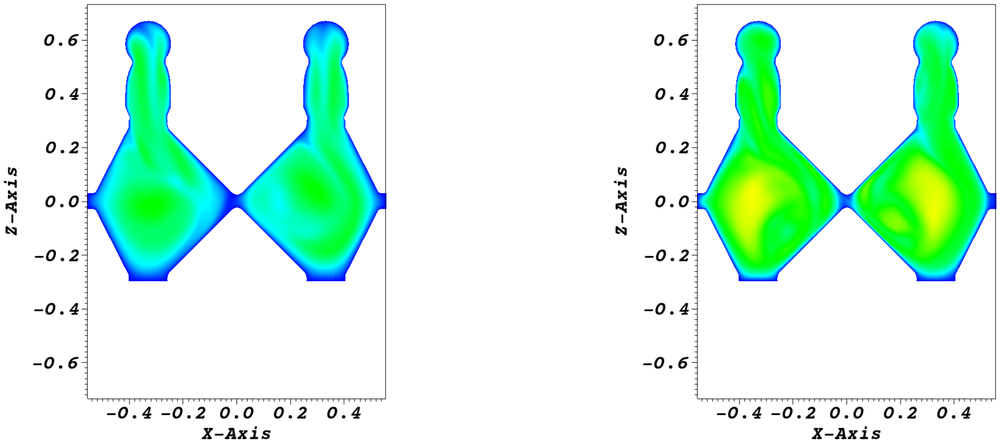

(a) $f_{inj} = 14$ kHz

(b) $f_{inj} = 36$ kHz

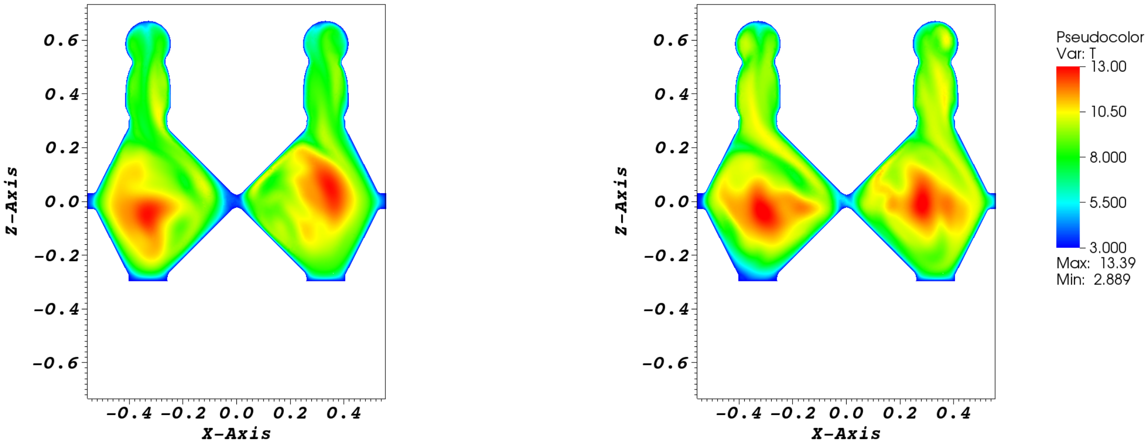

(c) $f_{inj} = 53$ kHz

(d) $f_{inj} = 68$ kHz

Figure 4.9: Temperature slice plots at the same phase in the injector cycle at approximately 1 ms into each frequency's simulation for HIT-SIU. Note the maximum temperature on the color scale is here 13 eV compared to the 15 eV of the previous two cases.

over the $f_{inj} = 53$ kHz case. It does not appear to be the case that temperatures observed within the manifold are necessarily *higher* than temperatures within the main flux conserver, but they do not appear to be *lower*.

Furthermore, an additional feature is visible within the complex geometry of the injector manifolds of HIT-SIU in Fig. 4.9: where the other two devices see singular filaments of high-temperature plasma per injector, HIT-SIU tends to see multiple parallel filaments, visible in all cases but particularly in the +X injector in Fig. 4.9a, and even in the +X injector in Fig. 4.9d. It appears there is sufficient volume and geometric freedom within the injector manifold of HIT-SIU for plasma dynamics to develop that are more complicated than the dynamics in the injectors of HIT-SI and HIT-SI3; it is likely that the injector action is less effective at producing a high-performing plasma in the main flux conserver in this geometry because more of that action must be diverted to driving the in-manifold plasma dynamics.

4.3.5 Density Dynamics

Plasma density dynamics can also be compared across frequencies and devices for these finite-temperature simulations; the synthetic interferometer analysis performed in Sec. 3.2.2, according to the synthetic probe line placed as shown in Fig. 3.7 for all three simulated devices.

All three devices shown an overall trend towards slightly lower final average densities with increasing frequencies, but all three devices have their own quirks: HIT-SI3 sees the lowest initial density spikes and the highest final densities, seeing an overall flatter trajectory than either other device does. HIT-SI, unlike the other two, does not tend to see low-frequency activity in its density dynamics, that are particularly pronounced for the other two, and see some regular periodic shapes in HIT-SIU: see the HIT-SIU curve in Fig. 4.10a, where from approximately 0.55 to 0.85 ms, the density oscillates in a distinct triangle-wave; in Fig. 4.10d, from about 0.25 ms onward, there is nearly a square wave with a period of approximately 10 kHz. While the shapes of the oscillations are too likely to be random for much of interest to be read into them, their frequencies correspond to the low-frequency oscillations observed

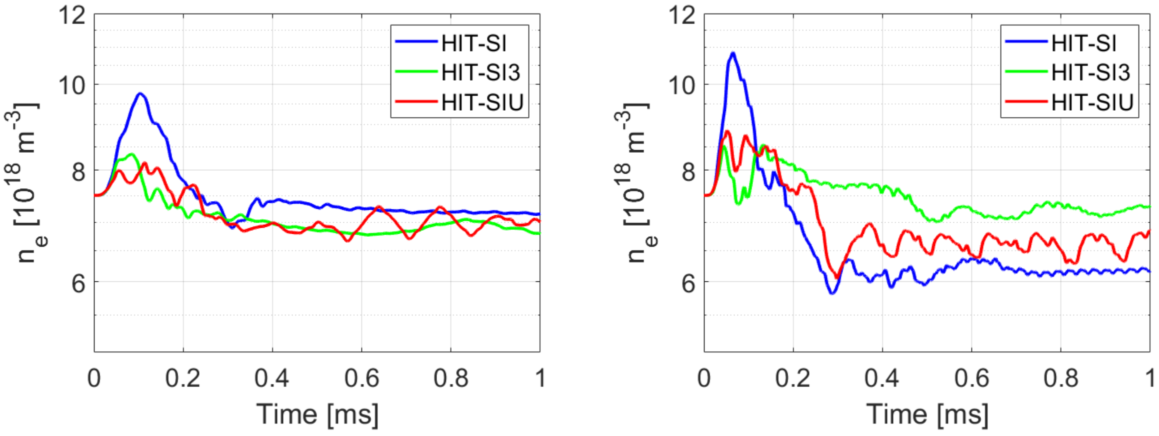

(a) $f_{inj} = 14$ kHz

(b) $f_{inj} = 36$ kHz

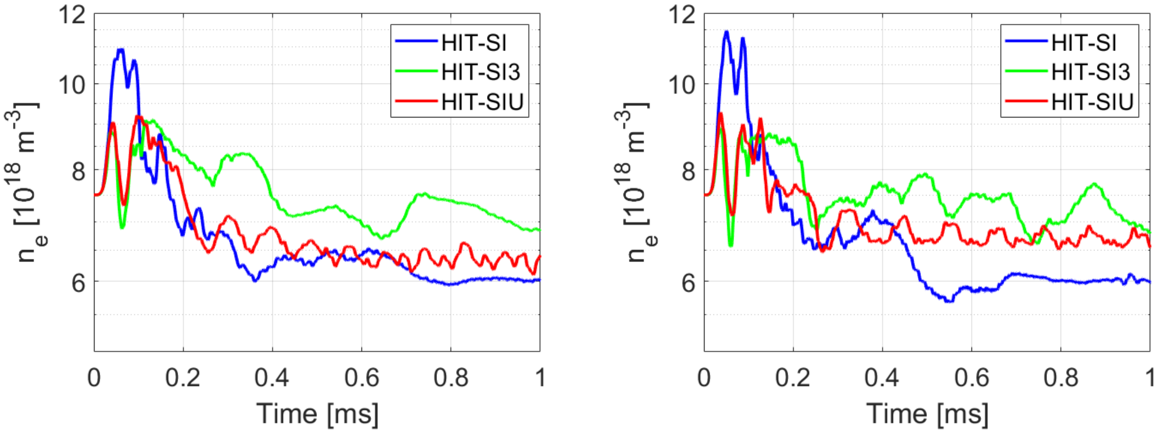

(c) $f_{inj} = 53$ kHz

(d) $f_{inj} = 68$ kHz

Figure 4.10: Plots of synthetic interferometer-measured density versus time for each device: HIT-SI (blue), HIT-SI3 (green), and HIT-SIU (red), cycle-averaged at the injector frequency for such frequency, as in Fig. 3.4.

in the current centroid behavior in Sec. 4.3.2; the low-frequency oscillations observed in HIT-SIU in particular show their signature in multiple places.

4.3.6 Magnetic Field Modal Analysis

Considering the effects observed in Chap. 2 whereby Taylor state equilibria formed islands in a manner to perform a Fourier-like decomposition of their boundary shape, if such an effect is to be visible in these time-dependent MHD simulations, it would most likely be apparent in the modal analysis performed as in Sec. 3.3.4.

For example, HIT-SI's $n = 2$ symmetry, HIT-SI3's $n = 3$, and HIT-SIU's $n = 4$ could all potentially make themselves visible in relatively-stronger components of the corresponding toroidal modes.

Any such search would be subject to many caveats, however: primarily, there are many features in the overall simulated shot that could contribute to mode amplitudes in unexpected ways: injector action could couple to the plasma and excite modes that do not correspond to injector symmetry; even the equilibria explored in Chap. 2 often saw their boundary decompositions produced in surprising ways: notably, as seen in Figs. 2.14 and 2.15, all of HIT-SI, HIT-SI3, and HIT-SIU saw significant $q = 1/2$ islands whether their foremost symmetry was $n = 2$ or not; $q = 1/2$ islands, every one of which is innately $m = 1,\ n = 2$ in shape, can double up on the same flux surface to produce (for the case of HIT-SIU) an $m = 2,\ n = 4$ perturbation, or (for the case of HIT-SI3) an $m = 3,\ n = 6$.

Similarly, the BD mode subtraction performed may conflate the effects of injector *action* and (passive) injector *presence*, though it is likely that the latter is accounted for in the overall equilibrium-associated first BD mode.

In light of that, the influence of injector presence on the equilibrium would be discernible by observing whether the modes with n-number corresponding to their device's symmetry significantly decrease in amplitude (ideally more than others) between the second and third rows of each of the subfigures in the following set of BD mode subtraction figures by frequency for each device: Fig. 4.11 for HIT-SI, Fig. 4.12 for HIT-SI3, and Fig. 4.13 for HIT-SIU. If that is so, then the first BD mode, correlated with the spheromak, contains Fourier modes significantly correlated with the boundary shapes, and boundary effects like those observable in Taylor states in Chap. 2 are present in these time-dependent Hall MHD simulations.

For the three devices in total, it does not appear that there is a consistent trend towards the mode number associated with the device's symmetry being reduced in the spectrum that remains once the equilibrium is subtracted out. This would be identified by a significant decrease between the subfigures' second and third rows in $n = 2$ for HIT-SI in Fig. 4.11, in $n = 3$ for HIT-SI3 in Fig. 4.12, or in $n = 4$ for HIT-SIU in Fig. 4.13.

A case of the mode persisting is visible with $n = 2$ in the HIT-SI cases; for almost all times after startup for all frequencies, the (dark green) $n = 2$ amplitude after the injector- and equilibrium-correlated BD modes have been subtracted out remains greater than all other amplitudes, with only a few moments where $n = 4$ challenges it for dominance.

However, the other two devices do see decreases in their associated modes. The $n = 3$ curve (bright green) *does* see a significant decrease between the final two rows of all the frequency subfigures in Fig. 4.12; the $n = 2$ persistence appears to be a common trait of that mode across devices and frequencies. Similarly, the $n = 4$ curve (purple) for HIT-SIU in Fig. 4.13 sees a reliable reduction in amplitude at all frequencies, though it is never at a particularly large amplitude compared to the modes with lower numbers to begin with.

Altogether, there exist too many confounders to declare any sort of conclusion along the lines of "boundary effects on the equilibrium exist in HIT-SI3 and HIT-SIU but not HIT-SI;" the data presented here does not have sufficient signal relative to its noise to discern definite boundary effects on equilibria that affect time-dependent plasma performance. Nonetheless, this scan has provided some evidence, even if it is unclear, that there is some mode impact on the equilibrium from the boundary shape that is visible in the full dynamics. Potentially further studies could be performed using geometries and diagnostics optimized for this search: for example, the modal analysis could be increased in precision by the use of more synthetic probes: as these are simulated devices, there is ultimately no need to restrict the analysis to probes in the same locations as experimental probes, nor even to the surface of the plasma

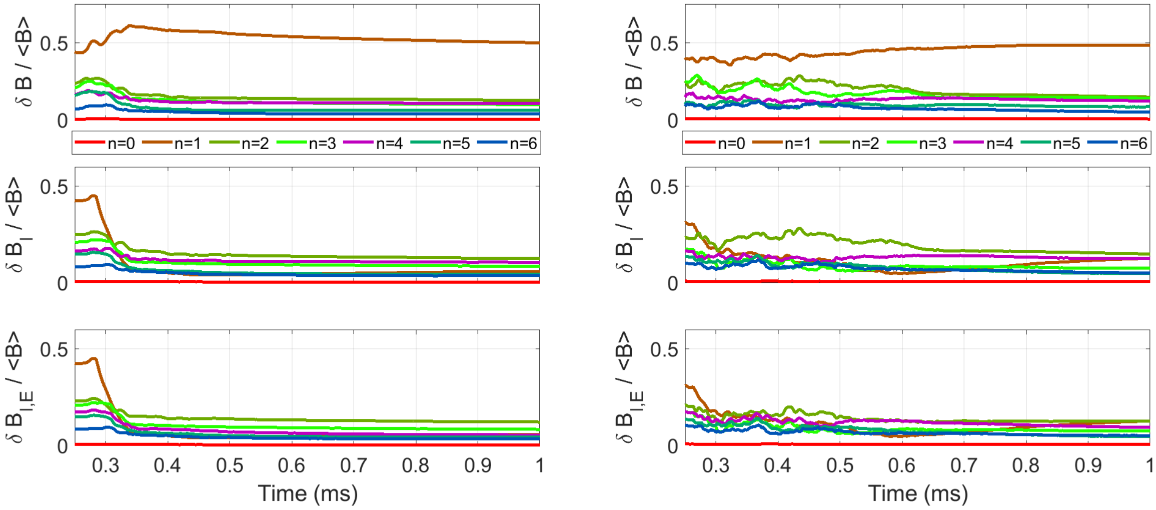

(a) $f_{inj} = 14$ kHz

(b) $f_{inj} = 36$ kHz

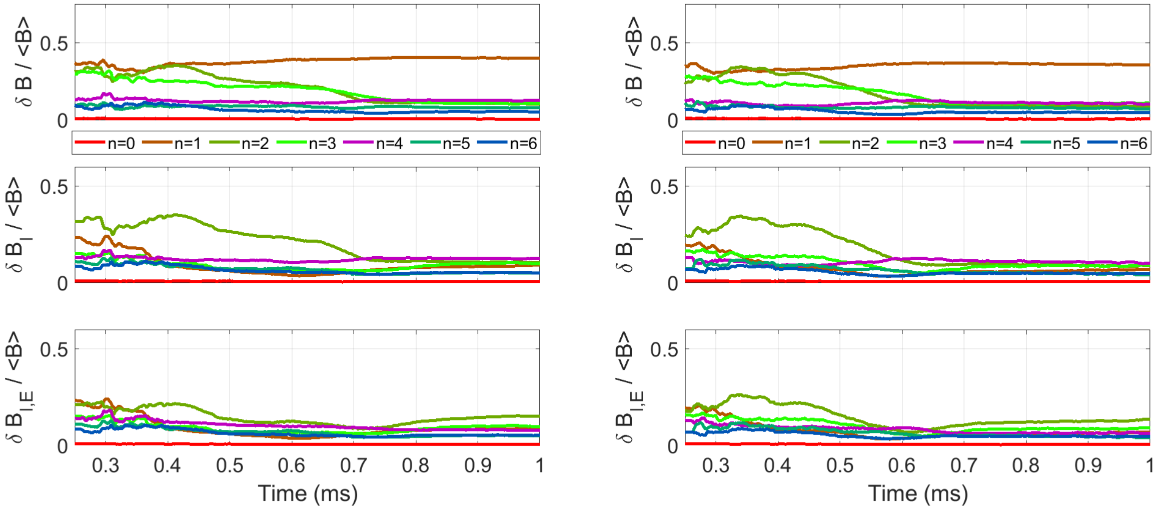

(c) $f_{inj} = 53$ kHz

(d) $f_{inj} = 68$ kHz

Figure 4.11: Fourier spectra of HIT-SI simulations versus injector frequency, showing, top row to bottom, in each subfigure: row 1: perturbation Fourier spectrum normalized to the mean magnetic field (with toroidal mode numbers given in the legend located between the first and second rows); row 2: normalized perturbation spectrum of modes obtained from Fourier decomposition of the dataset with injector-correlated BD modes subtracted (see Eq. 3.11); row 3: As row 2, with equilibrium-correlated BD modes also subtracted (see Eq. 3.12).

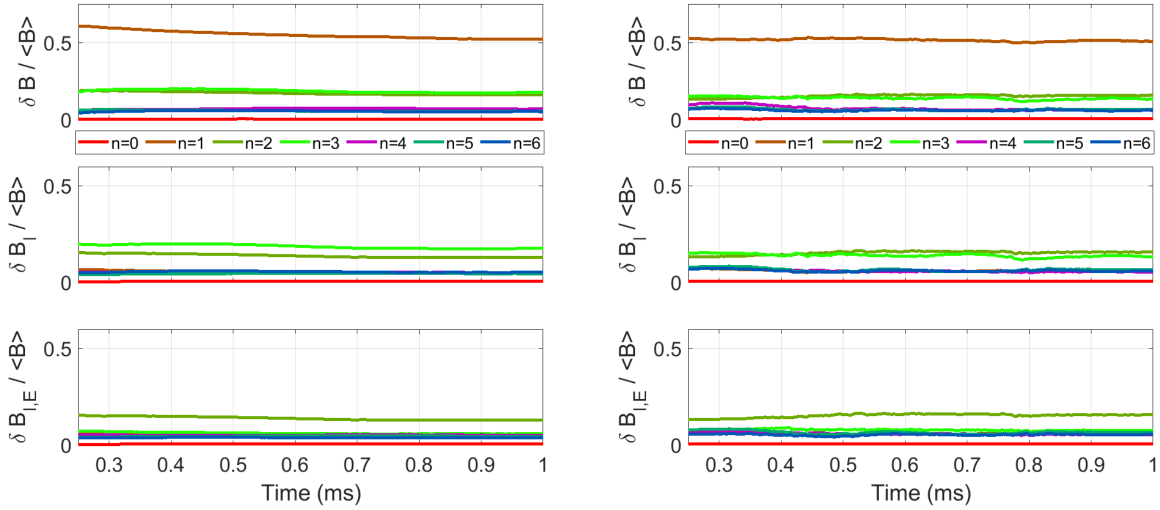

(a) $f_{inj} = 14$ kHz (b) $f_{inj} = 36$ kHz

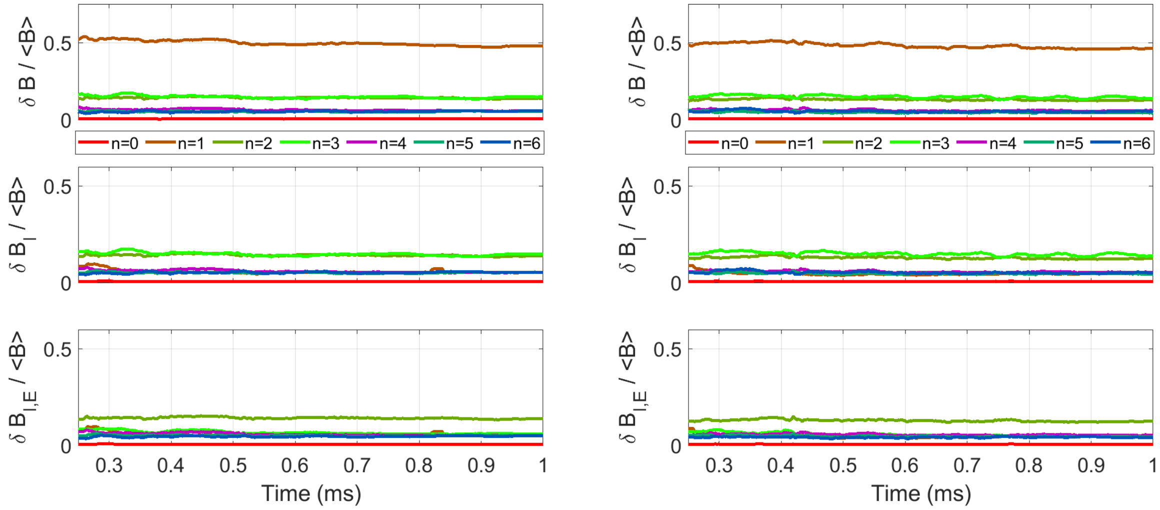

(c) $f_{inj} = 53$ kHz (d) $f_{inj} = 68$ kHz

Figure 4.12: Fourier spectra of HIT-SI3 simulations versus injector frequency, showing, top row to bottom, in each subfigure: row 1: perturbation Fourier spectrum normalized to the mean magnetic field (with toroidal mode numbers given in the legend located between the first and second rows); row 2: normalized perturbation spectrum of modes obtained from Fourier decomposition of the dataset with injector-correlated BD modes subtracted (see Eq. 3.11); row 3: As row 2, with equilibrium-correlated BD modes also subtracted (see Eq. 3.12).

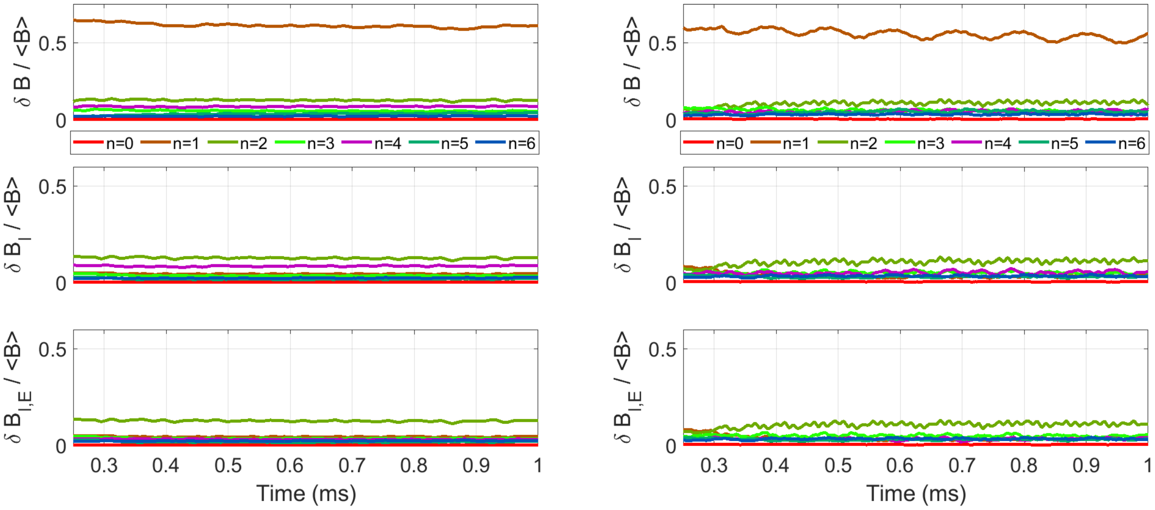

(a) $f_{inj} = 14$ kHz

(b) $f_{inj} = 36$ kHz

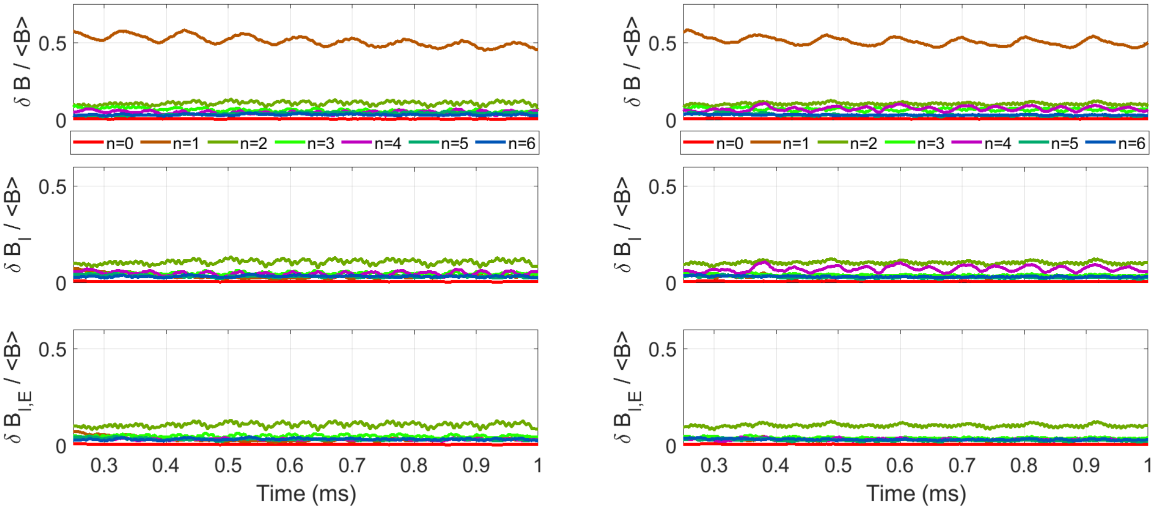

(c) $f_{inj} = 53$ kHz

(d) $f_{inj} = 68$ kHz

Figure 4.13: Fourier spectra of HIT-SIU simulations versus injector frequency, showing, top row to bottom, in each subfigure: row 1: perturbation Fourier spectrum normalized to the mean magnetic field (with toroidal mode numbers given in the legend located between the first and second rows); row 2: normalized perturbation spectrum of modes obtained from Fourier decomposition of the dataset with injector-correlated BD modes subtracted (see Eq. 3.11); row 3: As row 2, with equilibrium-correlated BD modes also subtracted (see Eq. 3.12).

volume.

However, at present, the analysis that has been performed still illuminates the behavior of the different devices at different frequencies: again notice, in the top rows of the subfigures of Fig. 4.13, that there is once again a pronounced oscillation at the same low frequencies as observed in current centroid and density behavior; here it is present in the (brown) $n = 1$ amplitude curves in the decompositions of unsubtracted fields. Also, despite being subjected to the same processing as the HIT-SI and HIT-SI3 data, the HIT-SIU curves all display oscillations in amplitude that the smoother curves of HIT-SI and HIT-SI3 generally do not.

Also, HIT-SI alone among the devices sees continuing changes in relative mode amplitude long after startup begins; for all but the $f_{inj} = 14$ kHz case, HIT-SI's $n = 2$ and $n = 3$ unsubtracted mode amplitudes do not settle to their final asymptotes until after 0.6 ms into the simulated shot; neither other device sees such long-term, aperiodic behavior after the first quarter-millisecond in which startup occurs.

Altogether, the Fourier decompositions of the magnetic field reveal a plethora of complicated dynamics, from which it is not properly possible to extricate the influence of boundary features on sought equilibria of the sort explored in Chapter 2. Nevertheless, the analysis still illuminates the unique behavior of each device, including showing once again the low-frequency periodic behavior in HIT-SIU, and here demonstrating its correlation to injector activity.

4.3.7 Conclusions and recommended further steps

In this chapter, the results of a multidimensional parameter scan have been explored: a set of finite-pressure single-temperature Hall MHD frequency scans of the full plasma volumes using PSI-Tet, as in Chap. 3, on multiple different SIHI device geometries, as in Chap. 2. As boundary shapes can affect equilibrium behavior, as shown in Chap. 2, and as PSI-Tet can help to explore the full dynamics of a SIHI device with time-dependent MHD simulations, as shown in Chap. 3, so too can PSI-Tet be used to search for the influence of boundary shapes on time-dependent plasma performance.

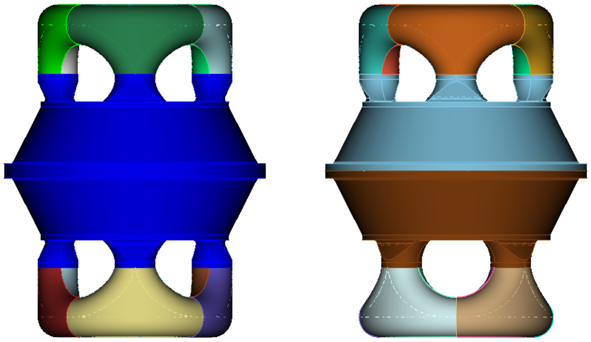

Figure 4.14: Geometries for potential boundary-shape effects evaluation: two HIT-SIU-like geometries with the injector manifold copied and mirrored to the bottom. As-is, that produces the "STACK" device, shown on the left, and with the bottom manifold twisted 45° about the z-axis, that produces the "TWIST" device, shown on the right.

The search presented here, however, is only a beginning: three devices, four frequencies, dozens of surface probes and a single internal magnetic probe line are far from the limit of what this sort of geometric and injector-frequency scan could be. Note, however, that the resoruces required for a multidimensional scan scale polynomially with the number of dimensions, and with PSI-Tet being designed for geometric fidelity more than speed or computational lightness, the limit would certainly be set by practical resource constraints; navigating those is a challenge in themselves.

However, one potential study that could be performed in order to help isolate the influence of boundary shapes versus other parameters would be a direct comparison of two geometries that differ in a single well-defined way. An option for such a geometry is shown in Fig. 4.14, as the corresponding Taylor state equilibria differ as shown in Fig. 4.15.

In order to account for differences in injector phasing, as well (because if the two devices were run with their phasing corresponding to a rotating $n = 1$ imposed perturbation, "TWIST" would impose that in eight steps while "STACK" would impose it in only four double-strength steps,) two phasing cases could also be run per device: one with the afore-

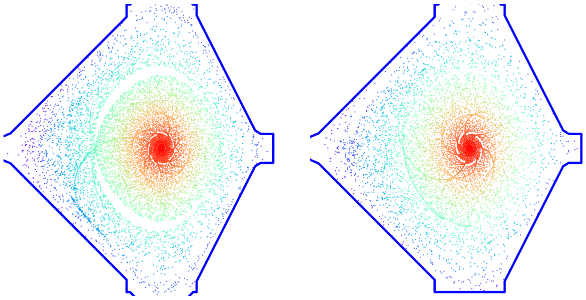

Figure 4.15: Poincaré plots for half of the flux conservers of both of the geometries shown in Fig. 4.14, again with “STACK” at left and “TWIST” on the right. The difference between the two geometries produces a pair of highly pronounced $q = 0.5$ islands in “STACK”, visible as white gaps in its punctures, while “TWIST” sees only very small islands at $q = 0.5$; its boundary perturbation is instead better fit by a single $n = 4$ island that is compressed against the wall but visible as a white gap surrounded by blue at the upper left of “STACK”.

mentioned “rotating $n = 1$” case, and the other with the injector phasings swapped between devices, so that then “STACK” runs with eight injectors at eight phases and “TWIST” with eight injectors at only four phases; this would help to extricate the effects of injector phasing from injector placement.

However, such cases may not be the optimal for testing high-gain simulated spheromaks, where the plasmas should be freer from transient injector effects and closer, in broad theory, to the Taylor state equilibria found to be affected by boundary shapes in Chapter. 2; also found in this three-device frequency scan is that the complicated geometry of injector manifolds tends to enable plasma dynamics other than the desired spheromak to be driven, with structures potentially forming in the manifolds themselves.

A similar effect was observed in an ideal MHD equilibrium study of injector λ, where the value of the injector λ was directly set rather than copied from the calculated spheromak equilibrium λ; varying it to about two-and-a-half times the equilibrium λ, or approximately twice the λ that would be imposed in actual device operation, produced field structures re-

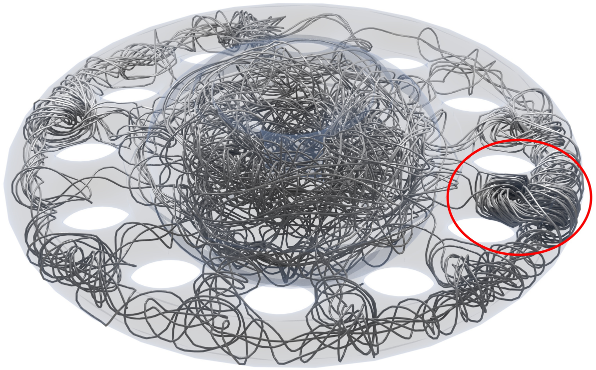

Figure 4.16: Field line traces for a midplane manifold geometry with injector λ artificially set to 20.0m^{-1} compared to the value of approximately 8m^{-1} that was the natural spheromak lambda. This degree of curvature to the injector fields enabled spheromak-like structures to form within the manifold itself, as particularly seen on the right, circled in red.

sembling spheromaks themselves inside the midplane manifold that was under investigation, as seen in Fig. 4.16.

While it is unlikely that such pronounced structures were forming during the simulated shot of HIT-SIU, the extra space within the manifolds affords room for the plasma to self-organize into structures that are not of use to the main spheromak, and that behavior is worth noting for future device designs.

Chapter 5

SUMMARY AND CONCLUSIONS

5.1 The overall value of geometric effects on plasma behavior

As plasmas are a high-energy-density state of matter that can be manipulated remotely, they are potentially of great utility for applications that have need of energy densities too high for ordinary solid containers to endure. Nuclear fusion is the clearest such application: the ability to confine plasmas in magnetic field structures suspended away from any solid walls is the key to steady-state fusion power generation, for unlike nuclear fission, the energies the nuclei must reach in order to react to release their stored energy is far too great for the reacting fuel to be held in solid containers directly.

The influence of boundary conditions on plasma equilibria and time-dependent behavior is therefore of significant interest to the push for magnetic confinement fusion, or at least to the parts of that push that have potential openings for their plasmas to seek minimum-energy equilibria that could potentially deviate from the desired field structure or topology, such as with spheromaks. Spheromaks depend on the Taylor minimum energy principle that says that the plasma will, short of the decay of the entire magnetic structure on the resistive diffusion timescale, seek the state of minimum energy that conserves magnetic helicity. A spheromak is such a minimum-energy-with-conserved-helicity case that has magnetic topology well-suited for fusion in the ideal case, but the ideal case accounts only for axisymmetric boundary conditions and does not account for pressure.

However, features that differ from the ideal case are potentially of use in practical spheromak development, particularly for plasma current drive, of which spheromak-based devices are in need of a great deal, owing to the tradeoff for greater design simplicity being a need for greater plasma current to be driven. The simply-connected spheromak's lack of a central solenoid or toroidal field coil, which are among the components that are the most expensive and sensitive to neutron radiation in conventional tokamak reactor designs. As plasma current is, by conventional methods such as neutral beam injection and radio-frequency drive, power-expensive to drive, a more efficient method of plasma current drive is necessary to produce a functional and economic steady-state spheromak fusion power plant.

A proposed method for such current drive is Steady Inductive Helicity Injection, which satisfies Cowling's anti-dynamo theorem[23] that states that a steady-state axisymmetric dynamo is impossible by sacrificing axisymmetry. But as sacrificing axisymmetry would ordinarily mean sacrificing energy confinement, the goal is to strike a balance between the need for *some* nonaxisymmetry for current drive purposes and the need for *major* axisymmetry for energy confinement purposes.

To that end, Steady Inductive Helicity Injection operates by injecting magnetic fields with net helicity content into the plasma via the use of nonaxisymmetric helicity injectors at a rate sufficient to sustain the spheromak against resistive decay. The parametric refueling is meant to occur via cross-field current drive[22] at the points where, due to the imposed non-axisymmetric perturbation stirring the plasma, the current paths deviate from the magnetic field lines.

Managing the strength and targeting of this perturbation, such that its effects are targeted to current drive maximally and to confinement degradation minimally is therefore of significant importance in ensuring the viability of spheromak-based fusion power generation. Identifying the sources and influences of various boundary-condition features, of both geometric and magnetic types, are therefore of importance to the search for practical fusion power.

And as magnetic-confinement fusion is a plasma-based power source with high energy-per-mass density, it could therefore be of use for (relatively) high-thrust, high-I_{sp} space propulsion, as well, of the sort that could render interplanetary travel more practical.

5.2 Nonaxisymmetric boundary conditions affect Taylor state equilibrium magnetic topology

A place to begin the search for the effects of boundary conditions on spheromak plasma behavior is at the ideal equilibria from which spheromaks are defined, and to which helicity-conserving plasmas are, in the ideal case and under the right timescales, constantly seeking. If there exist strong boundary-shape or boundary magnetic effects on these equilibria, then the nature of those effects could provide guidance for seeking whether such effects persist in more-full simulated plasmas, and ultimately in reality.

In Sec. 2.2 it was shown that nonaxisymmetric boundary shapes often result in the appearance of magnetic islands in the resulting spheromak, at locations defined by the overall q-profile (itself set largely by the overall proportions of the geometry, with peak q being roughly proportional to vertical elongation,) such that, from within the range of available values of q, a Fourier-like decomposition of the boundary shape is constructed.

The effect of this is that boundary features that correspond to an $m/n = q$ mode number that is available in the q-profile can excite islands whose amplitude varies in proportion to the magnitude of the boundary feature. HIT-SI's Taylor state equilibrium, for example, sees a major $q = 1/2$ island corresponding to the placement of the four mouths of its helicity injectors. Islands can also vary in number within a flux surface and also in shape: HIT-SI3 sees three islands on the $q = 1/2$ surface that are themselves not completely symmetric, but slightly distorted so as to accommodate the uneven spacing of the injector mouths.

Nonaxisymmetric features do not need to excite major islands within the boundary, however, if they are small relative to the overall volume, or are shielded from the main spheromak by a region that is narrow compared to the characteristic $1/\lambda$ distance for magnetic field rotation of the Taylor state equilibria.

In Sec. 2.3 it was shown that magnetic boundary conditions independent of geometry, such as injector action, are capable of exciting islands in a geometry that would, based on boundary-shape effects alone, not have them, and that magnetic boundary conditions were also capable of suppressing, or at least transforming, islands that would innately be present due to boundary shape effects.

Overall, if either the presence or absence of equilibrium islands is desired, this analysis suggests that it is possible to sculpt the boundary shape and the applied magnetic boundary conditions to achieve the desired outcome. However, this remains an exploration of ideal equilibria only; the PSI-Tet code can also be used for time-dependent simulations, and the utility of that feature was also explored.

5.3 Increasing injector frequency under constant injector current and voltage increases simulated HIT-SI current gain

Using PSI-Tet's 3D Hall MHD features, a set of simulations (a scan of injector frequency) of the full plasma volume of HIT-SI were performed using finite-pressure, single-temperature Hall MHD, and the results of these simulations were compared to equivalent frequency scans using a zero-beta Hall MHD model in PSI-Tet, the axisymmetric-yet-mature MHD code NIMROD, and experimental HIT-SI data, as shown in Chap. 3.

The PSI-Tet finite-beta frequency scan was found to agree with experimental observations and NIMROD on most parameters, with the most major exception being the outward shift and symmetrization of the radial position of the current centroid, as discussed in Sec. 3.3.3; this is a behavior that single-temperature MHD simulations have yet to capture.

An increase in temperature and current gain was observed for PSI-Tet single-temperature simulated HIT-SI with increasing injector frequency. While this matches the experimental observations of HIT-SI's current gain records being reached at high injector frequency, it must be noted that the constant injector flux and voltage applied as boundary conditions results in an increase in power injection directly proportional to injector frequency; a scan matching injector power to the observed experimental trends may see different results. Also, a low-frequency oscillation, particularly in density, was observed to emerge at high injector frequencies.

However, the application of single-temperature PSI-Tet to simulations of full HIT-SI shots from startup to the end of a simulated millisecond, while clearly lacking total fidelity to reality, nevertheless offers sufficient insight into the dynamics within helicity injectors to be of use in exploring the dynamics within differently-configured helicity injectors, and so the behavior of plasmas under equivalent initial and boundary conditions but within different geometries may be explored.

5.4 Three simulated frequency scans show different dynamics most likely due to different injector behavior

In Chapter 4, two other SIHI device geometries were simulated using PSI-Tet under the same conditions as HIT-SI: HIT-SI3 with three helicity injectors, and HIT-SIU, with a manifold of four. Although these do not correspond to a direct scan of any particular boundary feature, as the injector geometries vary in multiple parameters between all devices, they do correspond to real experiments that either have been operated or are under construction. The injector flux and voltages were scaled between these simulated devices in an attempt to keep the power injection constant across devices at the same frequencies; as such, with the same helicity and power generation at each injector frequency, the effects of the injector count and configuration can be recognized.

That the scan was not sufficiently resolved in terms of isolating the influence of boundary geometries only on the resulting targeted equilibrium, versus different methods of applying injector action, meant that even in the modal analysis of Sec. 4.3.6 there was not sufficient evidence to declare that features corresponding to the equilibrium islands found in Chap. 2 had been observed in the full time-dependent simulations of every one of the different geometries. However, two of the three simulated devices did see correlations between their time-dependent performance and their ideal equilibria, suggesting grounds for further study.

Nevertheless, significant differences were observed in the devices' simulated performance, most notably with HIT-SIU, with its injector manifold, seeing lower current gains and temperatures compared to the other two devices at the equivalent conditions. Although, further investigation is needed to ensure that this difference is not due to lower power injection.

The presence of more complicated behavior in the injector manifolds hints that there could be a different relationship between power and flux/current waveforms than in the other injector configurations. While one reason for the use of injector manifolds is to be able to avoid unwanted coupling between injector action and the spheromak, and instead enable the application of a purer perturbation with less energy in Fourier components other than the desired perturbation mode than discrete injectors could create, there exists the possibility that manifold injectors are less efficient than discrete injectors at producing the desired coupling.

If such a dependence can be confirmed and characterized, then depending on whether imposed-perturbation mode purity or current-drive efficiency is desired in the target operating regime, that could itself determine whether an injector manifold or discrete helicity injectors are preferable for a given design.

5.5 Recommended future steps

The matter of geometric influences on SIHI device performance remains an important one so long as their geometries remain nontrivial; as such, further exploration of the matters discussed in each of the three preceding chapters could be useful to the effort to produce economic spheromak-based fusion power.

To begin with, the matter of boundary shapes on device performance could be further clarified by running studies of the type discussed in Sec. 4.3.7; direct isolation of boundary geometric differences versus injector behavior would be of significant use in disentangling the two effects.

Additionally, clarifying the behavior of injector manifolds versus discrete injectors could also be further explored, perhaps by simulating devices such as those pictured in Fig. 4.1a and Fig. 4.1c. With injector manifolds being targeted for future SIHI devices, as in the under-construction HIT-SIU, characterizing and controlling their performance is a matter of import for controlling the spheromaks they are to create.

Further refinement of PSI-Tet's physics model would be of use in allowing simulations with greater physical fidelity to be performed in these searches; the work of Alan Kaptanoglu[31] in adding a two-temperature model to PSI-Tet is of interest there.

Further exploration of equilibria is also of interest; it would be useful for device design to have a method of predicting in what geometries, and at what size, islands would appear in advance, outside of obvious cases such as flux conservers stretched away from axisymmetry clearly having major $n = 2$ components in their resulting island structure. However, the PSI-Tet Taylor state solver is rapid enough that a quick analytical tool, rather than an applied numerical method, is probably not a major advance.

But above all, continuing to take steps pursuit of plasma control for the purposes of fusion power and space propulsion itself is the most important recommendation; these are big challenges in need of big solutions with many steps; may this one be of use in guiding a few more.

Bibliography

[1] Freidberg, Jeffrey P. *Plasma Physics and Fusion Energy.* Cambridge University Press, 2008.

[2] Pettit, Don. The Tyranny of the Rocket Equation. *National Aeronautics and Space Administration, Expedition*, 30, 2012.

[3] Sovey, James S and Rawlin, Vincent K and Patterson, Michael J. Ion propulsion development projects in US: Space Electric Rocket Test I to Deep Space 1. *Journal of Propulsion and Power*, 17(3):517–526, 2001.

[4] NASA. J-2 Engine Fact Sheet.

[5] NASA. Ion Propulsion Technology.

[6] Diaz, Franklin R Chang. The VASIMR rocket. *Scientific American*, 283(5):90–97, 2000.

[7] Cassibry, Jason and Cortez, Ross and Stanic, Milos and Watts, Andrew and Seidler, William and Adams, Rob and Statham, Geoff and Fabisinski, Leo. Case and development path for fusion propulsion. *Journal of Spacecraft and Rockets*, 52(2):595–612, 2015.

[8] Costley, AE. On the fusion triple product and fusion power gain of tokamak pilot plants and reactors. *Nuclear Fusion*, 56(6):066003, 2016.

[9] Francis F. Chen. *Introduction to Plasma Physics.* Springer.

[10] Aymar, R and Chuyanov, VA and Huguet, M and Shimomura, Y and Teams, ITER Home and others. Overview of ITER-FEAT-the future international burning plasma experiment. *Nuclear Fusion*, 41(10):1301, 2001.

[11] Sutherland, DA and Jarboe, TR and Morgan, KD and Pfaff, M and Lavine, ES and Kamikawa, Y and Hughes, M and Andrist, P and Marklin, G and Nelson, BA. The dynomak: An advanced spheromak reactor concept withimposed-dynamo current drive and next-generation nuclearpower technologies.

[12] Sorbom, BN and Ball, J and Palmer, TR and Mangiarotti, FJ and Sierchio, JM and Bonoli, P and Kasten, C and Sutherland, DA and Barnard, HS and Haakonsen, CB and others. ARC: A compact, high-field, fusion nuclear science facility and demonstration power plant with demountable magnets. *Fusion Engineering and Design*, 100:378–405, 2015.

[13] Wood, RD and Hill, DN and Hooper, EB and Woodruff, S and McLean, HS and Stallard, BW. Improved operation of the SSPX spheromak. *Nuclear Fusion*, 45(12):1582, 2005.

[14] Jarboe, TR and Hamp, WT and Marklin, GJ and Nelson, BA and O'Neill, RG and Redd, AJ and Sieck, PE and Smith, RJ and Wrobel, JS. Spheromak formation by steady inductive helicity injection. *Physical Review Letters*, 97(11):115003, 2006.

[15] Jarboe, Thomas R. Review of spheromak research. *Plasma Physics and Controlled Fusion*, 36(6):945, 1994.

[16] Rosenbluth, MN and Bussac, MN. MHD stability of spheromak. *Nuclear Fusion*, 19(4):489, 1979.

[17] Taylor, J Brian. Relaxation of toroidal plasma and generation of reverse magnetic fields. *Physical Review Letters*, 33(19):1139, 1974.

[18] Taylor, JBj. Relaxation and magnetic reconnection in plasmas. *Reviews of Modern Physics*, 58(3):741, 1986.

[19] Hudson, B and Wood, RD and McLean, HS and Hooper, EB and Hill, DN and Jayakumar, J and Moller, J and Montez, D and Romero-Talamás, CA and Casper, TA and

others. Energy confinement and magnetic field generation in the SSPX spheromak. *Physics of Plasmas*, 15(5):056112, 2008.

[20] Ebrahimi, F and Raman, R. Plasmoids formation during simulations of coaxial helicity injection in the national spherical torus experiment. *Physical Review Letters*, 114(20):205003, 2015.

[21] Jarboe, Thomas R. Steady inductive helicity injection and its application to a high-beta spheromak. *Fusion technology*, 36(1):85–91, 1999.

[22] Jarboe, TR and Victor, BS and Nelson, BA and Hansen, CJ and Akcay, C and Ennis, DA and Hicks, NK and Hossack, AC and Marklin, GJ and Smith, RJ. Imposed-dynamo current drive. *Nuclear Fusion*, 52(8):083017, 2012.

[23] Cowling, Thomas George. The magnetic field of sunspots. *Monthly Notices of the Royal Astronomical Society*, 94:39–48, 1933.

[24] Jarboe, TR and Parker, KM and Mattick, TA and Craw, MM and Gu, P and Hamp, WT and Hwang, AA and Izzo, VA and Jewell, PD and Kim, H and others. Spheromak Fusion Propulsion for Future Solar System Exploration. *Journal of propulsion and power*, 21(2):218–229, 2005.

[25] Victor, BS and Jarboe, TR and Hansen, CJ and Akcay, C and Morgan, KD and Hossack, AC and Nelson, BA. Sustained spheromaks with ideal n= 1 kink stability and pressure confinement. *Physics of Plasmas*, 21(8):082504, 2014.

[26] Glasser, AH and Sovinec, CR and Nebel, RA and Gianakon, TA and Plimpton, SJ and Chu, MS and Schnack, DD and NIMROD team and others. The NIMROD code: a new approach to numerical plasma physics. *Plasma Physics and Controlled Fusion*, 41(3A):A747, 1999.

[27] Lowrie, Weston and Shumlak, Uri and Lukin, Vyacheslav and Glasser, Alan. Multi-Block Development and Applications of HiFi. *APS*, 52:BP9–100, 2010.

[28] Hansen, Christopher. *MHD modeling in complex 3D geometries: towards predictive simulation of SIHI current drive*. PhD thesis, University of Washington, 2014.

[29] Morgan, Kyle. *Finite-beta simulations of the HIT-SI and HIT-SI3 experiments using the NIMROD code*. PhD thesis, University of Washington, 2018.

[30] Sutherland, Derek Aiden. *Measurements of neutral particles and simulations of plasma-neutral dynamics in the HIT-SI3 experiment*. PhD thesis, 2019.

[31] Kaptanoglu, AA and Benedett, TE and Morgan, KD and Hansen, CJ and Jarboe, TR. Two-temperature effects in Hall-MHD simulations of the HIT-SI experiment. *Physics of Plasmas*, 27(7):072505, 2020.

[32] Benedett, TE and Hansen, CJ and Morgan, KD and Jarboe, TR. Effects of temperature and density evolution in MHD simulations of HIT-SI. *Physics of Plasmas*, 27(4):042508, 2020.

[33] Bellan, Paul M. *Fundamentals of Plasma Physics*. Cambridge University Press, 2008.

[34] Rome, James A and Peng, YKM. Topology of tokamak orbits. Technical report, Oak Ridge National Lab., TN (USA), 1978.

[35] La Haye, RJ and Günter, S and Humphreys, DA and Lohr, J and Luce, TC and Maraschek, ME and Petty, CC and Prater, R and Scoville, JT and Strait, EJ. Control of neoclassical tearing modes in DIII–D. *Physics of Plasmas*, 9(5):2051–2060, 2002.

[36] Grad, Harold and Rubin, Hanan. Hydromagnetic equilibria and force-free fields. *Journal of Nuclear Energy (1954)*, 7(3-4):284–285, 1958.

[37] Shafranov, VD. Plasma equilibrium in a magnetic field. *Reviews of plasma physics*, 2:103, 1966.

[38] Waelbroeck, FL. Theory and observations of magnetic islands. *Nuclear Fusion*, 49(10):104025, 2009.

[39] Bauer, Frances and Betancourt, Octavio and Garabedian, Paul. *Magnetohydrodynamic Equilibrium and Stability of Stellarators.* Springer Science & Business Media, 2012.

[40] Reiman, A and Greenside, H. Calculation of three-dimensional MHD equilibria with islands and stochastic regions. Technical report, Princeton Univ., NJ (USA). Plasma Physics Lab., 1986.

[41] Hegna, Chris C and Bhattacharjee, Amitava. Magnetic island formation in three-dimensional plasma equilibria. *Physics of Fluids B: Plasma Physics*, 1(2):392–397, 1989.

[42] Glasser, AH and Greene, JM and Johnson, JL. Resistive instabilities in general toroidal plasma configurations. *The Physics of Fluids*, 18(7):875–888, 1975.

[43] Cary, John R and Kotschenreuther, M. Pressure induced islands in three-dimensional toroidal plasma. *The Physics of fluids*, 28(5):1392–1401, 1985.

[44] Reiman, A and Boozer, Allen H. Island formation and destruction of flux surfaces in three-dimensional MHD equilibria. *The Physics of fluids*, 27(10):2446–2454, 1984.

[45] Shimomura, Y and Aymar, R and Chuyanov, VA and Huguet, M and Matsumoto, H and Mizoguchi, T and Murakami, Y and Polevoi, AR and Shimada, M and Teams, ITER Home and others. ITER-feat operation. *Nuclear Fusion*, 41(3):309, 2001.

[46] Simonen, TC and Matsuoka, M and Bhadra, DK and Burrell, KH and Callis, RW and Chance, MS and Chu, MS and Greene, JM and Groebner, RJ and Harvey, RW and others. Neutral-beam current-driven high-poloidal-beta operation of the DIII-D tokamak. *Physical Review Letters*, 61(15):1720, 1988.

[47] Wallace, GM and Hubbard, AE and Bonoli, PT and Faust, IC and Harvey, RW and Hughes, JW and LaBombard, BL and Meneghini, O and Parker, RR and Schmidt, AE and others. Lower hybrid current drive at high density in Alcator C-Mod. *Nuclear Fusion*, 51(8):083032, 2011.

[48] Raman, R and Mueller, D and Jardin, SC and Jarboe, TR and Nelson, BA and Bell, MG and Gerhardt, SP and Hooper, EB and Kaye, SM and Kessel, CE and others. Non-inductive plasma start-up on NSTX and projections to NSTX-U using transient CHI. *Nuclear Fusion*, 53(7):073017, 2013.

[49] Raman, Roger and Jarboe, TR and Nelson, BA and Izzo, VA and O'Neill, RG and Redd, AJ and Smith, RJ. Demonstration of plasma startup by coaxial helicity injection. *Physical Review Letters*, 90(7):075005, 2003.

[50] Hooper, E Biclcford and Bulmer, RH and Cohen, BI and Hill, DN and Holcomb, CT and Hudson, B and McLean, HS and Pearlstein, LD and Romero-Talamás, CA and Sovinec, CR and others. Sustained spheromak physics experiment (SSPX): design and physics results. *Plasma Physics and Controlled Fusion*, 54(11):113001, 2012.

[51] Wrobel, JS and Hansen, CJ and Jarboe, TR and Smith, RJ and Hossack, AC and Nelson, BA and Marklin, GJ and Ennis, DA and Akcay, C and Victor, BS. Relaxation-time measurement via a time-dependent helicity balance model. *Physics of Plasmas*, 20(1):012503, 2013.

[52] Hossack, Aaron C and Jarboe, TR and Chandra, RN and Morgan, KD and Sutherland, DA and Penna, JM and Everson, CJ and Nelson, BA. Plasma response to sustainment with imposed-dynamo current drive in HIT-SI and HIT-SI3. *Nuclear Fusion*, 57(7):076026, 2017.

[53] Bondeson, A and Marklin, G and An, ZG and Chen, HH and Lee, YC and Liu, CS. Tilting instability of a cylindrical spheromak. *The Physics of Fluids*, 24(9):1682–1688, 1981.

[54] Finn, John M and Manheimer, Wallace M and Ott, Edward. Spheromak tilting instability in cylindrical geometry. *The Physics of Fluids*, 24(7):1336–1341, 1981.

[55] CUBIT Development Team. CUBIT: Geometry and mesh generation toolkit.

[56] Udintsev, VS and Ottaviani, M and Maget, P and Giruzzi, G and Segui, JL and Aniel, T and Artaud, JF and Clairet, F and Goniche, M and Hoang, GT and others. Experimental observation of m/n= 1/1 mode behaviour during sawtooth activity and its manifestations in tokamak plasmas. *Plasma Physics and Controlled Fusion*, 47(8):1111, 2005.

[57] Akcay, Cihan. *Extended magnetohydrodynamic simulations of the helicity injected torus (HIT-SI) spheromak experiment with the NIMROD code*. PhD thesis, 2013.

[58] Jarboe, T and Victor, BS and Nelson, BA and Hansen, CJ and Akcay, C and Ennis, DA and Hicks, NK and Hossack, AC and Marklin, GJ and Smith, RJ. Progress on HIT-SI and Imposed Dynamo Current Drive. Technical report, 2012.

[59] Akcay, Cihan and Kim, Charlson and Jarboe, Tom and Nelson, Brian. Extended MHD NIMROD Simulations of HIT-SI plasmas. *Bulletin of the American Physical Society*, 57, 2012.

[60] Hansen, C and Marklin, G and Victor, B and Akcay, C and Jarboe, T. Simulation of injector dynamics during steady inductive helicity injection current drive in the HIT-SI experiment. *Physics of Plasmas*, 22(4):042505, 2015.

[61] Morgan, KD and Jarboe, TR and Hossack, AC and Chandra, RN and Everson, CJ. Validation of extended magnetohydrodynamic simulations of the HIT-SI3 experiment using the NIMROD code. *Physics of Plasmas*, 24(12):122510, 2017.

[62] C.R. Sovinec and A.H. Glasser and T.A. Gianakon and D.C. Barnes and R.A. Nebel and S.E. Kruger and S.J. Plimpton and A. Tarditi and M.S. Chu and the NIMROD Team. Nonlinear Magnetohydrodynamics with High-order Finite Elements. *J. Comp. Phys.*, 195:355, 2004.

[63] Birn, J and Drake, JF and Shay, MA and Rogers, BN and Denton, RE and Hesse, M and Kuznetsova, M and Ma, ZW and Bhattacharjee, A and Otto, A and others.

Geospace Environmental Modeling (GEM) magnetic reconnection challenge. *Journal of Geophysical Research: Space Physics*, 106(A3):3715–3719, 2001.

[64] Hansen, C and Victor, B and Morgan, K and Jarboe, T and Hossack, A and Marklin, G and Nelson, BA and Sutherland, D. Numerical studies and metric development for validation of magnetohydrodynamic models on the HIT-SI experiment. *Physics of Plasmas*, 22(5):056105, 2015.

[65] Rypl, D. T3d mesh generator. *URL: http://ksm. fsv. cvut. cz/dr/t3d. html*, 2004.

[66] Halpern, Federico D and Lütjens, Hinrich and Luciani, Jean-François. Diamagnetic thresholds for sawtooth cycling in tokamak plasmas. *Physics of Plasmas*, 18(10):102501, 2011.

[67] Zhang, W and Ma, ZW and Wang, S. Hall effect on tearing mode instabilities in tokamak. *Physics of Plasmas*, 24(10):102510, 2017.

[68] S.I. Braginskii. Transport Processes in a Plasma. *Reviews of Plasma Physics*, 1:205, 1965.

[69] O'Bryan, JB and Sovinec, CR and Bird, TM. Simulation of current-filament dynamics and relaxation in the Pegasus Spherical Tokamak. *Physics of Plasmas*, 19(8):080701, 2012.

[70] Spitzer Jr, Lyman. 1962, Physics of Fully Ionized Gases. *Interscience Tracts on Physics and Astronomy*, 3, 1.

[71] A.C. Hossack and T.R. Jarboe and R.N. Chandra and K.D. Morgan and D.A. Sutherland and J.M. Penna and C.J. Everson and B.A. Nelson. Plasma response to sustainment with imposed-dynamo current drive in HIT-SI and HIT-SI3. *Nuclear Fusion*, 57:076026, 2017.

[72] C. Akcay and C.C. Kim and B.S. Victor and T.R. Jarboe. Validation of single-fluid and two-fluid magnetohydrodynamic models of the helicity injected torus spheromak experiment with the NIMROD code. *Phys. Plasmas*, 20:082512, 2013.

[73] Schnack, Dalton D and Barnes, Daniel C and Brennan, Dylan P and Hegna, Chris C and Held, E and Kim, Charlson C and Kruger, Scott E and Pankin, Alexey Y and Sovinec, Carl R. Computational modeling of fully ionized magnetized plasmas using the fluid approximation. *Physics of plasmas*, 13(5):058103, 2006.

[74] Izzo, VA and Jarboe, TR. Three-dimensional magnetohydrodynamic simulations of the Helicity Injected Torus with Steady Inductive drive. *Physics of plasmas*, 12(5):056109, 2005.

[75] Jarboe, TR and Hansen, CJ and Hossack, AC and Marklin, GJ and Morgan, KD and Nelson, BA and Sutherland, DA and Victor, BS. A proof of principle of imposed dynamo current drive: Demonstration of sufficient confinement. *Fusion Science and Technology*, 66(3):369–384, 2014.

[76] Jarboe, T and Victor, B and Nelson, B and Hansen, C and Akcay, C and Ennis, D and Hicks, N and Hossack, A and Marklin, G and Smith, R. Progress on HIT-SI and Imposed Dynamo Current Drive. Technical report, Technical Report No. ICC/P4-31, 2012.

[77] Hooper, E Bickford and Cohen, Bruce I and McLean, HS and Wood, RD and Romero-Talamas, CA and Sovinec, CR. NIMROD resistive magnetohydrodynamic simulations of spheromak physics. *Physics of Plasmas*, 15(3):032502, 2008.

[78] Dudok de Wit, T and Pecquet, A-L and Vallet, J-C and Lima, R. The biorthogonal decomposition as a tool for investigating fluctuations in plasmas. *Physics of plasmas*, 1(10):3288–3300, 1994.

[79] Nardone, C. Multichannel fluctuation data analysis by the singular value decomposition method. Application to MHD modes in JET. *Plasma physics and controlled fusion*, 34(9):1447, 1992.

[80] Levesque, JP and Rath, N and Shiraki, D and Angelini, S and Bialek, J and Byrne, PJ and DeBono, BA and Hughes, PE and Mauel, ME and Navratil, GA and others. Multimode observations and 3D magnetic control of the boundary of a tokamak plasma. *Nuclear Fusion*, 53(7):073037, 2013.

[81] Noack, Bernd R and Afanasiev, Konstantin and Morzyński, Marek and Tadmor, Gilead and Thiele, Frank. A hierarchy of low-dimensional models for the transient and post-transient cylinder wake. *Journal of Fluid Mechanics*, 497:335–363, 2003.

[82] Victor, BS and Akcay, C and Hansen, CJ and Jarboe, TR and Nelson, BA and Morgan, KD. Development of validation metrics using biorthogonal decomposition for the comparison of magnetic field measurements. *Plasma Physics and Controlled Fusion*, 57(4):045010, 2015.

[83] Scime, Earl and Cekic, Miodrag and Den Hartog, DJ and Hokin, Samuel and Holly, DJ and Watts, Christopher. Ion heating and magnetohydrodynamic dynamo fluctuations in the reversed-field pinch. *Physics of Fluids B: Plasma Physics*, 4(12):4062–4071, 1992.

[84] O'Bryan, JB and Romero-Talamás, CA and Woodruff, S. Simulation of multi-pulse coaxial helicity injection in the Sustained Spheromak Physics Experiment. *Physics of Plasmas*, 25(3):032503, 2018.

Appendix A

SCRIPT FOR GEOMETRY PERTURBATION SCAN BOUNDARIES

```
#elongated_jou_maker_all.py
#Script for generating CUBIT scripts for volumes for boundary-perturbation
                                        scan after original by Chris Hansen
marray = ['1','1','2','2']
narray = ['2','3','3','4']
aarray = ['0.01','0.02','0.03','0.04','0.05','0.06','0.07','0.08','0.09','
                                       0.10','0.11','0.12','0.13','0.14','0.
                                       15','0.16','0.17','0.18','0.19','0.20
                                       ']

str1 = '''reset
undo off

# Define the basic geometry
#{nTheta=80}
#{nPhi=80}
#{R0=1.0}
#{a=0.66}

# Define the perturbation
#{amp='''
  str2 = '''}
#{m='''
  str3 = '''}
#{n='''
  str4 = '''}
```

```
# Construct toroidal slices
#{phi_step=0}
#{Loop(nPhi)}
#{theta_step=0}
#{Loop(nTheta)}
#{minor_radius = a*(1 + amp*(cosd(m*theta_step*360/nTheta)*cosd(n*phi_step
                                     *360/nPhi)+sind(m*theta_step*360/
                                     nTheta)*sind(n*phi_step*360/nPhi)))}
#{R = R0 + minor_radius*cosd(theta_step*360/nTheta)}
#{Z = minor_radius*sind(theta_step*360/nTheta)}
create vertex {R*cosd(phi_step*360/nPhi)} {R*sind(phi_step*360/nPhi)} {Z}
#{theta_step++}
#{EndLoop}
create curve spline vertex {phi_step*nTheta+1} to {(phi_step+1)*nTheta} {
                                     phi_step*nTheta+1} delete
#{phi_step++}
#{EndLoop}

# Assemble toroidal slices into volume
#{phi_step=1}
#{nPhi_int = nPhi-1)
  #{Loop(nPhi_int)}
  create surface skin curve {phi_step} {phi_step+1}
  #{phi_step++}
  #{EndLoop}
  create surface skin curve {nPhi} 1
  create volume surface 1 to {nPhi} heal

  # Cleanup
  delete curve 1 to {nPhi}

  # Create central "gap"
```

```
create Cylinder height {a/10} radius 1
unite Volume {nPhi} {nPhi+1}

unite volume all
volume all scale 1.0 1.0 1.2

# Generate mesh
volume all scheme Tetmesh
set tetmesher interior points on
set tetmesher optimize level 3  overconstrained  off sliver  off
set tetmesher boundary recovery  off
volume all tetmesh growth_factor 1.0
volume all size .08
mesh volume all

# Save mesh to file
block 1 volume all
block 1 element type tetra10
export Genesis  "/home/tebkwd/Documents/CAD_files'''
str5 = '''.g" block 1 overwrite


'''

f = open("elongated81.jou","w")

m = 0
n = 0
a = 0.0
strcomposite = str1+a+str2+m+str3+n+str4+m+'n'+n+'a'+a+str5
f.write(strcomposite)
for i in range(2):
m = marray[i]
```

```
n = narray[i]
for a in aarray:
strcomposite = str1+a+str2+m+str3+n+str4+m+’n’+n+’a’+a+str5
f.write(strcomposite)
f.close()
```

Appendix B

SCRIPT FOR WALL-PERTURBED ZERO-INJECTOR HIT-SI BOUNDARY

Presented here is the CUBIT script by Chris Hansen for the volume shown in Fig. 2.27. Python-style line breaks for presentation are indicated with lines ending with “\”.

```
##########################
## Create "Injectorless" HIT-SI Geometry with wall perturbation
###########################


reset
undo off
Set Maximum Arc_Span 90

# Define the basic geometry
#{nR=10}
#{nPhi=60}
#{R0=25.84}
#{R1=40.34294648}
#{Z0=29.6731}

# Define the perturbation
#{amp=0.05}
#{n=2}
#{amp_max=amp*(R1-R0)*(R1-R0)}
```

```
###########################
## Create confinement volume
###########################

# Vertices
create vertex 0 0 0
create vertex 0 4.03430245 0
create vertex 1.79605122 4.77825122 0
create vertex 25.46802561 28.45022561 0
create vertex 25.84 29.34825122 0
create vertex 25.84 {amp_max+Z0} 0
create vertex 40.34294648 {amp_max+Z0} 0
create vertex 40.34294648 27.75568243 0
create vertex 40.48152483 27.17880719 0
create vertex 52.45754091 3.69032476 0
create vertex 53.58896256 2.9972 0
create vertex 55.60218540 2.9972 0
create vertex 55.60218540 0 0

# Arc centers
create vertex 0 6.574302 0
create vertex 24.57 29.348251 0
create vertex 41.612946 27.755682 0
create vertex 53.588963 4.2672 0

# Curves
create curve vertex 1 vertex 2
```

```
create curve arc center vertex 14  2  3  radius 2.54
create curve vertex 3 vertex 4
create curve arc center vertex 15 4 5 radius 1.27
create curve vertex 5 vertex 6
create curve vertex 6 vertex 7
create curve vertex 7 vertex 8
create curve arc center vertex 16 8 9 radius 1.27
create curve vertex 9 vertex 10
create curve arc center vertex 17 10 11 radius 1.27
create curve vertex 11 vertex 12
create curve vertex 12 vertex 13
create curve vertex 13 vertex 1

# Delete arc centers
delete vertex 14 15 16 17

#
create surface curve all
sweep surface 1  yaxis angle 360
Volume 1  copy reflect y nomesh
unite volume 1 2

# Construct toroidal slices
#{phi_step=0}
#{Loop(nPhi)}
create vertex {R0*.9*cosd((nPhi-phi_step)*360/nPhi)} {Z0+1.1*amp_max} \
{R0*.9*sind((nPhi-phi_step)*360/nPhi)}
create vertex {R0*.9*cosd((nPhi-phi_step)*360/nPhi)} {Z0}  \
```

```
{R0*.9*sind((nPhi-phi_step)*360/nPhi)}
#{R_step=0}
#{Loop(nR)}
#{R = (R1-R0)*R_step/(nR-1) + R0}
#{Z = Z0 + amp*(R-R0)*(R1-R)*cosd(n*(nPhi-phi_step)*360/nPhi)}
create vertex {R*cosd((nPhi-phi_step)*360/nPhi)} {Z} \
{R*sind((nPhi-phi_step)*360/nPhi)}
#{R_step++}
#{EndLoop}
create vertex {R1*1.1*cosd((nPhi-phi_step)*360/nPhi)} {Z0} \
{R1*1.1*sind((nPhi-phi_step)*360/nPhi)}
create vertex {R1*1.1*cosd((nPhi-phi_step)*360/nPhi)} {Z0+1.1*amp_max} \
{R1*1.1*sind((nPhi-phi_step)*360/nPhi)}


create curve vertex {(nR+10)*phi_step+44} {(nR+10)*phi_step+45}
create curve vertex {(nR+10)*phi_step+45} {(nR+10)*phi_step+46}
create curve spline vertex {(nR+10)*phi_step+46} to \
{nR-1+(nR+10)*phi_step+46} delete
create curve vertex {nR-1+(nR+10)*phi_step+46} {nR+(nR+10)*phi_step+46}
create curve vertex {nR-1+(nR+10)*phi_step+47} {nR+(nR+10)*phi_step+47}
create curve vertex {nR+(nR+10)*phi_step+47} {(nR+10)*phi_step+44}
create surface curve {6*phi_step+60} to {6*(phi_step+1)+59}
#{phi_step++}
#{EndLoop}

# Loft tool volume
#{phi_step=0}
```

```
#{nPhi_1=nPhi-1}
#{Loop(nPhi_1)}
#create volume loft surface {phi_step+2+24*nPhi} {phi_step+3+24*nPhi}
create volume loft surface {phi_step+26} {phi_step+27}
#{phi_step++}
#{EndLoop}
create volume loft surface {nPhi+25} {26}
unite volume {nPhi+3} to {2*nPhi+2}
delete body 3 to {2+nPhi}

# Perform subtractions
subtract volume {nPhi+3}  from volume 1
webcut volume 1  with plane yplane offset {-Z0}
delete volume 1

# Align and scale volume
rotate Volume all  angle 90 about X include_merged
Volume all scale .01

# Generate mesh
volume all scheme Tetmesh
set tetmesher interior points on
set tetmesher optimize level 3  overconstrained  off sliver  off
set tetmesher boundary recovery  off
Trimesher geometry sizing off
volume all tetmesh growth_factor 1.0
volume all size .035
mesh volume all
```

```
# Save mesh to file
block 1 volume all
block 1 element type tetra10
export Genesis  "HIT_wall_pert.g" block 1 overwrite
```

Appendix C

GEM RECONNECTION CHALLENGE BENCHMARK USING PSI-TET

C.1 Recap of the GEM Reconnection Challenge

The Geospace Environmental Modeling Magnetic Reconnection Challenge (Birn et al.[63]) is a standard test case for plasma modeling codes, serving to test whether their simulations of a particular magnetic reconnection case are accurate.

Specifically, reconnection in two dimensions is studied through the simulation of a Harris sheet equilibrium with a seed magnetic island. As the test case is meant to be used for a variety of codes, the details of the challenge are defined in terms of and normalized to just a few key parameters, so the implementation can be fit to particular codes as necessary. With those units taken into account, it is expected that the behavior of PSI-TET will match the behavior of other codes, and so a successful completion of the challenge should serve to help verify the PSI-TET code.

C.2 Units, Relations, Initial Conditions, and Expected Results

C.2.1 Units

In Birn et al., quantities are given in unitless multiples of important properties of the problem. These are:

Length: lengths are given in multiples of the ion inertial length c/ω_{pi}, where $\omega_{pi} = \sqrt{n_0(Z_i e)^2/m_i \epsilon_0}$. Ions are also assumed to be singly-charged ($Z_i = 1$).

Time: timescales are given in multiples of the inverse of the ion cyclotron frequency: $\Omega_i^{-1} = m_i/Z_i e B_0$.

Speed: multiples of the Alfvén speed: $v_A = B/\sqrt{\mu_0 \rho}$, where $\rho = \Sigma n_j m_j = m_i n_i + m_e n_e$.

$B = B_0$ in the definition of the reference speed.

C.2.2 Relations

To determine what the controlling settings that must be selected are, a few relations are provided:

$\lambda = 0.5(c/\omega_{pi})$

$n_\infty/n_0 = 0.2$

$T_e/T_i = 1.0$

$B_0^2 = 2\mu_0(T_i)n_0 \Rightarrow B_0 = \sqrt{2\mu_0 T_{i_{eV}} n_0 e}$ (factor of e to convert eV to J)

$m_i/m_e = 25$. This ratio is specified in the original paper; it is a good deal smaller than any real ion-to-electron mass ratio, and was presumably selected for ease of numerical calculation.

Initially, $n_i = n_e = n_0$, so $v_A = B_0/\sqrt{1.04\mu_0 n_0 m_i}$

This indicates that the independent variables whose quantities must be defined in the appropriate unit set (SI) for PSI-TET are T_i, n_0, m_i.

Initial Conditions

$L_x = 12.8(c/\omega_{pi}), L_z = 25.6(c/\omega_{pi}), -L_x/2 \leq x \leq L_x/2, -L_z/2 \leq z \leq L_z/2.$

$B_z(z) = B_0 \tanh(z/\lambda)$

$n(z) = n_0 \text{sech}^2(z/\lambda) + n_\infty$

At the z-boundaries, $B_z = \partial B_x/\partial z = \partial B_y/\partial z = 0$. That is, there are no Z-magnetic fields and no change in the perpendicular magnetic fields at the boundary.

There is also a magnetic perturbation, defined in terms of flux: $\psi(x,z) = \psi_0 \cos(2\pi x/L_x)\cos(\pi z/L_z)$, where, in normalized units, $\psi_0 = 0.1$.

That is interpreted as $\hat{y} \times \nabla\psi = \delta\vec{B}$, so the amplitude of $\delta\vec{B}/B_0 = 0.1$. The amplitude of the gradient is $\psi_0 \pi \sqrt{L_x^{-2} + L_z^{-2}} = 0.1 B_0$.

BIRN ET AL.: GEM RECONNECTION CHALLENGE

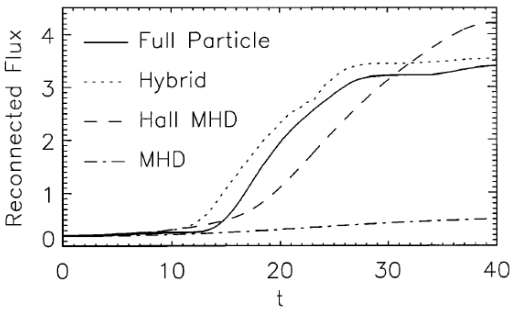

Figure 1. The reconnected magnetic flux versus time from a variety of simulation models: full particle, hybrid, Hall MHD, and MHD (for resistivity $\eta = 0.005$).

Figure C.1: Expected results for the GEM reconnection challenge

Expected Results

The expected results are mainly expressed in Ref. 63 as an expected reconnected-flux-vs.-time profile given in its Figure 1, reproduced in Fig. C.1.

The Approach

The problem requires a grid, 25.6 in the z-direction and 12.8 in the x-direction. As PSI-TET is a 3-D code dependent on tetrahedral meshing, it must be converted into a 3-D problem. Let the domain be as small (yet finite) as possible in the y-direction, and use periodic boundary conditions in the y-direction. As this problem is designed as a 2-D case, there should be no activity in the y-direction, but the boundary conditions are chosen to avoid damping any that may appear.

Let

$T_i = 100$ eV, $n_0 = 5.196374002851238 \times 10^{16}$ m^{-3}, $m_i = m_{H^1}$.

The slab-mesh is generated in T3D, with $dx = 0.1$, making $L_y = 2dx = 0.2$ m.

Requisite values based on those initial values include

Resistivity $= m\nu_{ei}/ne^2 = \mu_0 l_0 v_A \hat{\eta}$. Because $l_0 = 1$ and μ_0 is factored in later, $\eta = 0.005 v_A$ $\approx 742.5892101919615$ m/s.

Table C.1: Parameters for PSI-Tet GEM benchmark

Parameter	Value [Units]
B_0	0.001584586464007 [T]
ω_{pi}	299792458 $[\frac{\text{rad}}{\text{s}}]$
Ion inertial length	1.0 [m]
Ω_i^{-1}	$6.602443600492060 \times 10^{-6}$ [s]
v_A	148517.8420383923 [m/s]
L_x	12.8 [m]
L_z	25.6 [m]
ψ_0	$5.774588374456838 \times 10^4$ [Wb]

Similarly, viscosity $= l_0 n_0 M_i v_A \hat{\nu}$, where $\nu = 0.05$ and everything but v_A is one or factored in later. Thus $\nu \approx 7425.892101919615$ m/s.

Hall MHD is compared to resistive MHD to confirm difference in behavior as seen in Ref. 63. The flux through the plane $x = 0, z \geq 0$ is measured with normal $+\hat{x}$ and the initial flux is subtracted to obtain the reconnected flux as plotted in Fig. 1 of Ref. 63. Qualitatively, plots of the shapes of the evolved distributions are compared to other codes' results for the same regimes.

C.3 The Implementation

A program to implement the simulation described above has been written, based mainly off the "test_xmhd" example program, which tested the extended MHD capabilities of PSI-TET through evaluating the propagation of a sound wave. As in that file, an interpolation class was written to initialize the distributions described above.

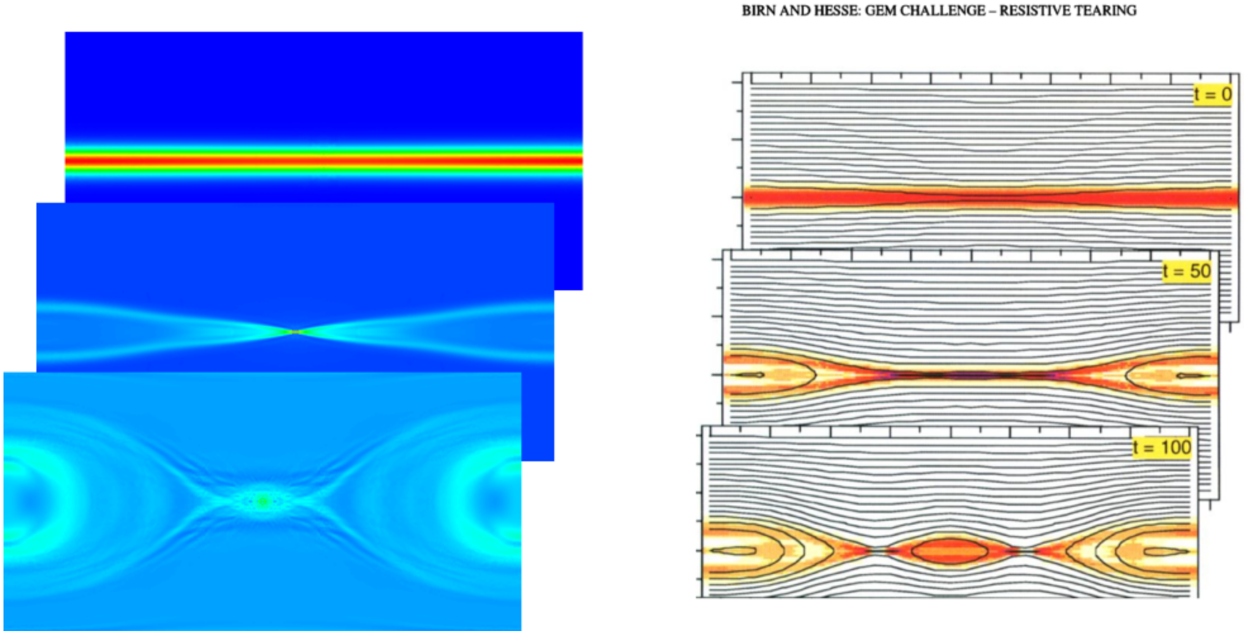

Figure C.2: Comparison of PSI-TET's current density results with other code's at (near)-equivalent timesteps, showing similarity in evolution

C.3.1 Initial Results

Though the reconnected flux has not been normalized, qualitatively the results seem to be appropriate for Hall and resistive MHD.

Also, the results for the resistive MHD run appear qualitatively similar, as seen in Figure C.2, with plots of current density from the PSI-TET run on the left and from Ref. 63 on the right:

A grid convergence study found that the trends in dynamics were as expected, as shown in Fig. C.3. A study of increasing polynomial degree also found results as expected, as shown in Fig. C.4.

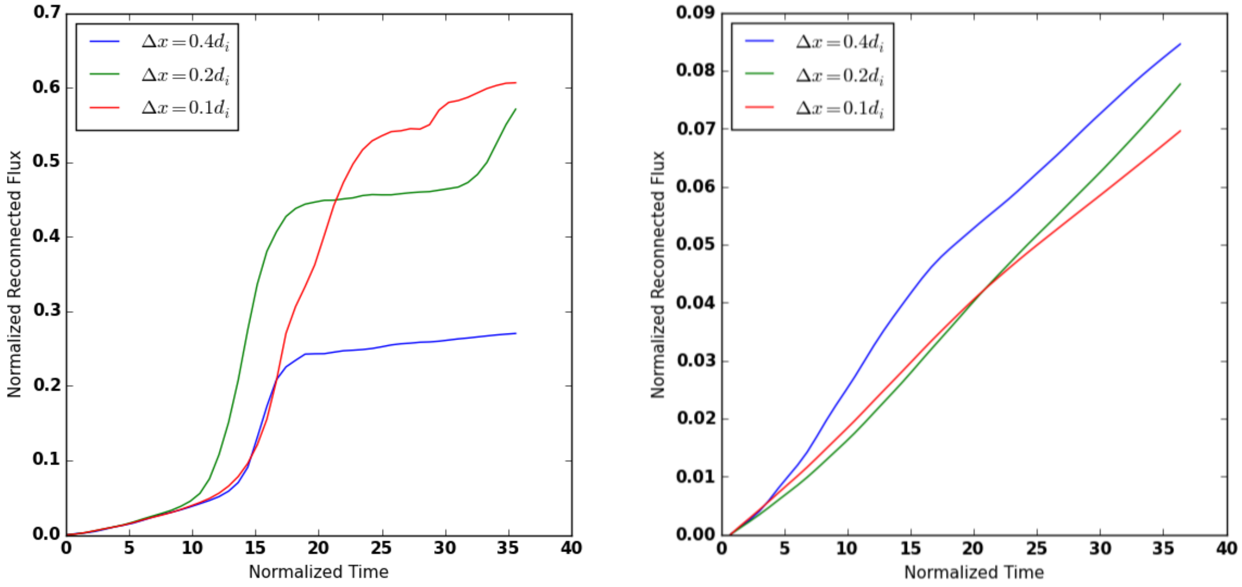

Figure C.3: Effect of increasing grid resolution on amount of reconnected flux at polynomial degree of 1. As grid resolution increases, the rate of reconnection increases in the Hall case (left), while the non-Hall case (right) is largely unaffected.

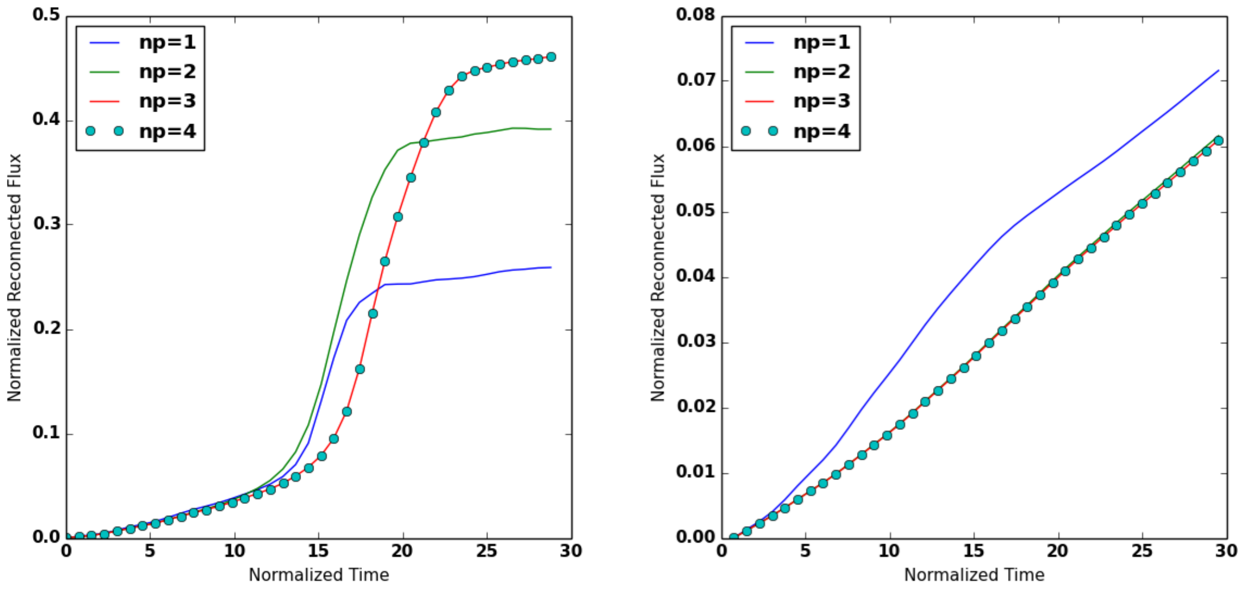

Figure C.4: Effect of increasing polynomial degree on reconnected flux with the lowest-resolution grid. In the Hall case (left) convergence was sharp, with the results for *np*=3 and *np*=4 overlapping almost perfectly, while with the non-Hall case (right,) convergence happened even more rapidly.

VITA

Thomas Edwin Benedett
Bachelor of Science in Aerospace Engineering
Missouri University of Science and Technology
May 2014

Doctor of Philosophy
University of Washington
August 2020